Graphene-based devices for biological sensing

Master's thesis
University of Jyväskylä
Department of Chemistry
18.06.2020
Henri Kaaripuro

Abstract

The aim of this Master's thesis was to study the application of graphene in biological sensing. The theoretical section is set up with a short overview of the basic physical properties of graphene. Two different measurement configurations, field effect transistor and multielectrode array, are discussed briefly. The remaining section covers the detection of different biological molecules and electrogenic cells using the transistor setup, and application of these devices in neurobiology.

In the experimental section, fluorescence quenching properties of graphene were studied by coating the material with biotinylated bovine serum albumin, which had a dye molecule (fluorescein isothiocyanate) bound to it *via* avidin. Avidin is a protein which binds strongly to biotin. The studied areas of graphene contained two grids of two-photon oxidized graphene squares: different squares having different irradiation parameters, and different grids having squares of differing width. The section begins with a theoretical review of the measurement techniques, surface adsorption of bovine serum albumin, and fluorescence quenching in general as well as in the case of graphene. The sample was studied before and after protein functionalization by optical microscopy, atomic force microscopy and Raman spectroscopy, and by fluorescence lifetime imaging microscopy after protein functionalization.

The ratio of graphene's integrated D and G bands ($I(\mathrm{D})I(\mathrm{G})^{-1}$) is used as a measure of disorder in the material. $I(\mathrm{D})I(\mathrm{G})^{-1}$ was found to depend somewhat linearly on irradiation parameters, laser pulse energy and irradiation time. The height of the oxidized squares was found to increase nonlinearly as $I(\mathrm{D})I(\mathrm{G})^{-1}$ did, as expected, but it was also noted to be affected by the size of the irradiated area. The average fluorescence lifetime was found to be linearly dependent on the square height, and Pearsons R value 0.95 for measurements on both grids were achieved. The interception and slope values of the fits were largely different, implying that the square area has an effect on the behavior. The situation at hand is most likely a distribution of lifetimes, brought up by the dye molecules residing at many varying distances from the graphene. Two linearly behaving lifetimes could also be extracted, but a third one is filling the fit with barely a sign of determinism, indicating overfitting.

Tiivistelmä

Tämän Pro gradu -tutkielman tavoitteena oli tutkia grafeenin käyttöä biologisessa havainnoinnissa. Tutkielman teoreettinen osio aloitettiin lyhyella katsauksella grafeenin fysikaalisista ominaisuuksista. Osiossa esiteltiiny lyhyesti kaksi erilaista mittausasetelmaa: kanavatransistori ja usean elektrodin asetelma. Teoreettinen osio päätettiin esittelemällä kanavatransistorien käyttöä biologisten molekyylien ja elektrogeenisten solujen havainnoinnissa, sekä niiden hyödyntämistä neurobiologiassa.

Kokeellisessa osiosa tutkittiin grafeenin kykyä sammuttaa fluoresenssia päällystämällä se biotinyloidulla naudan seerumin albumiinilla (engl. bovine serum albumin), jonka biotiineihin kiinnitettiin avidiinia, johon oli kovalenttisesti sidottu väriainetta (fluoresiini isotiosyanaatti). Avidiini on proteiini, joka sitoutuu tiukasti biotiiniin. Molemmilla tutkituilla grafeenialueilla oli ruudukko kaksifotonihapetettua grafeenioksidia, joista eri ruutuja oli säteilytetty eri parametrien mukaisesti. Lisäksi eri alueilla sijaitsevilla ruuduilla oli eri leveydet. Osio pohjustettiin teoreettisella katsauksella mittaustekniikoista, naudan seerumin albumiinin kiinnittymisestä pintoihin, ja fluoresenssin sammumisesta sekä yleisesti että grafeenin tapauksessa. Näytettä tutkittiin ennen proteiinilla päällystämistä ja sen jälkeen optisella mikroskopialla, atomivoimamikroskopialla ja Raman-spektroskopialla. Proteiinilla päällystämisen jälkeen näytettä tutkittiin myös fluoresenssin elinaika -mikroskopialla.

Grafeenin integroitujen D- ja G-piikkien suhdetta ($I(\mathrm{D})I(\mathrm{G})^{-1}$) pidettiin materiaalin epäjärjestyksen mittarina. Sen havaittiin kasvavan säteilytysparametrien, laserpulssin energian ja säteilytysajan, kasvaessa. $I(\mathrm{D})I(\mathrm{G})^{-1}$ kasvaessa hapetettujen neliöiden korkeuden havaittiin kasvavan, odotusten mukaisesti, mutta myös säteilytetyn pinta-alan havaittiin vaikuttavan niiden korkeuteen. Fluoresenssin keskiarvoisen elinajan havaittiin riippuvan suoraan hapetetun neliön korkeudesta, ja Pearsonin R -arvo 0,95 saavutettiin molempien ruudukkojen lineaarisille sovituksille. Sovituksien kulmakertoimien ja leikkauspisteiden havaittiin eroavan merkittävästi keskenään, mikä viittaa neliöiden pinta-alan vaikutukseen. Tilanne neliöiden pinnalla vastaa todennäköisesti monien eri elinaikojen jakaumaa, joka aiheutuu väriainemolekyylien monista eri asennoista ja etäisyyksistä grafeenin pinnasta. Kaksi lineaarisesti käyttäytyvää elinaikakomponenttia pystyttiin erittelemään, mutta kolmas komponentti on ylisovittava.

Preface

This Master's thesis was conducted between June 2019 and May 2020 for the Department of Chemistry of University of Jyväskylä. The experimental measurements were carried out during the spring of 2020, and cut short by the restrictions imposed due to the COVID-19 pandemic. This deficiency has been compensated by additional theoretical work at the beginning of the experimental section.

I would like to thank my supervisor Mika Pettersson for the opportunity to work on this most interesting topic. I am especially grateful to Johanna Schirmer and Visa Ruokolainen for all the guidance and teaching, as well as for being always available and helpful. I am grateful to Suvi-Tuuli Akkanen, Johannes Parikka and Aku Lampinen for helping me, in their own ways, during and with the writing process. I would also like to thank almost everyone who has hanged out at Koppi during my years in Jyväskylä, you have been instrumental in making the city feel like home. Lastly, I would like to thank my dear Ilona, for your endless support and care.

Nivala
15.05.2020
Henri Kaaripuro

Contents

Abstract iii

Tiivistelmä iv

Abbreviations ix

Theoretical section 1

1 Introduction 1

2 Graphene 2

2.1 Structure . . . 2

2.2 Mechanical properties . . . 3

2.3 Electrical properties . . . 3

3 Graphene based devices 5

3.1 Field effect transistor . . . 5

3.2 Multielectrode arrays . . . 12

4 Operation of liquid gated graphene field effect transistors *in vitro* and *ex vivo* 13

4.1 Detection of simple molecules . . . 13

4.2 Detection of glucose . . . 17

4.3 Detection of DNA . . . 21

4.4 Detection of biomolecular response . . . 26

4.4.1 Detection of acetylcholine . . . 30

4.4.2 Detection of glutamate . . . 30

4.4.3 Detection of catecholamines . . . 32

4.5 FET detection array . . . 37

4.6 Detection of electrogenic cells 38

4.7 Effect of substrate 43

5 Applications of graphene based devices in neurobiology 45

6 Summary 49

Experimental section 51

7 Objectives 51

8 Theoretical background 51

8.1 On two-photon oxidized graphene 51

8.2 Surface chemistry of biotinylated BSA 52

8.3 Förster resonance energy transfer 53

8.4 Fluorescence quenching of graphene 55

8.5 Fluorescence of the probe molecule 57

8.6 Atomic force microscopy 58

8.7 Raman characteristics of graphene 60

8.8 Fluorescence of graphene oxide 61

8.9 Fluorescence lifetime imaging microscopy 62

9 Conduction of experiment 64

9.1 Protein coating of the chip 64

9.2 Optical microscopy 65

9.3 Atomic force microscopy 65

9.4 Raman 65

9.5 Fluorescence lifetime imaging microscopy 66

10 Results **67**

10.1 Optical microscopy 67

10.2 Atomic force microscopy 67

10.3 Raman 70

10.4 State of oxidation 72

10.5 Fluorescence lifetime imaging spectroscopy 74

10.6 Changes in lifetime 78

11 Discussion **82**

11.1 Damage to the first chip 83

12 Conclusions **85**

13 References **86**

Appendices **94**

Abbreviations

AFM	Atomic force microscopy
AP	Action potential
APBA	Aminophenylboronic acid
AuNP	Gold nanoparticle
BSA	Bovine serum albumin
b-BSA	Biotinylated bovine serum albumin
CSD	Cortical spreading depression
c-3-APBA	Covalently bound 3-APBA
DAN	1,5-diaminonaphthalene
dsDNA	Double strand DNA
EDL	Electric double layer
FET	Field effect transistor
FRET	Förster resonance energy transfer
FITC	Fluorescein isothiocyanate
FLIM	Fluorescence lifetime imaging microscopy
GA	Glutaraldehyde
GFET	Graphene field effect transistor
GluD	Glutamic dehydrogenase
GO	Graphene oxide
GOx	Glucose oxidase
LDR	Linear detection range
LGFET	Liquid gated field effect transistor
LGGFET	Liquid gated graphene field effect transistor
LOD	Limit of detection
MEA	Micro electrode array
mGluR	Metabotropic glutamate receptors
NAD	Nicotinamide adenine dinucleotide
nc-3-APBA	Non-covalently bound 3-APBA
nc-4-APBA	Non-covalently bound 4-APBA

PBASE	1-pyrenebutanoic acid succinimidyl ester
PBS	Phosphate buffered saline
PDMS	Polydimethylsiloxane
PEN	poly(ethylene naphthalene)
PET	Polyethylene terephthalate
PI	Polyimide
PtNP	Platinum nanoparticle
rGO	Reduced graphene oxide
SNR	Signal-to-noise ratio
ssDNA	Single strand DNA

Theoretical section

1 Introduction

Graphene was first isolated by Novoselov *et al.*[1] in 2004 by mechanical exfoliation, i.e. by peeling it from graphite with Scotch tape. Graphene is a two dimensional and robust, yet flexible material, which possesses excellent electrical properties. The most significant property of graphene for biological sensing is its complete biocompatibility, potentially allowing even implantable sensors. The graphene is sensitive to changes in ionic concentration and the presence of certain molecules. This alongside with multitude of known routes for functionalizing the graphene surface makes it an extremely promising material for sensors.[2] The reproducibility of graphene films and sensors is also a great advantage over similar devices fabricated with nanotubes or nanowires, as comparisons between devices become reliable.[3] *In vitro* and *in vivo* neurobiological signals are mostly studied using arrays of microelectrodes.[4] However, the rise of graphene based transistors is threatening this position as the transistors solve the most serious setbacks of microelecrodes, namely the increasing levels of impedance and noise as a function of decreasing device size.[5]

The most important applications of graphene that will not be included in this thesis are heterostructures of graphene and other two dimensional materials, the most notable of which is hexagonal boron nitride. Encapsulation of graphene in a 2D material brings out its best features. Two superposed 2D structures result in a smoother surface with lesser charged impurities, which naturally leads to better electronic properties. Hexagonal boron nitride is the most studied 2D coating material, as it brings an especially compatible lattice match.[2]

2 Graphene

2.1 Structure

Graphene is a planar, two-dimensional allotrope of carbon, that consists of sp^2-hybridized carbon atoms arranged in a hexagonal lattice. Carbon has four valence electrons, and a sheet of graphene is held together by three in-plane σ-bonds, with a bond length of 0.142 nm.[6] The last electron resides on the p orbital orthogonal to the carbon plane, leading to a filled π band. Graphene is also the basic building block of of numerous other nanocarbon allotropes, such as fullerenes and carbon nanotubes.

Although graphene is typically depicted as a flat surface, reality is different. It has been known for decades that perfect 2D crystals cannot exist on large scales at temperatures exceeding absolute zero, due to thermodynamic instability. What can happen, instead, is that the 2D structure exists as a part of a 3D system. For graphene, this system can be the substrate it was grown on top of, or the 3D system can rise due to deformations in the graphene, making it a 2D crystal in three dimensions. This type of deformation is called rippling.[7]

The crystal lattice of graphene itself can also contain imperfections. Topological defects are typically a pentagon or a heptagon replacing a six membered-ring in the lattice. The defects can also be Stone-Wales defects, in which four six-membered rings form a pair of five- and seven-membered rings. The formation of defects is made easier due to them causing out-of-plane bending in the lattice, lowering the formation energy.[8]

In addition to defects by irregularities in the ring structure, defects can also be formed by missing or having too many atoms in the lattice. Missing one or multiple carbon atoms from the lattice are called single and multiple vacancies respectively. Single vacancies leads to Jahn-Teller distortion and formation of a five- and a nine-membered ring. Missing multiple atoms has a wide variety of possible effects on the lattice, as the number of missing atoms and their locations can vary. Missing multiple atoms in a line leads to a one dimensional line defect. Line defects affect graphene's conduction properties, and they appear typically at grain boundaries.

As the lattice may be missing atoms, it can also have too many. Placing extra carbon atoms to the lattice is near impossible, due to the high energy requirement. Should extra atoms connect to the lattice, they must take advantage of the third dimension. The covalent bonding is conducted by sp^3 hybridized carbons that appear locally. The possible sites for the extra carbons to attach to are at bridge positions and on top of the underlying carbon atoms. If the attaching atom is not carbon, bonding between the two depends on the strength of their interaction. Plethora of bonding configurations are possible, depending on the interactions, as are many different bonding locations, usually corresponding to high-symmetry positions. A foreign atom can also be substituted to a vacancy in the lattice as a substitutional impurity.[9]

Graphene oxide (GO) is modified graphene that contains functional groups of oxygen including, but not limited to, epoxides, alcohols and carboxylic acids. It is easily fabricated into single sheets, which is most definitely a sought after attribute. GO is too insulating as is, but it can be readily reduced *via* hydrazine hydrate vapor into reduced graphene oxide (rGO). The treatment restores conduction through the film, but does not completely remove the oxygen based defects. Approximately 25 % of carbon atoms remain oxidized after the treatment, most of the defects being carboxyl groups.[10] The amount of active sites surviving the hydrazine treatment can be altered by functionalizing the GO surface beforehand by groups like ethylenediamine.[3] Nitrogen doping of graphene can be achieved by creating the graphene from a nitrogen containing polymer. Like oxygen, nitrogen also offers active binding sites on the surface of graphene.[11]

2.2 Mechanical properties

Graphene is known to be light, strong and flexible. The density of graphene is only $0.77\,\mathrm{mg\,m^{-2}}$. The amount a material deforms when exposed to a force is given by the material's Young's modulus, and the amount of tension a material can withstand before breaking is given as the material's tensile strength. The Young's modulus of graphene is1 TPa, and its tensile strength 130 GPa.[12] The corresponding values for steel[13] are 180 MPa and 860 MPa respectively, making graphene many times more durable. Should one make a 1 $\mathrm{m^2}$ hammock out of graphene, it could hold 4 kg's of weight before breaking, thus being able to hold a common house cat on a near invisible surface that weights as much as one of the cat's whiskers.[14]

2.3 Electrical properties

Graphene is a zero-gap semimetal that can have charge carrier mobility in of over $200\,000\,\mathrm{cm^2\,V^{-1}\,s^{-1}}$.[15] For reference, silicon has electron mobility of less than $1400\,\mathrm{cm^2\,V^{-1}\,s^{-1}}$ and hole mobility of $450\,\mathrm{cm^2\,V^{-1}\,s^{-1}}$.[16] The quasiparticles in graphene are described using a Dirac-like Hamiltonian

$$\hat{H}_0 = -i\hbar v_F \boldsymbol{\sigma} \nabla, \tag{1}$$

where i is the imaginary unit, $\hbar$ the reduced Planck constant, $v_F \approx 10^6\ \mathrm{ms^{-1}}$ the Fermi velocity; $\boldsymbol{\sigma}$ denotes the Pauli matrices and ∇ the differential operator. Equation (1) is accurate when many-body effects are neglected. The use of the Dirac-like equation instead of Schrödinger's equation is due to the crystal structure of graphene. The hexagonal lattice of graphene can be divided into two equivalent, triangular and interpenetrating sublattices. Quantum hopping between these two lattices results in two cosine-like energy bands that intersect at the edges of the Brillouin zone. The energy of the quasiparticles in graphene follows a linear dispersion relation, like massless relativistic particles,

$$E = hkv_F, \tag{2}$$

where h is the Planck constant. Linear dispersion relation leads to a conical energy spectrum near the Fermi energy that differs from the parabolical spectrum of conventional metals and semiconductors. This rises the zero-gap characteristic of graphene, as the density of states at the intersection is extremely small. The electronic structure is further illustrated in figure 1.

The current carrying states in graphene, as in most semiconductors, are negatively charged and electron-like at energies above zero. At negative energies, the unoccupied states (holes) carry current as positively charged quasiparticles. In typical condensed matter physics, electrons and holes are described using separate and unconnected Schrödinger's equations. However, due to the sublattice description, they are connected in graphene. This makes their behavior analogous to quantum electrodynamics. This allows for introduction of chirality to the system. Due to the quantum mechanical character of graphene, it has a minimum conductivity of $4\ e^2h^{-1}$.[17,18]

Graphene can be both p- and n-doped to affect its electric properties. The doping can be electrical or chemical, the former conducted by applying an electric field to the graphene, and the latter by infusing foreign chemical species into the graphene layer or its surface. Electrical doping affects the populations in the Dirac cones, whereas chemical doping shifts the Fermi point. Chemical doping can also be used for tuning of the band gap.[1,19] Graphene band gap can also be affected by applying strain to the graphene layer, forming the graphene into nanoribbons, or by having bilayer graphene.[20]

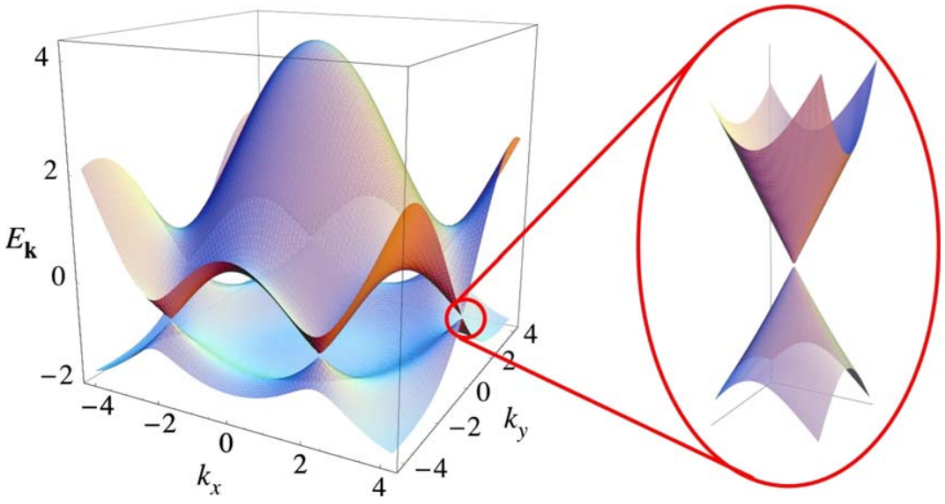

Figure 1. The band structure of graphene, in units of eV. The inset on the right is a zoom in of the conincal band structure at the Dirac points. Reprinted figure with permission from reference 17. Copyright 2009 by the American Physical Society.

3 Graphene based devices

3.1 Field effect transistor

Transistors are the heart of modern electronics. The first functioning transistor was a point-contact transistor invented in 1947. It never achieved commercial success, but the junction transistor released a month later did.[21] The research of transistors warranted the Nobel Prize in physics in 1956 to William Bradford Shockley, John Bardeen and Walter Houser Brattain, "for their researches on semiconductors and their discovery of the transistor effect."[22]

Semiconductors are an integral part of transistors, the most utilized of which are silicon and germanium. Their conducting characteristics are usually tuned by doping, for example by adding phosphorus to silicon, to increase the amount of conducting electrons. Semiconductors are divided into two classes: p-type semiconductors conduct electricity *via* holes, and n-type semiconductors *via* electrons. It is worth mentioning, that regardless of the free-to-move electrons or holes, the semiconductors are still electrically neutral. Although they are neutral, they have different concentrations of different charge carriers, making the junction of special interest. This leads to electrons diffusing from the n-type side to the p-type side and combining with the holes there, and vice versa. This creates a depletion layer near the junction. The existence of negative and positive charge carriers on opposite sides of the layer creates an electric field across it, producing a potential barrier that an incoming charge carrier must overcome.

A field effect transistor (FET) is a pnp- or a npn-junction. FETs are used widely, and they are characterized by high input resistance and small dimensions. An n-type insulated gate FET is created by forming n-regions on a slab of p-type semiconductor, according to figure 2. The gate can be top or back gated or both. Attaching electrical connects to the slab forms the source and drain electrodes. An insulating layer is placed between the semiconducting slab and the gate electrode, so that no current can flow to the terminal. The material of the insulating layer can be anything from metal oxides to liquids. The thin channel between the source and drain electrodes is a conduction path. The gate and the middle part semiconductor on the other hand resemble a capacitor. Applying voltage to the gate will thus effect the amount of mobile charge carriers in the conduction path, changing its apparent thickness.[23]

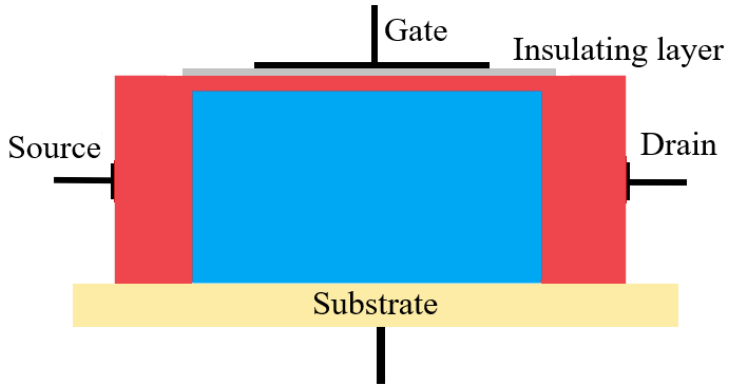

Figure 2. A schematic representation of a insulator gated field effect transistor. Red and blue colors represent n- and p-type semiconductors, which are interchangeable.

For modern high-speed applications, the transistor should respond quickly to changes in the gate voltage. These can be achieved by having short conducting channels that have fast electron carriers. A short conducting channel comes with disadvantages, such as lowering of threshold voltage. A way of fighting short channel effects, according to scaling law, is having thin conduction channels accompanied by a thin gate controlled region. Besides a fast response time, a good transistor should also have a on-off current ratio I_{on}/I_{off} between 10^4 and 10^7.[20]

$I_{DS}-V_G$ characteristics of a transistor consist of two regions. The first is a linear (ohmic) region, and the second is saturation region. After the linear region, at a so called pinch-off voltage, the current reaches an essentially constant value, and no increase of voltage is going to change it. In the linear region, a transistor's $I_{DS}-V_G$ characteristics are proportional to

$$I_{DS} = \frac{W}{L} C_{int}\, \mu\, (V_{GS} - V_{Dirac})\, V_{DS}, \tag{3}$$

where I_{DS} is the drain-to-source current, V_{GS} the gate-to-soure potential, V_{Dirac} the Dirac point potential, V_{DS} the drain-to-source potential, C_{int} the interface capacitance, μ the charge carrier mobility, W the width of the channel and L its length. From this, device transconductance is defined as

$$g = \frac{dI_{DS}}{dV_{GS}} \approx \frac{\Delta I_{DS}}{\Delta V_{GS}}. \tag{4}$$

Transconductance is the inverse of resistance and relates the current through the device to the gate-to-source voltage. In the linear region, it is simply the slope of the curve. As the source-to-drain connection is controlled by the gate, the maximum transconductance values (g_m) connecting these are typically used for characterization of device performance. Another important characteristic that is sometimes used for comparison of devices is the charge carrier mobility

$$\mu = \frac{W}{L} \frac{g}{C_{int} V_{DS}}. \tag{5}$$

It is important to note that both of these quantities are proportional to the dimensions of the

transistor. Thus, one should compare the area-normalized transconductance ($g_m \square$) values for information of device performance. Quantities are area-normalized when their W/L ratio is unity. As transconductance is also a function of V_{DS}, compared values are often normalized also with respect to it ($g_m \square V_{DS}^{-1}$).[24,25]

As graphene is a one atom thick semiconductor with a tunable bandgap, it is an attractive material for FETs. Devices with gate lengths as small as 40 nm have been created. The output characteristics of graphene FETs (GFET) contain a couple of interesting properties. Device transconductances in GFETs can be nearly constant over a significant V_{GS} range with little to no saturation, due to the absence of band gap in graphene.[20] However, a certain nonlinearity can be observed in GFETs: the $I_{DS} - V_G$ characteristics are typically V-shaped. At low drain-source voltages V_{DS} the GFET operates in a linear region, lowering the transconductance as a function of increasing voltage. As V_{DS} continues to increase, the potential conditions at the drain end of the transistor start to match those of the Dirac point, and a curve is formed in the graph. As V_{DS} continues to increase, the transconductance starts to increase linearly. This effect is due to the ambipolarity of graphene: graphene transfers from a n-type semiconductor to a p-type semiconductor during the curve.[20,26] Two example curves for a top and bottom gated GFET with different back gate voltages are presented in figure 3.

Applying gate voltage to the GFET creates a capacitor between the gate and the graphene layer, where the gate voltage V_G is proportional to the Fermi level E_F, elementary charge e and geometrical capacitance ϕ

$$V_G = \frac{E_F}{e} + \phi. \tag{6}$$

The last term is caused by the dielectric and it dominates in back gated systems, whereas the

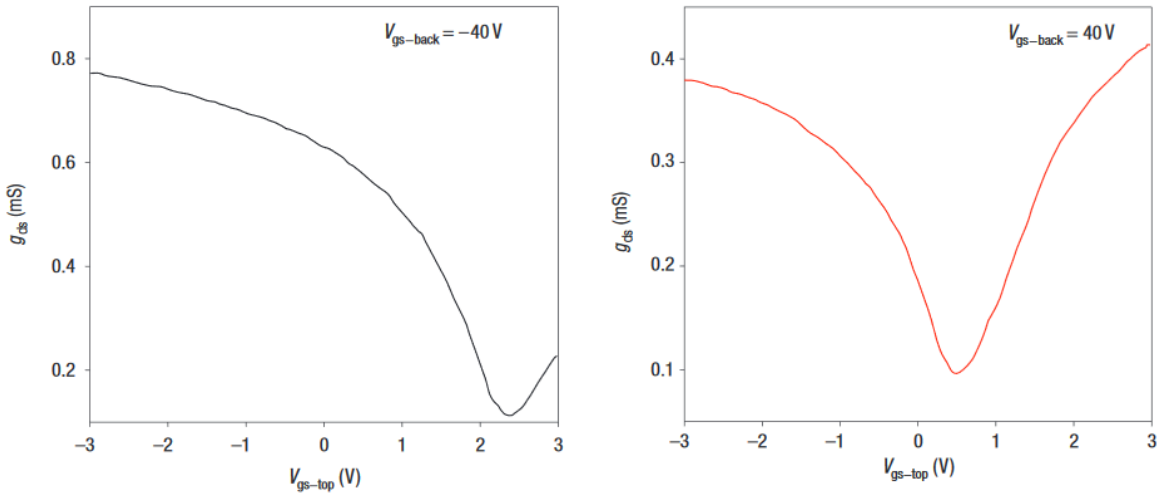

Figure 3. Transconductance as a function of gate-to-source voltage for a top and bottom gated GFET. Here the two linear regions are discernible, as well as the Dirac point. Asymmetry between hole and electron conducting regions is also clearly visible. Reprinted by permission from Springer Nature: reference 26, copyright 2008.

first term is caused by the graphene's quantum capacitance. In top gated, and especially liquid gated, devices the terms are of the same magnitude.[27] Capacitance of graphene in an electrolyte can be divided into three parts: one emerging due to the electrolyte-electrode double layer, the second due to the hydrophobicity of graphene, and the last due to density of carriers near the Dirac point, called quantum capacitance. Capacitance due to electrical double layer (EDL) can be calculated using equation[28]

$$C_{\mathrm{EDL}} = \frac{k_{\mathrm{EDL}}\varepsilon_0}{\lambda_{\mathrm{D}}}, \quad \lambda_{\mathrm{D}} = \frac{0.304}{\sqrt{M}}, \tag{7}$$

capacitance due to graphene hydrophobicity using equation[25]

$$C_{\mathrm{airgap}} = \frac{k_{\mathrm{air}}\varepsilon_0}{d}, \tag{8}$$

and quantum capacitance using equation[29]

$$C_{\mathrm{Q}} = \frac{2e^2}{\hbar v_{\mathrm{F}}\sqrt{\pi}}\sqrt{|n_{\mathrm{G}}| + |n^*|}, \quad n_{\mathrm{G}} = \left(\frac{eV_{\mathrm{GS}}}{\hbar v_{\mathrm{F}}\sqrt{\pi}}\right)^2. \tag{9}$$

In these equations, k_{EDL} is dielectric permittivity, considered the same as water, ε_0 is vacuum permittivity, λ_{D} is Debye length, M is the molarity of the solution, k_{air} the dielectric permittivity of air, d is the thickness (estimated as 0.32 nm), e is the elementary charge, n_{G} the gate potential induced charge carrier concentration, n^* impurity induced charge carrier concentration, and V_{GS} the applied gate potential. Equation (8) is taken into account for hydrophobic materials and high ionic concentrations because otherwise ions would be modeled as being unrealistically close to the surface. The three capacitances should be treated as a series of three capacitors. It is noteworthy, that quantum capacitance is only proportional to the density of charge carriers, and linearly proportional to the gate voltage. The capacitance has a V-shape with a round minimum at the Dirac point, and is symmetric with regard to it.[29]

Due to the capacitor that is formed between the gate and the conducting channel, FETs are severely limited in performance at high frequencies of operation.[23] The highest cut-off frequency achieved for a GFET is 100 GHz, for a gate length of 240 nm.[30] Highest cut-off frequency available for a silicon transistor of equivalent size is 53 GHz for a 550 nm device.[20]

For the purposes of biological sensing, liquid gated GFETs (LGGFET) are of vital importance. A basic device consists of source and drain electrodes, a sheet of graphene, electrolyte for the gate and a reference electrode. The electrodes must be coated with an insulator to avoid short circuiting the device through the electrolyte, and the electrode needs to be surrounded with a chamber to confine it in place. A schematic presentation is presented in figure 4. A circuit diagram of a typical LGGFET is presented in figure 5. C_{elec} and C_{gra} denote the total capacitances

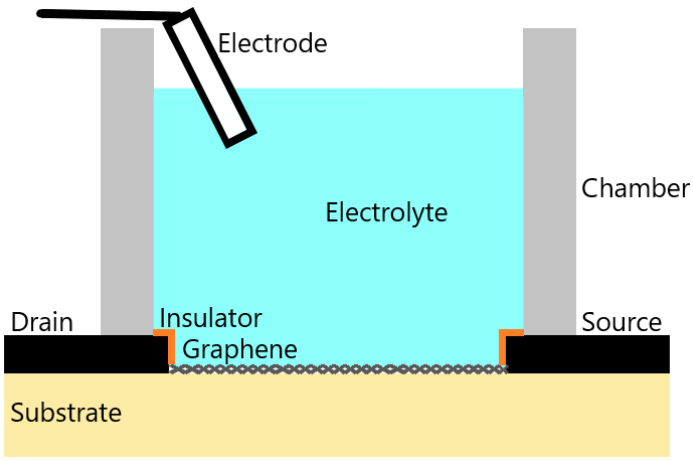

Figure 4. A schematic presentation of a liquid gated graphene field effect transistor.

at the electrode and graphene surfaces, respectively. R_{acc} is the access resistance between the graphene surface and the source and drain electrodes. The access resistance arises due to a pn-junction at the graphene-electrode interface, and it is a contributor to the asymmetry of electron and hole conducting regions in the $I_{\mathrm{DS}} - V_{\mathrm{G}}$ curves. The pn-junction itself is formed because of substrate doping of the graphene energy levels. For example, graphene grown epitaxially on SiC is expected to be n-doped, leading to restricted hole conduction.[31] The access resistance lowers a device's extrinsic transconductance from the intrinsic value available from the graphene.[32]

The electrochemical gate in LGFETs has better performance than classical silicon gated devices with regard to tuning of charge carriers. This is due to the electrochemical capacitance, making the effective distance between the gate electrode and graphene much smaller than the thickness of silicon gates is. When there are only a few charge carriers, graphene's transport is dominated by impurities in the substrate due to Coulomb scattering. In the case of a liquid gate, impurities can be thought of as the concentration of electrolytes. It has been shown that the conductivity

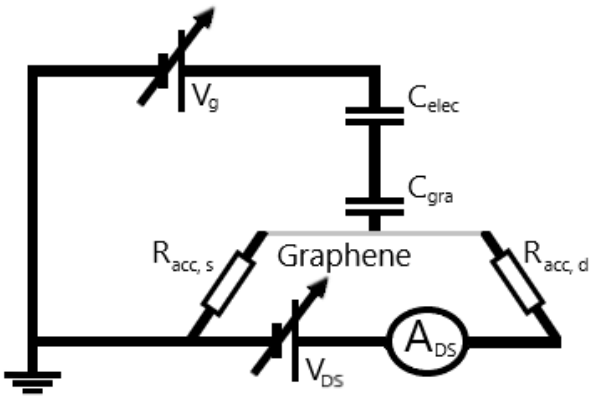

Figure 5. A circuit diagram of a typical LGGFET. C_{elec} and C_{gra} are the capacitances at the electrode and graphene surfaces respectively, and $R_{\mathrm{acc,\,s}}$ and $R_{\mathrm{acc,\,d}}$ the source and drain access resistances respectively.

of electrolytically gated graphene lowers as a function of increasing molarity of the electrolyte. The studied electrolytes contained only chemically inert molecules and ions, making physical changes in the graphene an unfeasible explanation.[33]

Graphene LGFETs can also be made to measure without the effect of a substrate, for example by etching the substrate off. This is especially attracting as the substrate is known to cause shifts in the Dirac point because of impurities that cannot be controlled. There are several distinct advantages to utilizing suspended graphene devices: the Dirac point is at 0 V in pH 7, their transconductance values can reach up to two times the values of comparable SiO_2 based devices, and an apparent reduction in the asymmetry of transconductance in n- and p-doped regions. Etched devices also have lower amounts of noise, again due to the absence of the effects of the substrate and its oxides.[34]

Graphene devices have remarkably low levels of noise. This is due to a couple of reasons: the high conductivity of graphene leads to low Johnson noise even in the presence of few charge carriers, and graphene having only few crystal defects which produces only little excess noise from their thermal switching.[35] Effective gate noise in LGFETs can be calculated according to

$$U_{\mathrm{G,\,RMS}} = \sqrt{\int_{f_1}^{f_2} \frac{S_\mathrm{I}}{g_\mathrm{m}^2} \mathrm{d}f}, \tag{10}$$

where $U_{\mathrm{G,\,RMS}}$ is the root-mean-squared gate noise, S_I is the power spectral density of I_DS and g_m the transconductance at a certain U_DS, and f_1 and f_2 are the limits of integration. Random charge fluctuations close to the transistor induce voltage fluctuations. Thus, augmented charge model can be used to model power spectral density as

$$S_\mathrm{I} = S_\mathrm{IN}\, g_\mathrm{m}^2 + A_\mathrm{S} \left(\frac{R_\mathrm{S}}{R_\mathrm{DS}} \right)^2 I_\mathrm{DS}^2, \tag{11}$$

where S_IN is the current noise power from random charge fluctuations, A_S is the resistance noise amplitude, R_DS the total resistance and R_S the access resistance. The last term represents the noise due to the exposed graphene interface, and it shows a clear f^{-1} dependence. Writing

$$\alpha_\mathrm{R} = A_\mathrm{S} \left(\frac{R_\mathrm{S}}{V_\mathrm{DS}} \right)^2 = A_\mathrm{S} \left(\frac{R_\mathrm{S}}{R_\mathrm{DS}} \right)^2 I_\mathrm{DS}^2, \tag{12}$$

we can write $U_{\mathrm{G,\,RMS}}$ as

$$U_{\mathrm{G,\,RMS}} = \sqrt{\int_{f_1}^{f_2} \frac{S_\mathrm{IN}\, g_\mathrm{m}^2 + a_\mathrm{S} I_\mathrm{DS}^4}{g_\mathrm{m}^2} \mathrm{d}f}, \tag{13}$$

where S_IN and α_S are used as fitting parameters. This equation needs to be fitted separately on both sides of the Dirac point, due to the differing access resistances. Sample spectra for

power spectral density and $U_{G,\,RMS}$ are provided in figure 6. The measured device was a typical LGGFET on a polyimide (PI) substrate, and noise values are given for an unbent device as well as a device that has been bent a number of times.[36]

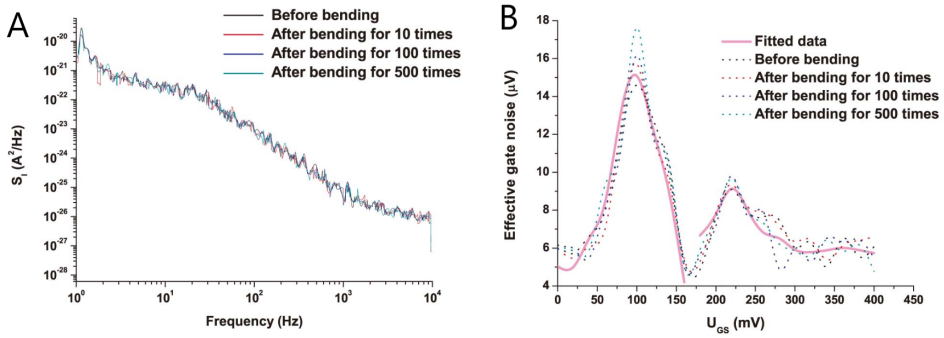

Figure 6. A) power spectral density of a typical LGGFET. B) Effective gate noise at U_{DS} = 200 mV, with Dirac point visible at U_{GS} = 160 mV. Copyright 2014 IEEE.

3.2 Multielectrode arrays

Multielectrode arrays (MEA) are, as the name states, arrays of microscopical electrodes. They have been used for decades even in biological sensing. This was made possible by the development of photoetching, and desireable by the arrays' ability to measure multiple points in a culture of cells or tissues non-destructibly over long periods of time.[37] Good signal-to-noise ratios (SNR) have also been available for a long time in MEAs.[38]

Traditional materials for fabricating MEAs are titanium and titanium nitride, among others. These have the downside of being opaque. Indium tin oxide (ITO) can be used to partially solve this problem, but it still requires that the electrode sites are non-transparent. Graphene is suitable for replacing these materials as it is both transparent and mechanically robust, while offering excellent conductive properties. Fabricated graphene MEAs have also proven to be stabile in aqueous solutions.[39] A schematic representation of a single graphene electrode is presented in figure 7.

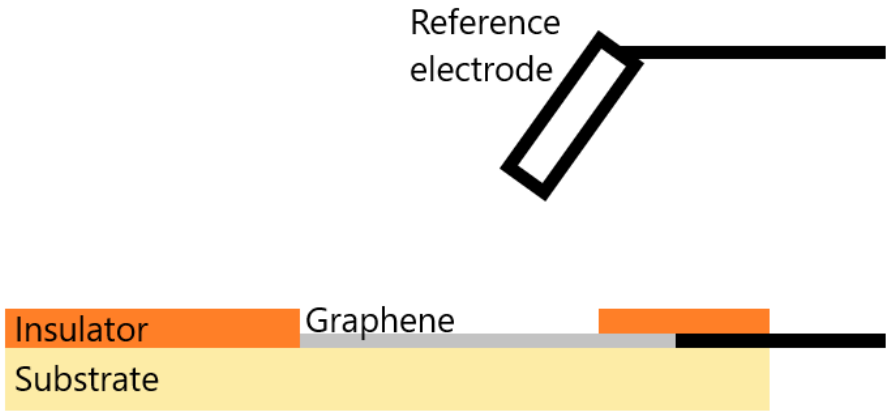

Figure 7. A schematic of a single graphene electrode.

4 Operation of liquid gated graphene field effect transistors *in vitro* and *ex vivo*

In vitro and *ex vivo* sensing of biological moieties can be conducted by using graphene LGFETs. Graphene is sensitive to changes in the liquid environment due to its electrical properties. It is especially notable that graphene can detect both positive and negative carriers due to its ambipolar character. The conductance properties can change due to chemical or biological molecules adsorbing onto the surface and acting as electron donors or acceptors.[40] LGFETs have been shown to be more readily doped with charge carriers than classical back gated silicon FETs, increasing their sensitivity.[27] A typical LGGFET has dimensions of one to some tens of micrometers, which is smaller than a standard cell, but larger than the smallest parts of nerve cells.[2,25]

Modification of the graphene surface is often conducted to increase the selectiveness of detection. The graphene surface can have aromatic systems non-covalently attach to it *via* π-π stacking. The attaching groups can be chosen probe molecules, such as DNA, or linker molecules, like 1-pyrenebutanoic acid succinimidyl ester (PBASE), that can bind to the actual probe molecule. A schematic presentation of a typical LGGFET with a PBASE connected probe molecule is presented in figure 8. The graphene can also be modified by oxides or amides, to create active sites for attachment.[11,41,42] A plethora of different devices are presented in the following sections. To ease comparison between devices, each paragraph is concluded with a table of the most important parameters for the presented devices. In the tables, LOD refers to the limit of detection and LDR to the linear detection range.

4.1 Detection of simple molecules

Capacitances in liquid gated FETs are notably higher than in back gated ones, giving them better transfer characteristics and making them more suitable for applications. Furthermore, the transconductances are also two orders of magnitude larger in electrolytes than in vacuum. The transfer characteristics are affected by the concentration of electrolytes in the top gate. This can be seen as a linear dependence of conductance on pH, and has been demonstrated by Ang *et al.*[43] and Ohno *et al.*.[40] The former had devices fabricated with 1 – 2 layers and 3 – 4 layers of unfunctionalized epitaxial graphene, and the latter had devices fabricated with a single graphene layer. The dependence of conductance on pH is due to the OH^- and H_3O^+ ions interacting with the electric double layer, causing a polarization effect in the graphene, much like the one caused by a top gate.[43] The measured conductivities and linear fits for the pH dependencies are presented in figure 9.

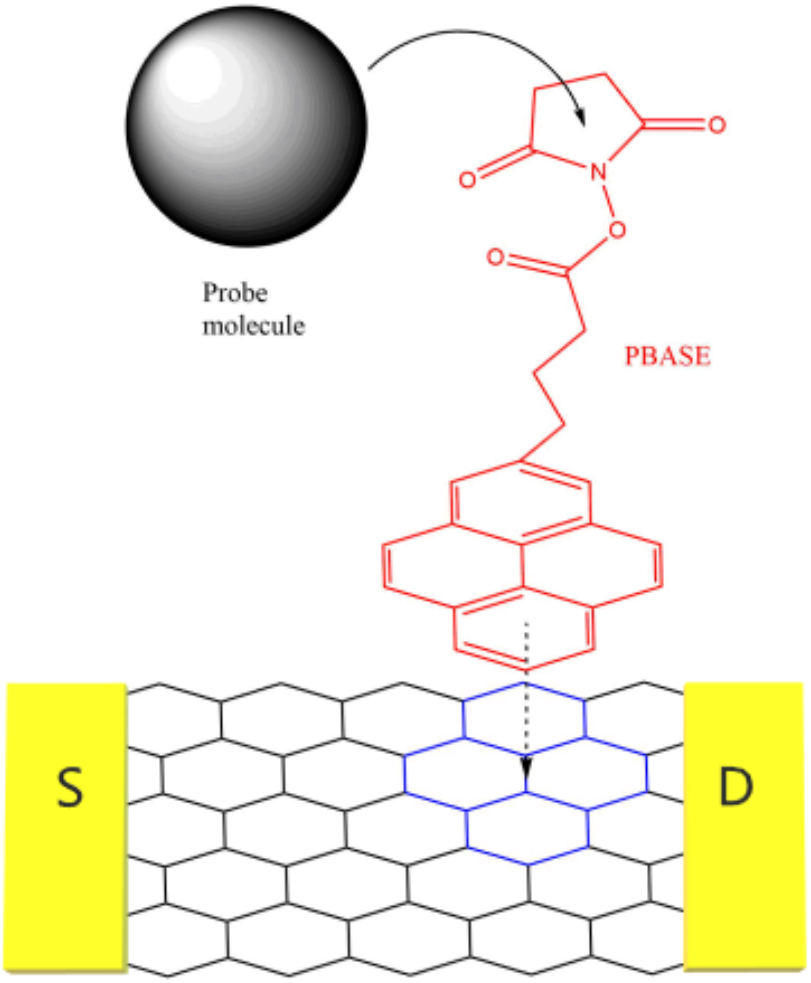

Figure 8. A schematic representation of functionalizing a graphene surface using PBASE and probe molecules. PBASE is adsorbed onto the surface *via* $\pi - \pi$ stacking, followed by covalent bonding between the probe molecule and the amide of the PBASE.

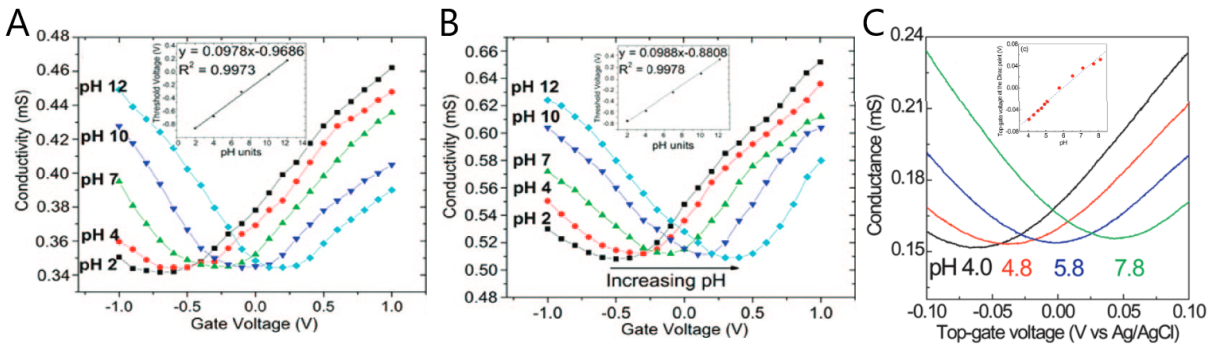

Figure 9. The measured conductivities for A) 1 – 2 layer graphene device, B) 3 – 4 layer graphene and C) single layer graphene. The insets show the linear fits for the pH dependence. A) and B) reprinted with permission from reference 43. Copyright 2008 American Chemical Society. C)Reprinted with permission from reference 40. Copyright 2009 American Chemical Society.

In a similar way, LGFETs can be used as label free sensors for biological molecules. Ohno *et al.*[40] have shown that bovine serum albumin (BSA), charged negatively by pH control, adsorbs

to the surface of the graphene and changes its conductive properties. The adsorption of BSA was noted to follow the Langmuir adsorption isotherm

$$\frac{C_{\mathrm{BSA}}}{\Delta G} = \frac{C_{\mathrm{BSA}}}{\Delta G_{\mathrm{max}}} + \frac{K_{\mathrm{d}}}{\Delta G_{\mathrm{max}}}, \tag{14}$$

where C_{BSA}, ΔG, ΔG_{max} and k_{d} are the concentration of BSA, the change in conductance, the conductance at saturation, and the dissociation constant of the interaction between BSA molecules and graphene respectively. However, more experiments were deemed necessary for verification. A spectrum for a real time measurement of conductance as a function of BSA concentration is presented in figure 10 A and a linear fit of $C_{\mathrm{BSA}}\,\Delta G^{-1}$ as a function of C_{BSA} according to equation (14) in figure 10 B.[40]

Selective detection of simple molecules has also been conducted, by using modified bilayer graphene. Having a bilayer causes a band gap in the graphene. Park *et al.*[44] used a LGGFET functionalized by the human olfactory receptor 2AG1 (hOR2AG1:OR) to detect amyl butyrate, which it binds specifically to. The bilayer graphene was first functionalized by either oxygen plasma treatment for p-type doping or ammonia plasma treatment for n-type doping, i.e. the ambipolar characteristics of graphene were removed. The graphene surface was coated with 1,5-diaminonaphthalene (DAN), that connected to the graphene *via* $\pi - \pi$ interactions of the carbon rings. This was done to immobilize the receptor to the surface, which was supposed to improve stability. The surface was then functionalized by glutaraldehyde (GA), followed by the actual olfactory receptor. The substrate was flexible polyethylene terephthalate (PET).

Using the devices, the group was able to detect the presence of amyl butyrate as a change in the device's drain-to-source current as a function of amyl butyrate's concentration. The measurements were also conducted using a LGFET constructed with pristine graphene, which had a stable transconductance regardless of the butyrate's concentration. The sensitivity of the devices was considerably high, as they were able to detect concentrations as low as 0.04 fM with SNR of 4.2. Because the olfactory receptor exists in an equilibrium with its negatively charged state, the receptor acts as a p-doper for the graphene. This leads to the oxygen treated graphene being somewhat more sensitive than the ammonia treated one. The interaction of target molecules with the detector was found to follow the Langmuir adsorption isotherm, supporting the findings of Ohno *et al.*.[40] The normalized sensitivity of the devices was derived as

$$N = \frac{C}{K^{-1} + C}, \tag{15}$$

where C is the concentration of the target molecules, and K is the equilibrium constant between the target molecules and the receptor. The devices were also tested with other molecules that only differed by the number of carbon atoms from the target molecule (hexyl butyrate, propyl butyrate, butyl butyrate). There was no significant alteration of the signal detected before a

concentration of 1 mM was reached, highlighting the great selectivity of the devices. Real time measurements of normalized change in drain-to-source current as a function of butyl amyrate concentration are shown in figure 10 C and the normalized change in drain-to-source current in figure 10 D for both the n-noped and the p-doped devices. In the latter figure, a linear detection range between 0.04 fM and 40 pM is discernible.

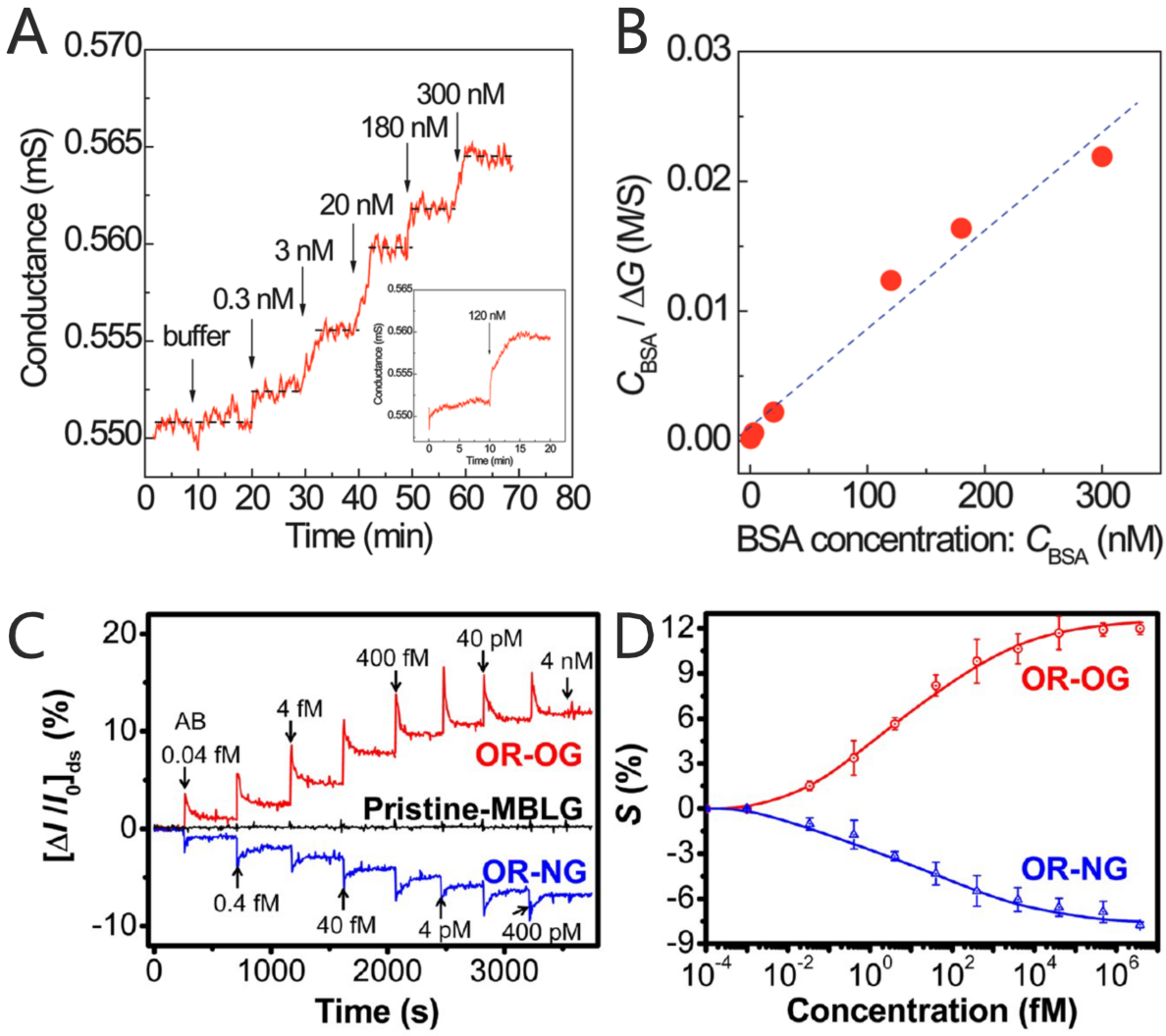

Figure 10. A) The real time measurement of conductance as a function of BSA concentration, B) linear fit of $C_{\mathrm{BSA}}\,\Delta G^{-1}$ as a function of C_{BSA} according to equation (14), C) real time measurement of normalized drain-to-source current as a function of butyl amyrate concentration for p- doped (red) and n-doped (blue) LGGFETs, with non-functionalized device (black) for reference, and D) normalized drain-to-source current as a function of butyl amyrate concentration for p- doped (red) and n-doped (blue) LGGFETs with discernible linear region. A) and B) reprinted with permission from reference 40. Copyright 2009 American Chemical Society. C) and D) reprinted with permission from reference 44. Copyright 2012 American Chemical Society.

Table 2. Details of the discussed LGGFETs for detecting small molecules

Material	Functionalization	W/L	LDR [target]	Substrate	Year	Ref
Few-layer graphene	None	500x500 μm^2	2 – 12 [pH]	SiC	2008	43
Graphene	None	-	4.0 – 8.2 [pH]	SiO_2/Si	2009	40
Graphene	None	-	0.3 – 300 nM[BSA]	SiO_2/Si	2009	40
Bilayer graphene	hOR2AG1:OR *via* GA *via* DAN	4000x200 μm^2	0.04 fM – 40 pM [amyl butyrate]	PET	2012	44

4.2 Detection of glucose

Glucose, or dextrose, is a common monosaccharide. Abnormal amounts of glucose in blood or other bodily fluids is associated with multiple diseases, such as diabetes mellitus. For people with diabetes, devices that can measure accurately for long periods of time and with minimal intrusion would be optimal.[45,46] Non-intrusive measurements would mean measuring glucose levels in body fluids. As the concentration of glucose is lower in body fluids than in blood, higher precision is required from the measuring apparatus. Glucose has been noted to have no effect on pristine graphene sensors, but it can be oxidized in a reaction catalyzed by glucose oxidase (GOx) according to reaction equation 1.

$$\beta\text{-D-glucose} + O_2 + H_2O \longrightarrow \text{D-glucono-1,5-lactone} + H_2O_2$$

Reaction equation 1. Oxidation reaction of glucose.

Graphene can be functionalized by GOx *via* linker molecules, such as PBASE, using the same principle shown in figure 8. Detection of glucose using GOx is done indirectly, as the enzyme does not incur any notable changes in the graphene's conductive properties.[47,48] Instead, the LGGFET reacts with the H_2O_2 byproduct according to reaction equation 2, which increases the conductivity of graphene.

$$2\ H_2O_2 \longrightarrow O_2 + 2\ H^+ + 2\ e^-$$

Reaction equation 2. Oxidation reaction of H_2O_2.

If the detected response was due to electron transfer generated by the oxidation reaction of glucose, graphene conductance should be lowering. Instead the conductance increases due to electrons transferring from the graphene to oxidize the hydrogen peroxide.[45,47] The groups of Huang[47] and Kwak[48] both fabricated simple LGGFETs functionalized by GOx *via* PBASE. Both groups also stated an exponential relation existing between the change in drain-to-source

current and the concentration of glucose, but neither provided any additional parameters. Example spectra from the latter group, for a flat and a bent device, are provided in figure 11.

GFETs functionalized by GOx have a downside of saturating, which may be because of limited density of GOx on the graphene surface, or because of limited reaction rate.[47] The amount of GOx available on the surface can be increased by silk encapsulation as the hydrophobic interaction between the two components results in a more rigid and stabile GOx structure. Wet silk-GOx film naturally adheres to a graphene surface, creating a strong and robust interface. In a setup such as this, the GOx reacts with the glucose that has diffused through the film layer, which also acts as the top gate. Real time measurement of the change in drain-to-source current at the Dirac point as a function of glucose concentration and the effect of some common interfering agents is shown in figure 12 C and the linear relation between glucose concentration and the change in the drain-to-source voltage in figure 12 D.[49]

Zhang *et al.*[45] have also presented a GFET based on GOx bound to a polymer matrix. Their device had the semiconducting channel of pristine graphene. The functionalization was conducted on the gate electrode instead. The electrode was first coated with graphene, followed by addition of platinum nanoparticles (PtNP), that were coated with a thin layer of Nafion. The functionalization was finished by a coating of a mixture of chitosan and GOx. Nafion and chitosan are both biocompatible polymers, and Nafion is used to help the chitosan-GOx layer to adhere to the graphene surface. The function of the platinum nanoparticles is to enhance the electrocatalytic activity on top of the graphene layer, and their average size was approximately 30 nm. It was also noted, that the amount of nanoparticles on top of the graphene naturally affected the sensitivity of the device. Assuming that the potential drops at the electric double layers at the gate electrode and the graphene surface follow the Nernst equation, the effective gate voltage change can be written as

$$V_{\mathrm{G}}^{\mathrm{eff}} = (1+\gamma)\frac{kT}{q}\ln[\mathrm{H_2O_2}] + \mathrm{C}; \qquad \gamma = \frac{C_{\mathrm{graphene}}}{C_{\mathrm{gate}}}, \tag{16}$$

where k is the Boltzmann constant, T the absolute temperature, q the electronic charge, C a con-

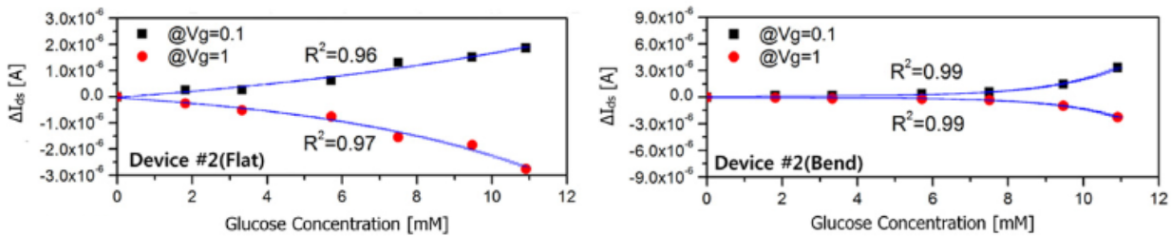

Figure 11. Exponential dependence of ΔI_{DS} on glucose concentration in a GOx based LGGFET in p- and n-doped situations for a flat and bent configurations of the same device. Reprinted with permission from reference 48, copyright 2012, with permission from Elsevier.

stant, $[H_2O_2]$ the concentration of hydrogen peroxide, $C_{graphene}$ the capacitance of the graphene channel and C_{gate} the capacitance at the gate surface. Real time measurement of the drain-to-source current at the Dirac point as a function of glucose concentration and the change in the effective gate voltage as a function of glucose concentration are presented in figures 12 A and B, respectively.

Regardless of its common usage, GOx functionalized graphene is not the only available method for detecting glucose. For example, Vasu *et al.*[46] have demonstrated the usage of aminophenylboronic acid (APBA) functionalized rGO in detecting glucose. The sensing of glucose is based on ester bonds forming between glucose and boronic acid, which leads to changes in graphene conductivity. APBA can be attached to the graphene surface non-covalently *via* $\pi - \pi$ interactions, or by covalent bonding between the amino groups of APBA and the carboxyl groups of rGO. The group studied three kinds of functionalizations for the devices: non-covalently bound 4-APBA (nc-4-APBA), non-covalently bound 3-APBA (nc-3-APBA)

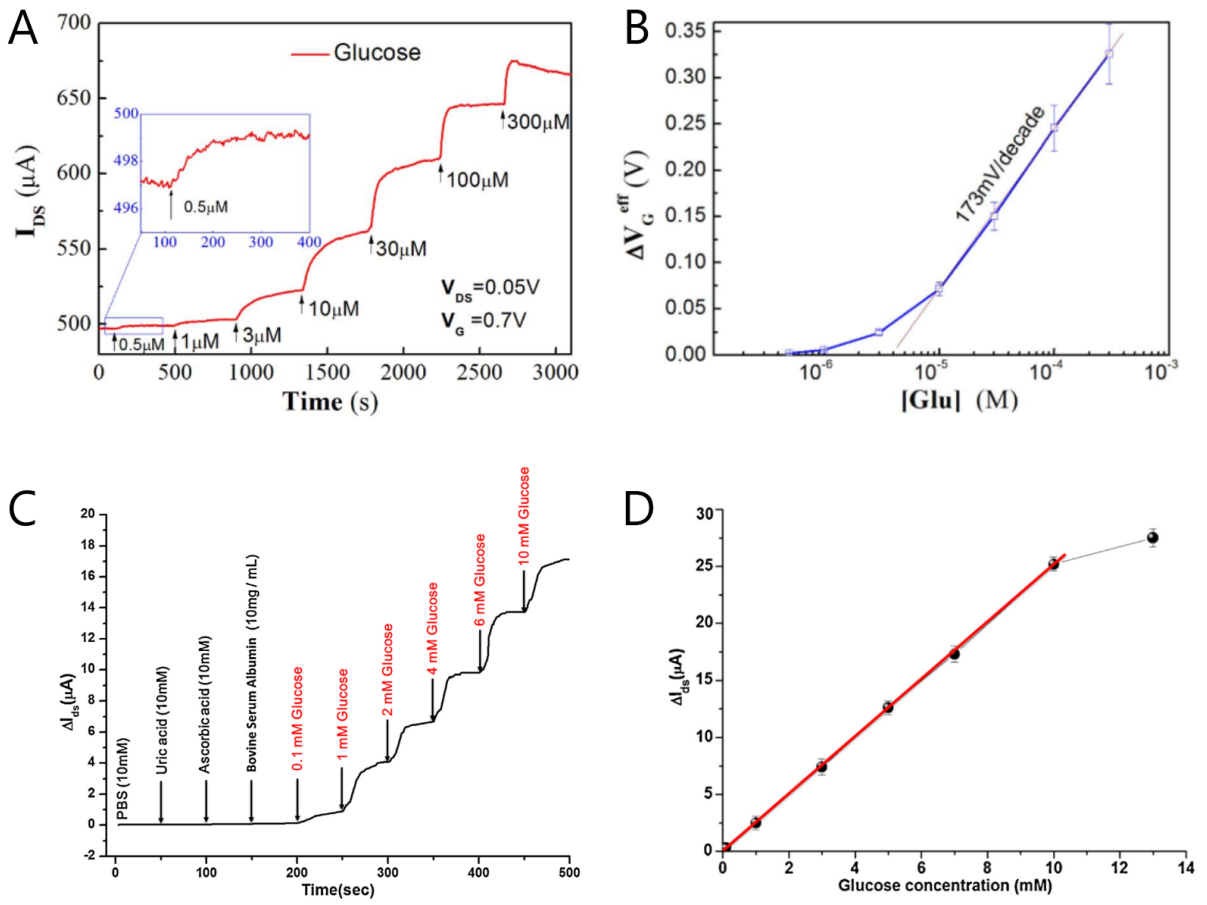

Figure 12. Real time measurements of drain-to-source current as a function of glucose concentration for GOx bound to a polymer matrix A) and GOx bound to a silk film B) based GFETs. C) and D) show the linear correlations of the change in the effective gate potential and the change in drain-to-source current at the Dirac point in the respective order. A) and B) reprinted with permission from reference 45. C) and D) reprinted from reference 49, copyright 2015, with permission from Elsevier.

and covalently bound 3-APBA (c-3-APBA). The non-covalent devices were fabricated separately by immersing the graphene surface in a solution of the functionalizing agent for 12 h. This leads to $\pi - \pi$ stacking of the probe molecules on top of the rGO. The covalent bonds were formed by activating the carboxyl groups of the rGO sheets by immersing them in 1-ethyl-3-(3-dimethylaminopropyl)carbodiimide for for 20 min, followed by a 30 min bath in a N-hydroxysuccinimide bath. This was followed by 12 h incubation with the 3-APBA solution, leading to amide bond between the amino group of the 3-APBA and the carboxyl groups of the rGO. Of these, the non-covalent bonding offers better sensitivity. This is because carboxyl groups are relatively rare on the rGO surface, whereas the graphene offers many more sites for $\pi - \pi$ stacking, leading to a greater APBA concentration, which naturally leads to greater sensitivity. Of the non-covalently bound APBAs, 4-APBA has the superior sensitivity. This is due to the para position of the amino group, which allows for it to interact more actively with the rGO, leading to better binding. The specificity of the device is due to bond forming affinity of the boronic acid, making the sensor 21 and 13 times less sensitive to BSA and lactose respectively than to glucose. The change of normalized gate voltage as a function of glucose concentration for all the devices is presented in figure 13. The inset of the figure shows comparison of the change in normalized gate voltage with some common interfering agents at 0.1 mM, highlighting the specificity of the device.

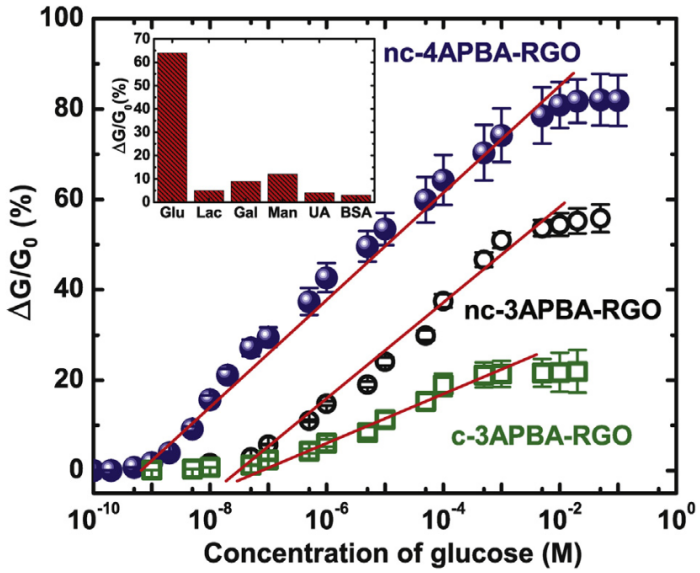

Figure 13. The change in the normalized gate voltage as a function of glucose concentration for different APBA dunctionalized devices, with linear fits. The inset shows the comparison of the change at 0.1 mM concentration for glutamate, lactose, galactose, mannose, uric acid and bovine serum albumin. Reprinted from reference 46, copyright 2015, with permission from Elsevier.

Table 3. Details of covered GFETs for glucose detection

Material	Functionalization	W/L	LDR	Substrate	Year	Ref
Graphene	GOx bound to PBASE	$\sim$2x4 mm$^{2\,(1)}$	0.1 mM$^{(2)}$	Quartz	2010	47
Graphene	GOx bound to PBASE	33 mm$^{2\,(3)}$	3.3 – 10.9 mM	PET	2012	48
Graphene	Gate modified, polymer matrix, GOx, PtNP	0.2x3 mm^2	0.5 – 1000 µM	Glass	2015	45
rGO	nc-3-APBA nc-4-APBA c-3-APBA	$\sim$5 µm x 2 µm	100 nM – 5 mM 1 nM – 10 mM 500 nM – 0.5 mM	SiO_2/Si	2015	46
Graphene	GOx bound to silk, silk gate	-x300 µm	0.1 – 10 mM	SiO_2/Si	2014	49

$^{(1)}$ order of W and L not specified.
$^{(2)}$ indicates LOD in absence of a reported linear detection range.
$^{(3)}$ indicates area in absence of a reported W/L ratio.

4.3 Detection of DNA

As a central molecule to life, the detection of DNA has naturally been studied extensively. DNA usually exists as single strand DNA (ssDNA) and double strand DNA (dsDNA). It is well known that typically DNA strands bond mostly by the complementary base pairings: adenine with thymine and cytosine with guanine. It is thus possible to make GFETs sensitive to certain single strands of DNA, by functionalizing the graphene with the complementary strands of the target. DNA can be bound to graphene by dissolving it to a liquid, and exposing the graphene to the solution for some hours. The binding is dominated by non-electrostatic stacking interaction, that can be considered as n-doping for the graphene. This is due to the negative charge of the DNA inducing charge transfer between the nucleotide and the graphene surface. Binding of the target molecules can be seen as a shift of the Dirac point in the $I_{\mathrm{DS}} - V_{\mathrm{G}}$ graph. The minimum current also decreases, but it can not be used as an indicator of DNA binding. This is because the minimum conductance is very susceptible to changes in ionic concentration. A shift in the Dirac point can also be noticed when a single-pair mutated DNA is measured with the same setup, although this is in much smaller scale, making the different samples identifiable. The shift in Dirac point for both the complementary and mismatched as a function of the analytes is presented in figure 14 B. A setup like this naturally comes with disadvantages. The LGGFET response saturates at a point due to the limited number of complementary strands, and measurements of only two different samples are not much for practical applications, such as cancer detection.

The sensitivity of the device was improved upon by synthesizing gold nanoparicles (AuNP) on

top of the graphene before functionalization with the probe DNA. The thiolated DNA strands are known to bind covalently with the nanoparticles, and their function is to increase the probe DNA concentration on the device. The AuNP assembly was conducted by immersing the graphene devide in 10 mM $HAuCl_4$. The decoration was found to induce p-doping on the graphene during the first 30 min of immersion, but for longer immersion times the doping direction switched to n-type. The shift in Dirac point as a function of immersion time is presented in figure 14 A. Functionalization with the AUNP's increased the upper limit of the linear detection range from 10 nM to 500 nM.[50]

Real time detection using complementary DNA strands has been demonstrated by Stine *et al.*.[3] They utilized two different LGGFETs in a flow channel, one of which was functionalized with complementary strands of the target DNA, and the other with completely non-complementary strands. Both types of strands were aminated at the 3' end to allow for covalent bonding with the rGO surface. A schematic presentation of the setup is presented in figure 15, but unfortunately no dimensional information was provided. The shape of the source and drain electrodes is of some interest, as they form two interlinking F-shapes, instead of the typical straight lines. Another property of interest is the (aminopropyl)trimethoxysilane layer formed between the rGO and silicon layers. Its function is to stabilize the attachment between the two surfaces. The measurement principle was to subtract the non-complementary LGGFETs signal from the complementary one's signal, to remove the effect of common interference between the devices. The group used a lock-in amplifier to measure the differential voltage between the two devices under constant gate voltage. As the technique only provides information on the difference

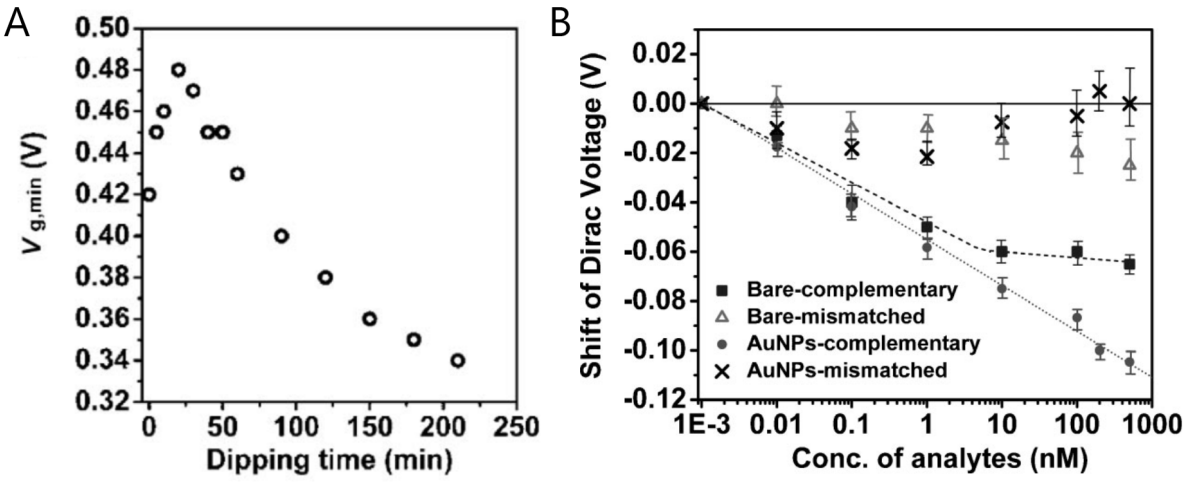

Figure 14. A) the evolution of the position of a LGGFET's Dirac point voltage as a function of immersion time in $HAuCL_4$, and B) the change in Dirac point voltage for a device fabricated with probe DNA molecules attached directly to the graphene or the AuNP's as a function of analyte concentration. Reprinted with permission from reference 50.

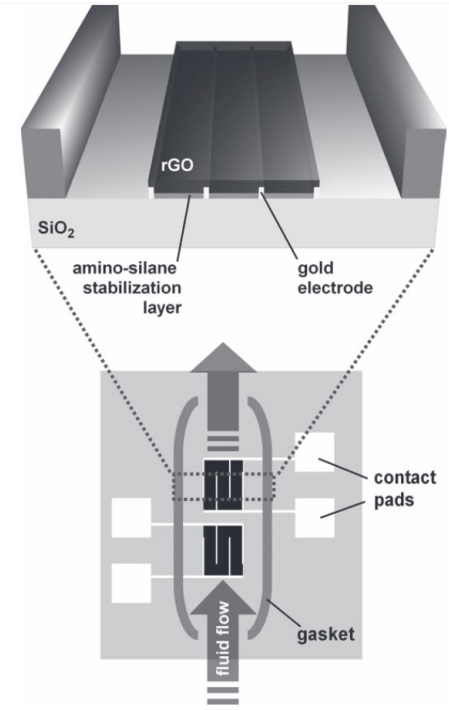

Figure 15. The measurement setup for the real time detection of ssDNA. Reprinted with permission from reference 3.

between the devices, a non-dimensionalized current difference

$$\text{normalized}\,\Delta I = \frac{V_1 - V_2}{R}\left(\frac{2}{I_{0,1} + I_{0,2}}\right)^{-1} \tag{17}$$

was derived. Here, $V_1 - V_2$ is the differential output signal, R the fixed resistance in the bridge circuit, and $I_{0,1}$ and $I_{0,2}$ are the source-to-drain currents of the different devices measured before the experiment. Real time measurement of normalized ΔI and normalized ΔI as a function of target DNA concentration are presented in figure 16.

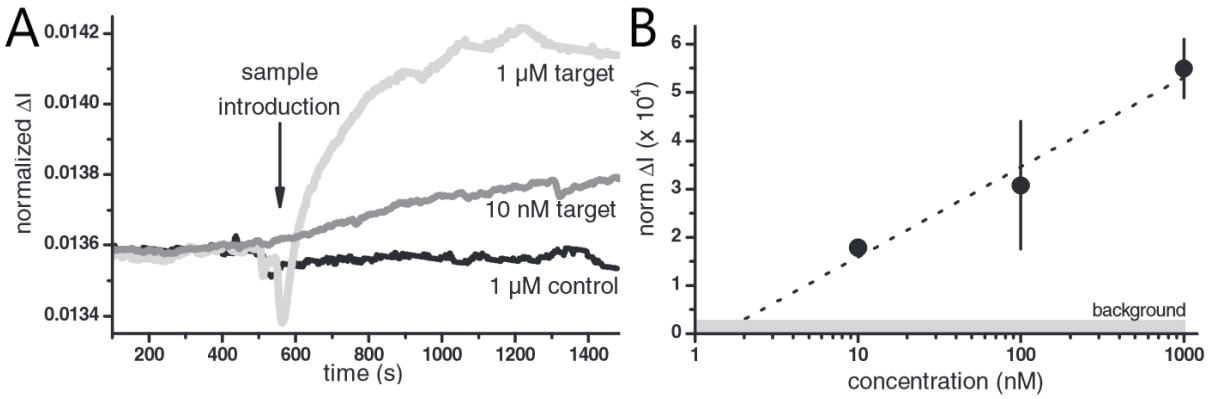

Figure 16. A) The real time measurement of normalized ΔI as a function of concentration, with clear detection of the target DNA, but no detection of the control molecule, and B) the linear correlation between the normalized ΔI and target DNA concentration. Reprinted with permission from reference 3.

Complementary DNA strands can be attached to the graphene surface also by covalently binding them to other molecules that can $\pi - \pi$ stack, such as PBASE. The bound DNA still causes a left-shift in the Dirac point. DNA strands bound covalently to the linkers have proven to be more stabile and to have less non-specific sensing than the directly to the graphene bound ones. Guo *et al.*[41] used a setup such as this to measure the change in device resistance. They noticed that the resistance decreases in the beginning of the measurement, but then starts to increase. This was suggested to be due to some of the probe molecules attaching directly and non-covalently to the graphene surface. Increasing the target DNA concentration made even the non-covalently bound strands to hybridize, breaking the bond to the graphene, making the gating effect smaller and thus increasing the resistance.

The gate electrode naturally also affects the properties of the transistor, and can be used as the sensing part of a LGGFET. On the electrode surface there is an EDL, much like the one on the graphene surface. Coating the gate electrode with complementary DNA strands changes the EDL, and the potential change at the surface of the gate electrode can be expressed as

$$\Delta\psi = \frac{nQ_{\mathrm{DNA}}}{\varepsilon_{\mathrm{r}}\varepsilon_0} t_{\mathrm{DNA}}, \tag{18}$$

where n is the surface density of the DNA molecules, Q_{DNA} the charge of a DNA molecule, ε_{r} the dielectric constant of the DNA layer, ε_0 the dielectric permittivity of air and t_{DNA} the thickness of the DNA layer. Due to the intrinsic negative charge of DNA molecules, their attachment lowers the gate potential. Hybridization with target strands further increases this effect. The channel current for a gate-functionalized device is given similarly to equation (3) by

$$I_{\mathrm{DS}} = \frac{W}{L}\mu C_{\mathrm{i}}(V_{\mathrm{GS}} - V_{\mathrm{offset}} - V_{\mathrm{Dirac}} - \frac{V_{\mathrm{DS}}}{2})V_{\mathrm{DS}}, \tag{19}$$

where V_{offset} is related to the potential drop on the two electrolyte interfaces and C_{i} is the gate capacitance. In a purely gate functionalized system $V_{\mathrm{offset}} = \Delta\psi$. Whether C_{int} should be taken into account is not mentioned upon, nor the possible conjugation of DNA to the graphene surface. Real time measurements of the drain-to-source current at the Dirac point and the change in Dirac point voltage as a function of concentration are presented in figure 17.[51]

Specificity is relatively easy to obtain with short strands of DNA, where a single mismatch pairing creates a critical difference in binding affinity. When the amount of nucleotides exceeds 40, as in most practical applications, a single mismatch is no longer relatively such a huge thing, and cross linking may happen. DNA strand displacement is a method to obtain higher accuracies even in longer chains. In strand displacement, the probe DNA is linked before the measurement with a strand that has lower affinity for the probe than the target strand has. A schematic representation of the mechanism is presented in figure 18 A. The probe may also have a toehold section, i.e. the probe strand is longer than the initially bound strand. This allows for

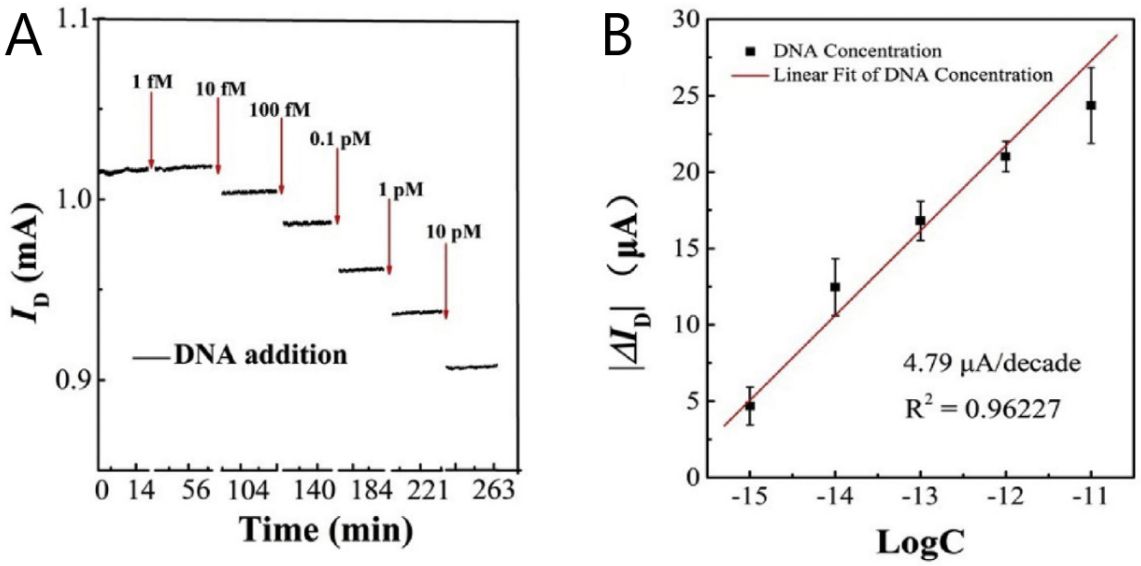

Figure 17. A) shows the real time measurement Dirac point current as a function of DNA concentration at $V_G = 0.8\,V$ and $V_{DS} = 0.1\,V$ and B) the change in Dirac point current as a function of the DNA concentration for the purely gate functionalized device. Reprinted from reference 51, copyright 2019, with permission from Elsevier.

the target strand for initial attachment, to ease the replacement. The length of the toehold and the differences in affinity between the strands both affect the sensitivity of the measurement. The sensitivity of this setup is highlighted when it is compared with a similar transistor, that has only the single probe strand. A device like this is not able to differentiate between perfectly complementary strands and single mismatch strands in 10 pM to 10 μM range.[52]

The electrostatic potential of graphene is affected only by the nucleotides close to the surface. In the double strand setup, this means that a part of the molecules do not have an effect on the graphene properties. The signal response can be increased by having a "molecular tweezer" form for the probe. A molecular tweezer is otherwise the same as the double strand setup mentioned before, except where the double strand ends, molecular tweezer has another branch of double strands. When the target strand replaces the initial strand in the tweezer, the unaltered branch aligns the probe branch closer to the graphene surface. This increases the detected signal, as more nucleotides are within Debye length of the graphene surface. The sensitivity of the tweezer setup increased three orders of magnitude from the double strand measurement, and it was not affected by other DNA molecules in a sample. A schematic representation of the single strand displacement and the nanotweezer are presented in figure 18, as well as the function of the nanotweezer on top of the graphene surface.[42]

Besides complementary DNA strands, the graphene in GFETs can be functionalized also by other biological molecules, like antibodies and aptamers, to detect DNA. These are both organic molecules that can bind selectively to organic or inorganic molecules. The usefulness of aptamers is based on the ease of their production and affinity towards the target molecules, that

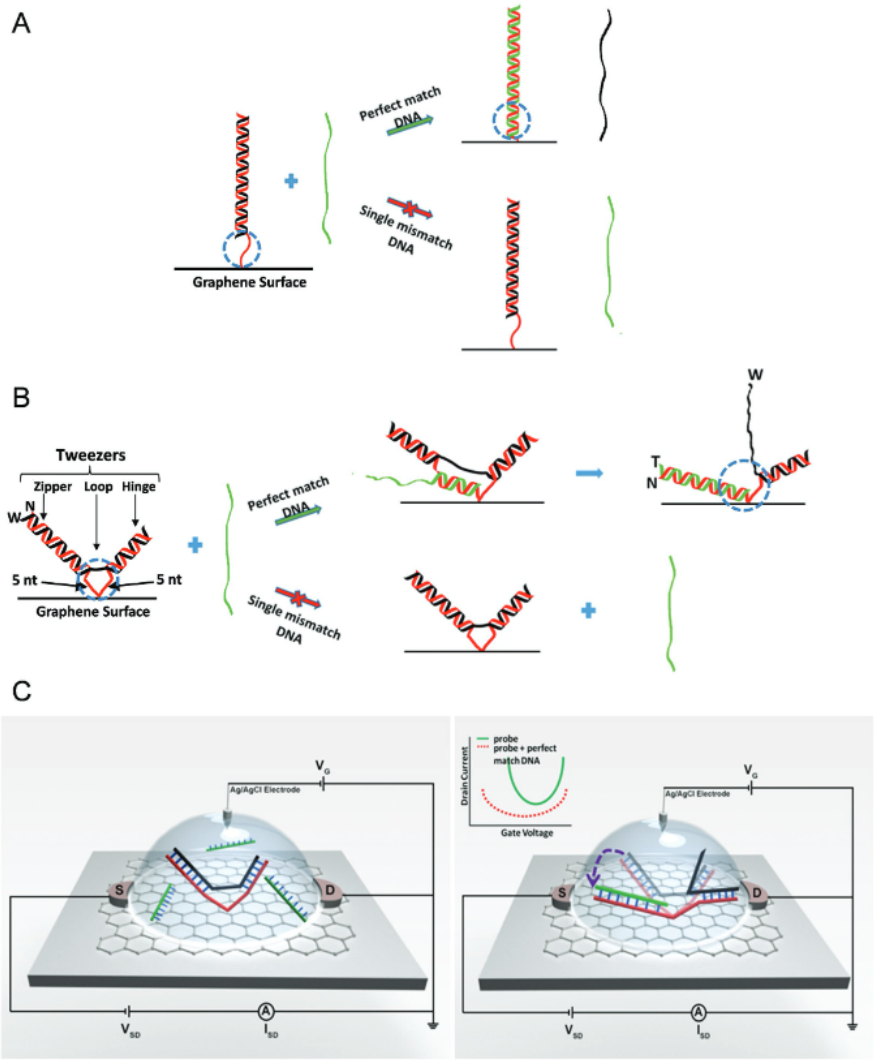

Figure 18. Schematic representations for the function of A) single strand displacement and B) nanotweezer. C) shows how the nanotweezer lies on top of the transistor. The inset in C) shows the clear change in transconductance when the perfect match DNA is introduced to the system. Reprinted with permission from reference 42.

is comparable to antibodies.[53] Aptamers and antibodies can also be used to detect one another. Functionalizing the graphene surface with the aptamers can be done non-covalently by $\pi - \pi$ stacking. LGGFETs formed like this show no notable change in I_{DS} as other biomolecules, such as BSA and streptavidin, are added to the electrolyte solution, but show a clear decrease in I_{DS} when the target molecule is introduced to the system. It is noteworthy that all of the mentioned molecules are detectable by a pristine GFET, indicating good selectivity caused by the aptamer. The adsorption is once again noted to follow the Langmuir adsorption isotherm.[54]

4.4 Detection of biomolecular response

Neurons, and particular muscle cells, generate a type of electric pulse called the action potential (AP). This phenomenon is used in the human body for transporting sensory input from pe-

Table 4. Details of covered GFETs for DNA detection

Material	Functionalization	Dimensions	LOD	Substrate	Year	Ref
Graphene	Complementary strand bound to PBASE	8x80 nm^2	3 nM	Si/SiO_2	2011	41
Graphene	Gate functionalized, thiolated ssDNA	6x0.25 mm^2	1 fM	Glass	2019	51
Graphene	Double strand bound to PBASE	4x6 mm^2	-	SiO_2	2016	52
Graphene	Nanotweezer bound to PBASE	$\sim$2x7 mm^2	-	Si/SiO_2	2018	42
Mono/few layer graphene	ssDNA (+AuNP)	$\sim$3x5 mm^2	0.01 nM	Glass	2010	50
Reduced GO	Aminated ssDNA	-	2 nM	SiO_2	2010	3
Graphene	Aptamer bound to PBASE	-	0.29 nM$^{(1)}$	SiO_2	2010	54

$^{(1)}$ indicates a lowest measured value in absence of a reported LOD.

ripheral nervous system to the central nervous system, contracting and extending muscles, and ultimately to create conciousness.

There are different kinds of neurons, but all of them have four distinct regions: the cell body, the axon, the axon terminals and the dendrites. The structure of a neuron is presented in figure 19. The cell body contains the nucleus and houses the synthesis of all kinds of neuronal proteins and membranes. Some proteins are also fabricated in the dendrites. The axon has a diameter of some micrometers and they are specialized for conduction of action potentials. At the ends of axons there are axon termini, that are used to form synapses between different cells. Dendrites are used to receive chemical signals from axon termini. These signals are converted to electric impulses and transferred towards the cell body. Synapses can also be formed directly to the cell body. The depolarizations received by a cell body spread to the axon hillock, and if they are sufficiently large, an action potential is formed. The formation of AP is an all-or-nothing process: depolarizations lower than the threshold potential form never induce an action potential, whereas depolarizations exceeding it always do.

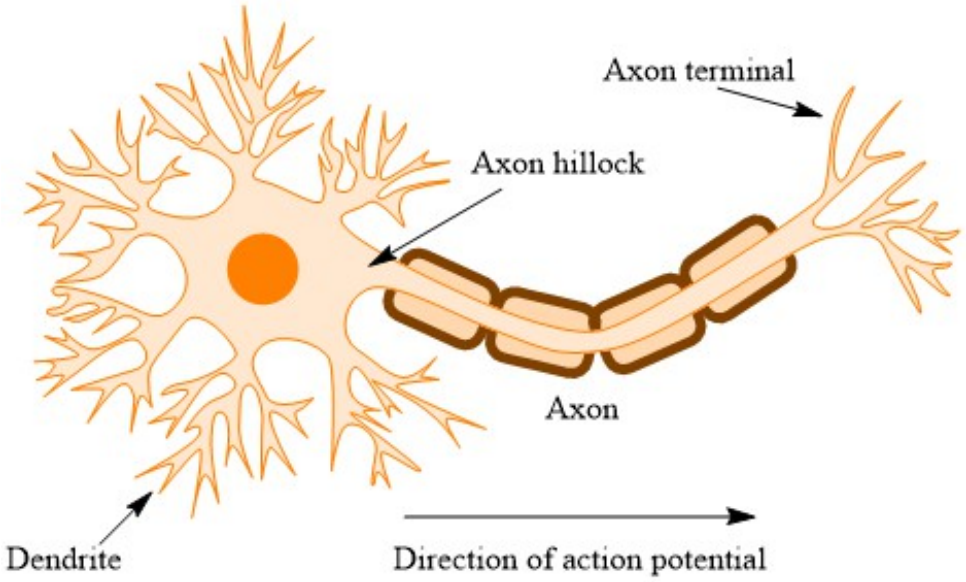

Figure 19. A schematic representation of a neurocell

Action potential is a series of sudden changes in the electric potential across the plasma membrane of an axon. Rest potential is approximately 60 mV lower on the inside of the axon, and during peak action potential it can be up to 50 mV higher than outside of the cell. Depolarization is followed by rapid repolarization, hyperpolarization and returning to resting value. This cycle can happen hundreds of times per second.

AP originates at the axon hillock, the junction of the axon and the cell body. A schematic representation of an axon hillock is presented in figure 20. The AP is actively conducted to the axon terminals and it moves at speeds up to 100 ms^{-1}. Arrival of AP at axon terminal opens voltage sensitive Ca^{2+} channels, rising Ca^{2+} concentration in cytosol. This triggers fusion of small vesicles that contain neurotransmitters with plasma membrane, leading to neurotransmitters being released from the presynaptic cell into the synaptic cleft *via* exocytosis. After about 0.5 ms the neurotransmitters will have diffused across the synaptic cleft to the postsynaptic cell. Binding of the transmitters induces opening and closing of specific channels in the postsynaptic cell, leading to changes in its membrane potential, and potentially a next AP. A single axon can synapse with multiple neurons and induce responses in all of them simultaneously.

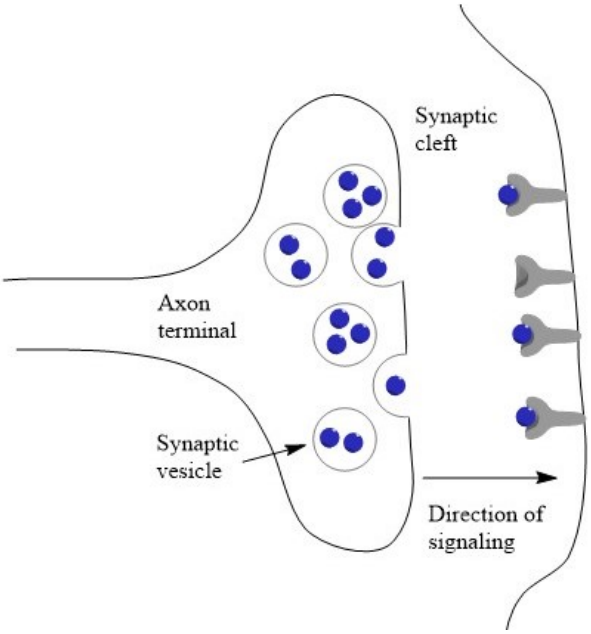

Figure 20. A schematic representation of the synaptic cleft and its immediate surroundings.

Neurotransmitter receptors are divided into two subcategories: ligand-gated ion channels and G protein-coupled receptors. The former open immediately upon neurotransmitter binding, whereas the latter induce the opening of a separate ion channel over a period of time that can last up to minutes. The most typical neurotransmitters are presented in figure 21. Of these, dopamine, epinephrine and norepinephrine form a class of molecules called catecholamines.[55]

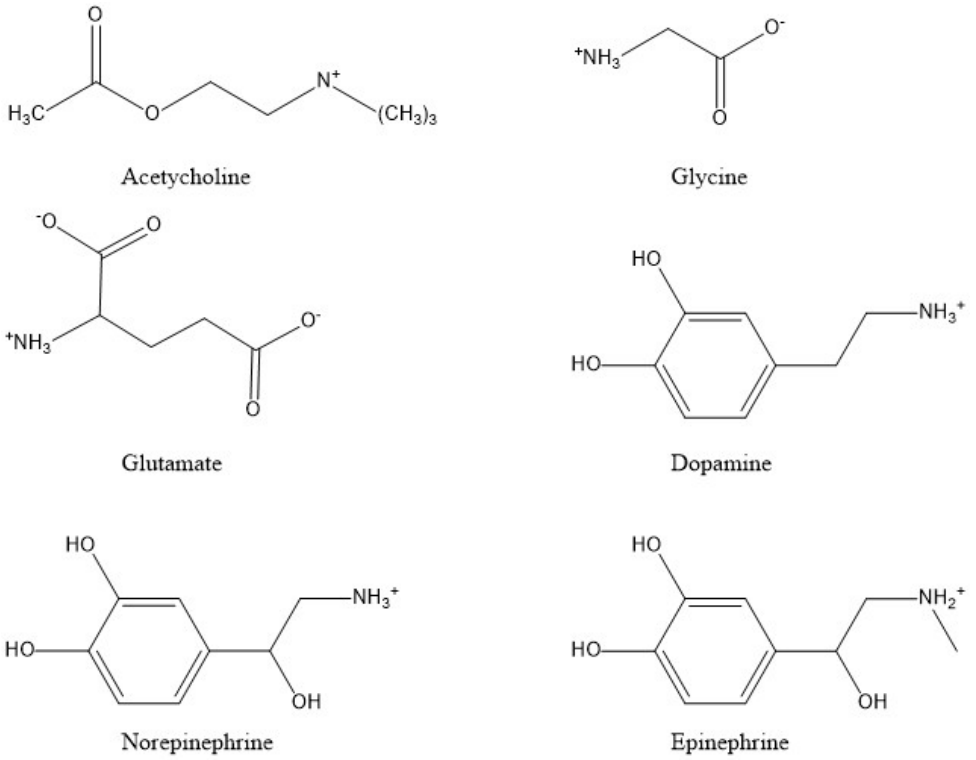

Figure 21. The most typical neurotransmitters.

4.4.1 Detection of acetylcholine

Acetylcholine is an important neurotransmitter present in the autonomous nervous system and the neuromuscular junction. Sohn *et al.*[56] created a device for detecting the molecule by attaching acetylcholinesterase to a network of rGO sheets *via* PBASE. The detection is based on the GFET's ability to detect change in pH by having its active sites react with OH^- and H_3O^+ groups, resulting in change in the density of charge carriers. Acetylcholinesterase is an enzyme which hydrolyzes acetylcholine into acetic acid and choline, resulting in an extra H^+ atom, which consequently shifts the Dirac point of rGO. It was noted that an unfunctionalized rGO device was more sensitive towards change in pH than a functionalized one. This is due to the detection happening on the rGO surface, which is partly obscured in the latter case. Real time measured normalized change in conductance is presented in figure 22 A.

This was improved upon by Hess *et al.*[57] by having acetylcholinesterase attach to a copolymer brush. This polymer consists of two kinds of monomers in equal ratios. The first group is used for hydrolyzing the acetylcholinesterase, and the second one has a dimethylamino group that can take in the proton released by the hydrolyzation reaction, changing the graphene's conducting properties. The measuring principle is illustrated in figure 23. One distinct advantage in using a copolymer brush functionalization over pristine graphene is its adjustable pH sensitivity. For example, the graphene surface is not a reliable pH detector in physiological pH and thus cannot effectively detect the enzyme's activity. Being able to switch the pH sensitive group removes this handicap. Real time measured transistor current as a function of acetylcholine concentration is presented in figure 22 B and change in gate voltage as a function of acetylcholine concentration in figure 22 C.

4.4.2 Detection of glutamate

Glutamate is one of the most common neurotransmitters, playing an important role in the mammalian central nervous system. Glutamate is oxidized according to reaction equation 3 in the presence of glutamic dehydrogenase (GluD) and nicotinamide adenine dinucleotide (NAD). NAD is a cofactor found in living cells and GluD is an enzyme for oxidizing glutamate. This reaction has been utilized for a graphene based glutamate sensor by Huang *et al.*[47] by linking GLuD to the graphene *via* PBASE. The device detects glutamate molecules from a solution by showing an increased conductance and a right shift of Dirac point following the addition of glutamate, but does not respond to other similar molecules. Pristine graphene based sensors were also found to be insensitive to additions of glutamate. The conductance change is due to the ammonium derivative products, analogously to the case of glucose discussed earlier.

$$\text{L-glutamate} + \beta\text{-NAD} + H_2O \longrightarrow \alpha\text{-ketoglutarate} + \beta\text{-NADH} + NH_4^+$$

Reaction equation 3. Oxidation reaction of glutamate.

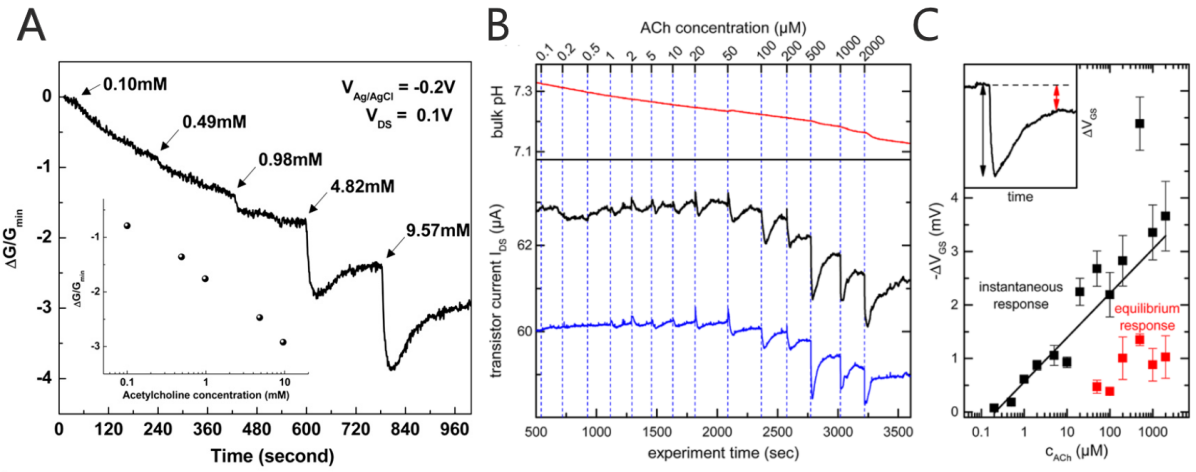

Figure 22. A) shows the real time normalized change in conductance at $V_G = 0\,V$ and $V_{DS} = 0.1\,V$ as a function of acetylcholine concentration, and the inset shows the normalized change in conductance as a function of acetylcholine concentration for the acetylcholinesterase functionalized device. B) shows the real time drain-to-source current of two separate copolymer brush functionalized acetylcholine sensors (black and blue) as a function of acetylcholine concentration, alongside the pH of the solution, and C) shows the instantaneous and equilibrium responses in change of gate potential as a function of acetylcholine concentration averaged for five devices. The inset shows the times at which the instantaneous and equilibrium responses were obtained. A) reprinted from reference 56, copyright 2013, with permission from Elsevier. B) and C) reprinted with permission from reference 57. Copyright 2014 American Chemical Society.

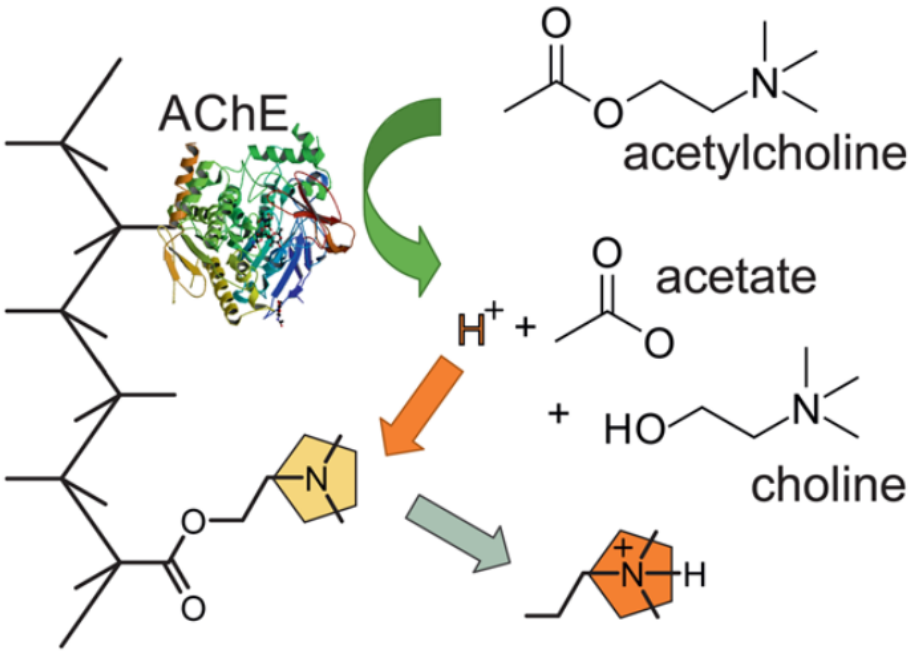

Figure 23. A schematic representation of the principle of measuring the concentration of acetylcholine using a copolymer brush containing acetylholinesterase and dimethylamino groups in equal ratios. Reprinted with permission from reference 57. Copyright 2014 American Chemical Society.

Glutamate has also been detected directly from primary cultured rat hippocampus neurons. Li *et al.*[58] created a rGO based FET that was functionalized by metabotropic glutamate receptors (mGluR), which binds strongly and specifically to glutamate. Binding of mGluR to graphene was accomplished *via* PBASE, and resulted in a negative shift of the Dirac point. Measured characteristics of the device are presented in figure 24. Figure 24 A shows the $I_{DS} - V_G$ characteristic of the GFET at different glutamate concentrations from 0.1 fM to 10 nM and with no glutamate. The detected amounts are outstandingly small, as the detection range is between 1 fM and 100 pM. Larger concentrations show no apparent shift in the Dirac point, most likely due to all available receptors being bound to ligands. To ease the analyzation of the data, it was normalized: defining $\Delta V_{g,\,glu}^{cal}$ as the change in the Dirac point and $\Delta V_{g,\,glu}^{cal,\,max}$ as the maximum change in the Dirac point, and plotting $\Delta V_{g,\,glu}^{cal}\,\Delta V_{g,\,glu}^{cal,\,max\,-1}$ as a function of glutamate's concentration. This way figure 24 B was obtained, and it shows a clear linear dependence of $\Delta V_{g,\,glu}^{cal}\,\Delta V_{g,\,glu}^{cal,\,max\,-1}$ on the concentration of glutamate. The inset in the figure shows a Langmuir adsorption isotherm fit of the data, from which a binding affinity dissociation constant was determined. The extremely small value of 3.86 ± 2.68 pM indicates very strong binding between the ligand and mGluR.

Real time measurements of I_{DS} at 0.1 V as a function of glutamate concentration are presented in figures 24 C and D for measurements in phosphate buffered saline (PBS) solution and cell medium, respectively. Measurement of glutamate secreted by the cells was conducted on cells grown directly on top of the graphene channel. The secretion was induced by providing K^+ ions to the liquid gate. This caused depolarization of the neurons, leading to opening of the Ca^{2+} channels and eventually release of the glutamate. The fits of the measured values show excellent linear correlation between $\Delta I_{DS}\,I_0^{-1}$ and glutamate concentration.

Table 5. Details of covered GFETs for glutamate detection

Material	Functionalization	Dimensions	LOD	Substrate	Year	Reference
Graphene	GluD bound to PBASE	$\sim$2 x 4 mm^2	5 µM	Quartz	2010	47
rGO	mGluR bound to PBASE	-	1 fM	Si/SiO_2	2019	58

4.4.3 Detection of catecholamines

Dopamine is an important neurotransmitter for the central nervous system. Irregularities in dopamine levels are associated with many diseases, such as Parkinson's disease and schizophrenia. Epinephrine and norepinephrine are both an integral part of the fight-or-flight reaction. Catecholamines can $\pi - \pi$ stack on top of graphene due to the aromatic ring they all possess. He *et al.*[59] created a dopamine sensor with few micrometer wide stripes of rGO as the semiconducting channel. The device had an increased p-doping character as a function of increasing

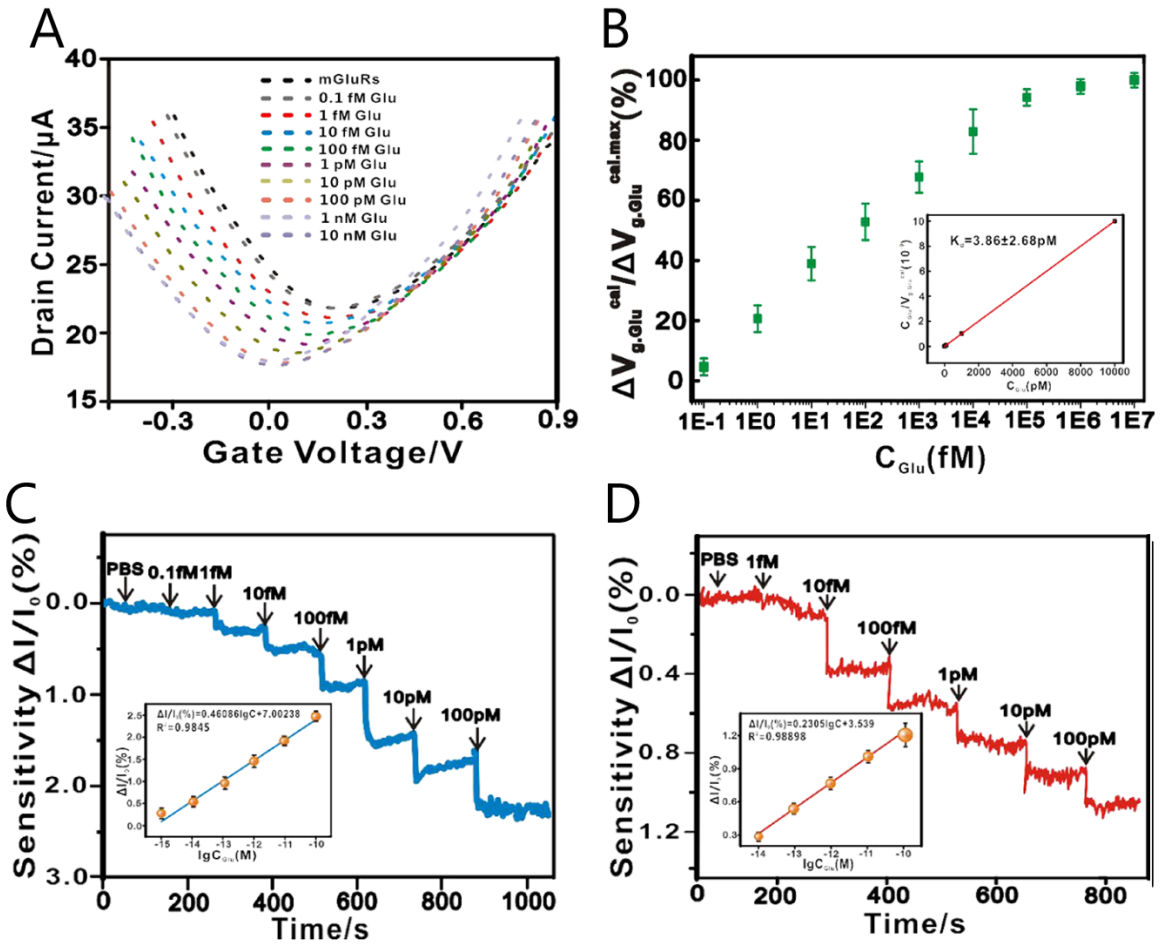

Figure 24. Measured spectra for the mGluR functionalized LGGFET. A) shows the $I_{DS} - V_G$ characteristics at different glutamate concentrations, B) the normalized Dirac point shifts as a function of glutamate concentration, C) and D) the real time measurements of normalized $\Delta I_{DS} I_0^{-1}$ as a function of glutamate concentration in PBS and cell medium, respectively. The inset in B) shows the fit to a Langmuir adsorption isotherm, and the insets in C) and D) the linear fits of $\Delta I_{DS} I_0^{-1}$ as a function of glutamate concentration. Adapted with permission from reference 58. Copyright 2019 American Chemical Society.

catecholamine concentration. This is shown in figures 25 A and B, for devices with quartz and PET substrate, respectively. The device was also used to detect epinephrine, although its sensitivity was smaller towards this molecule. The device was also able to detect secretion of vesicular catecholamines from PC12 cells. Before culturing the cells on top of the transistor, the graphene surface was coated with poly-L-lysine to better adhere the cell and graphene surfaces. Secretion of the catecholamine was induced by introducing a high concentration of potassium to the solution. Real time measurement of dopamine secreted by the cells is presented in figure 25 C.

Jung *et al.*[60] used a classical LGGFET to measure the concentration of dopamine secreted by the same cell line and found similar results. Their measurements of dopamine solution and dopamine secreted by the cells are presented in figures 25 D-E. They were also able to use the device to electrically induce dopamine secretion by the cells.

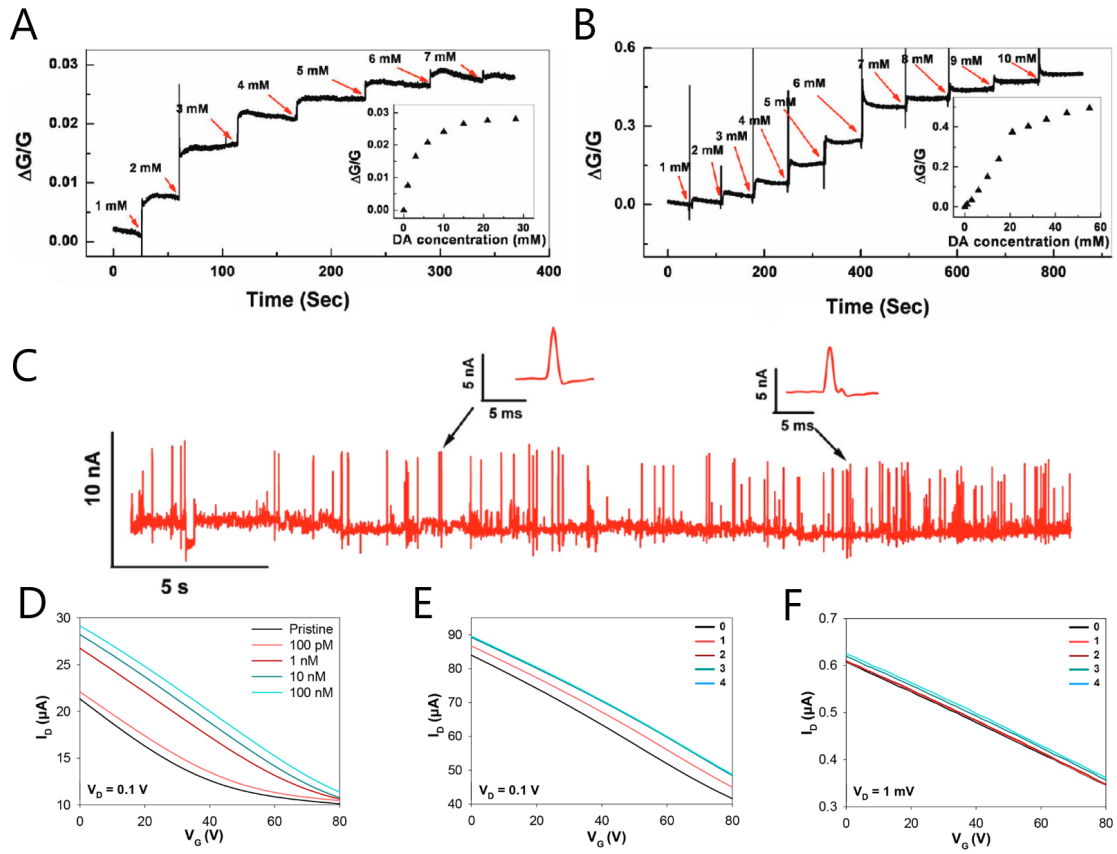

Figure 25. Real time measurement of dopamine concentration in solution using a transistor based on strips of rGO on a A) quartz and B) PET substrate. Insets show the dependance of normalized conductance as a function of dopamine concentration. C) shows the real time measurements of device current as a function of concentration of catecholamines secreted by PC12 cells at $V_{DS} = 100\,\text{mV}$ and $V_G = 0\,\text{V}$. D), E) and F) show the pristine graphene transistor's electrical response to dopamine in solution, dopamine secreted by cells due to electrical stimulation and dopamine secreted due to chemical stimulation, respectively. The numbers in E) and F) signify the times electrical or chemical stimulation was applied. A), B) and C) Reprinted with permission from reference 59. Copyright 2010 American Chemical Society. D), E) and F adapted with permission from reference 60. Copyright 2019 American Chemical Society.

Detection of dopamine was improved upon by Zhang *et al.*[61] who created a device that had graphene as both the semiconducting channel and as the functionalizing agent at the gate electrode. They stated that the responsitivity of the device was due to dopamine electro-oxidizing into o-dopaminequinone at the gate electrode. A schematic representation of the sensing mechanism is presented in figure 26. To verify this, they fabricated an otherwise similar device with an Ag/AgCl electrode and found that it only had a minor response to the catecholamine. The device's effective gate voltage was approximated, similarly as in equation 16, as

$$V_G^{\text{eff}} \approx 2.30(1+\gamma)\frac{kT}{ne}\log C_{DA} + C, \tag{20}$$

where C_{DA} is the dopamine concentration and n the number of electrons transferred during the reaction. This relationship can be used to concentrations higher than $0.1\,\mu\text{M}$. The relationship

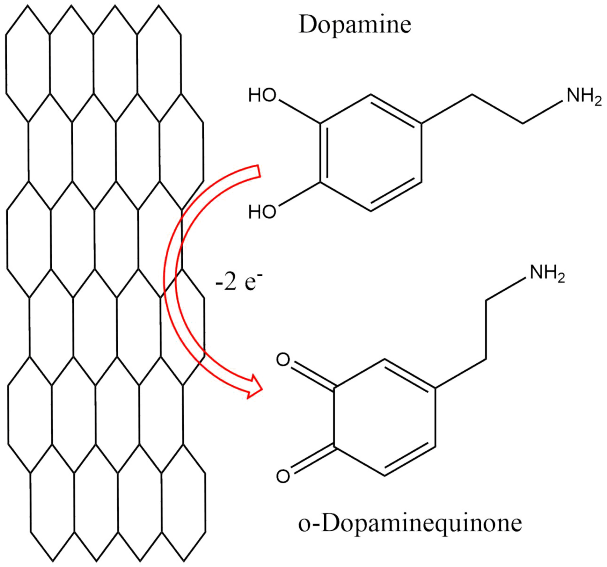

Figure 26. The oxidation of dopamine into o-dopaminequinone at a graphene surface.

between dopamine concentration and effective gate voltage can also be fitted according to power function

$$\Delta V_{\mathrm{G}}^{\mathrm{eff}} = A C_{\mathrm{DA}}^{\alpha}, \tag{21}$$

where A and α are constants. Real time measurements of dopamine concentration are presented in figure 27 A and the change in effective gate voltage as a function of dopamine and common interferents (ascorbic and uric acid) concentration in figure 27 B. In the latter figure, fits according to equations (20) and (21) are also provided.

The sensitivity of the device towards the interferents was respectively one and two orders of magnitude lower than to dopamine. The selectivity was further improved by coating the gate electrode with biocompatible polymer Nafion. Nafion is negatively charged in the pH of the measurement and thus it repels the acids by electrostatic interactions. The selectivity increased so that the sensitivity towards ascorbic acid was three, and the sensitivity towards uric acid four orders of magnitude lower than towards dopamine. Similar measurements and fits as earlier for the Nafion coated device are presented in figures 27 C and D. Unfortunately the device's sensitivity to other catecholamines was not studied.

Oh *et al.*[62] created a GFET for detecting dopamine by functionalizing pristine graphene with flakes of rGO that had been embedded with platinum nanoparticles. The nanoparticles were adsorbed onto the functional sites of the rGO by electrostatic interactions, and the rGO sheets onto the pristine graphene *via* typical $\pi - \pi$ stacking. The purpose of the nanoparticles was to catalyze the oxidization of dopamine into o-dopaminequinone on the surface of graphene. The catalyzation is more efficient if there are more nanoparticles, or if the particles are larger. Both of these are due to the increasing probability of dopamine meeting the catalyst. Real time measurements of change in normalized drain-to-source current as a function of dopamine and

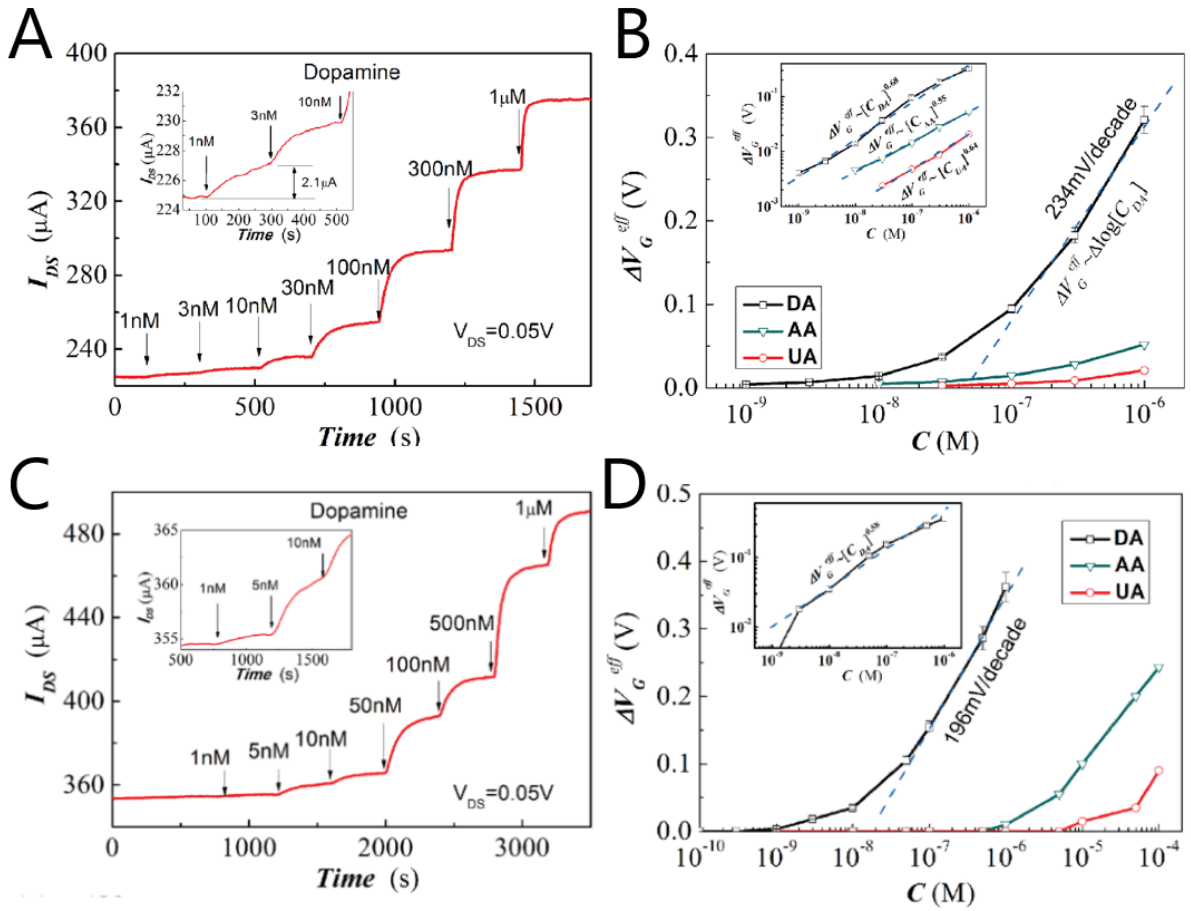

Figure 27. Real time measurements of dopamine concentration using a LGGFET with a A) graphene and C) Nafion coated graphene gates. B) and D) show the change in effective gate voltage as a function of dopamine (DA), ascorbic acid (AA) and uric acid (UA) concentration for the devices in the respective order. B) and C) also include fits to the data according to equations 20 and 21. Reprinted with permission from reference 61.

interferrent concentrations are presented in figure 28.

This device's selectivity was compared against other catecholamines, uric and ascorbic acid as well as tyrosine and phenethylamine. The acids were again noted to not cause any notable signal, due to the absence of a phenyl group. Tyrosine and phenethylamine also had no significant signal, due to the absence of a catechol group to catalytically oxidize. The other catecholamines displayed some sensitivity, but their larger dimensions diminished the catalytic activity and $\pi - \pi$ stacking. It was also displayed that the presence of these molecules did not diminish the detection of dopamine.

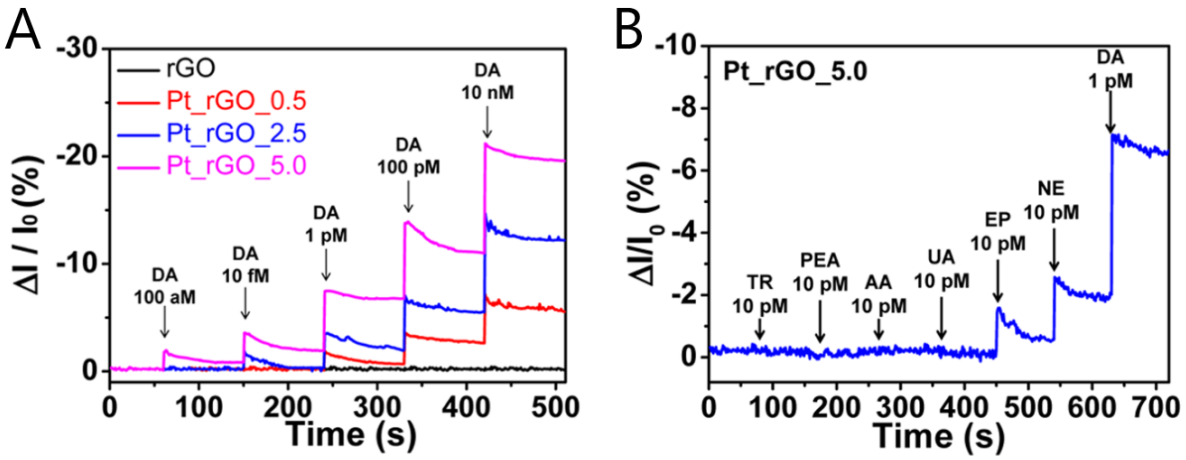

Figure 28. A) Real time measurement of dopamine concentration using a LGGFET functionalized with rGO platelets and different sized platinum nanoparticles, and B) measurements of the effect of six different interferents (tyrosine (TR), phenethylamine (PEA), uric acid (UA), ascorbic acid (AA), norepinephrine (NE), and epinephrine (EP)). Both measurements were conducted at $V_G = 1\,V$ and $V_{DS} = 10\,mV$. Aadapted with permission from reference 62. Copyright 2017 American Chemical Society.

Table 6. Details of covered FETs for catecholamine detection. Limits of detection are reported for dopamine, for which all of the devices were the most sensitive towards

Material	Functionalization	W/L	LOD	Substrate	Year	Ref
rGO	Strips of rGO	10 µm x 1.5 cm[(1)]	1 mM[(2)]	SiO_2, quartz, PET	2010	59
Graphene	None	6 x 6 mm^2	100 pM[(2)]	SiO_2/Si	2019	60
Graphene	None, graphene gate electrode	3 x 3 mm^2	1 nM	Glass/PET	2013	61
Graphene	Pt nanoparticle embedded rGO platelets	2 x 2 cm^2	0.1 fM	PET	2017	62

[(1)] Size of a strip, their number on a single device was not reported.
[(2)] Lowest measured value in absence of a reported LOD.

4.5 FET detection array

Measurements of cells are typically done using arrays of transistors, allowing for spatial resolution besides temporal. Depending on the purpose of the measurement, an array typically contains between 16 and 64 transistors that are placed on a common chip. The transistors can have a common drain electrode and separate sources, or they can be formed of completely individual pairs of electrodes. How the device is wired is not important as long as the transistors can all be measured individually and simultaneously.[2]

As the array is submerged into the electrolyte, the chip should be properly passivated to prevent shorting the circuit. The classical approach is to passivate the whole circuit outside of the

openings for the graphene. This is a good approach for cells like HL-1 that can cover the complete circuit by forming a confluent layer that provides good insulation, and thus increasing the measured signal. Neuronal networks do not form layers like this, and sizes of neurites can be as small as 1 µm, considerably smaller than available transistors. As the graphene must be at least the insulator's thickness deep in the chip, significant bending stress is caused to the delicate cells. To help alleviate this, the insulation can be conducted using a feedline follower model, where only the metallic feedlines are passivated. This also allows for better coupling between the transistor and the cell as the distance between them is lowered. Schematics of arrays of both passivations are presented in figure 29.[25]

4.6 Detection of electrogenic cells

The first measurement of extracellular activity using GFETs was published by Lieber *et al.*.[63] They measured electrical signals from a spontaneously beating cardiac muscle cells of embryonic chicken. The used device was a sheet of graphene suspended between the source and drain electrodes on a SiO_2 substrate. The source and drain electrodes were passivated by SiO_2 followed by covering of the whole device by poly(methyl methacrylate), after which a 50 x 50 μm^2 window was cut to reveal the graphene. Cultured cells were placed on the FET on top of polydimethylsiloxane (PDMS) sheets after which they were submerged in an aqueous medium the gate electrode was placed in contact with.

The achieved signal-to-noise ratio in measurements of conductance against time were regularly over four. They also found that the device sensitivity, as indicated by the peak value of conductance, could be affected by a factor of six by varying the gate voltage. The measured signal was biphasic. The phase flips at the location of the Dirac point, where the change of conductivity from p- to n-branch happens. This is also naturally the point of lowest conductance. It was also found that the device area affected the signals, indicating that the device does not record just the signal of a point, but rather an average of signals across the interface. Measured real time

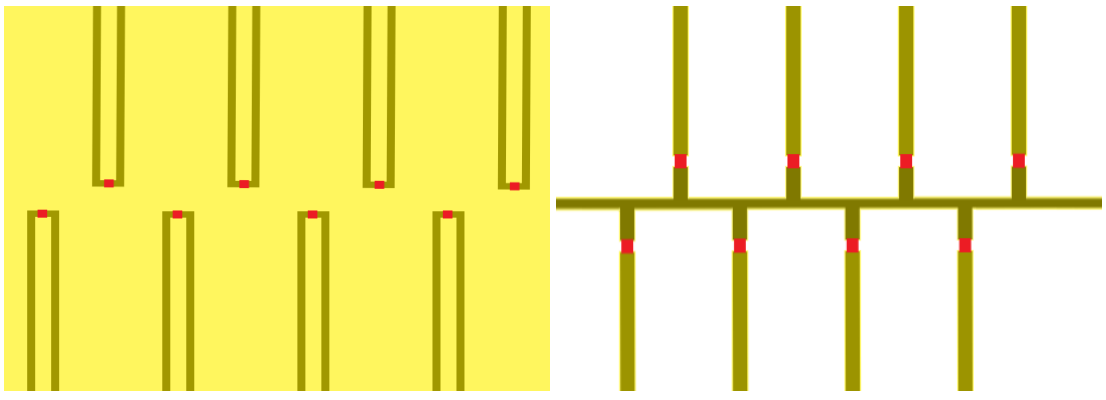

(a) Passivation of whole array. (b) Feedline follower.

Figure 29. Two types of array passivation. Red represents graphene, yellow the passivation. (a) is a set of individual pairs, whereas (b) has a common drain electrode.

conductances at several gate potentials are presented in figure 30.

Soon after, Hess *et al.*[64] demonstrated the use of an array of 16 graphene LGFETs to measure the AP of HL-1 cells cultivated on the array. Using the array, the group was able to track the propagation of the AP across the cell layer. Concurrent measurements of AP using the array are presented in figure 31. It was noted that the shape of the AP varied between different transistors in the array, and even uniphasic signals were recorded alongside biphasic ones. This is due to the signal being dependent on the amount of cells measured at a time and the coupling between the cells and the graphene surface. The former changes due to differing sizes and positions of the cells, and the latter due to the adhesion at the interface. The signal was verified to originate from the cells by addition of norepinephrine to the aqueous medium, which clearly increased the beating frequency. By averaging five successive spikes, a SNR of 70 was achievable.

Kireev *et al.*[25] showed that also neuronal networks can be monitored with a similar setup by growing the cells on top of the transistor. The signals perceived this way are naturally considerably smaller than those recorded from muscle cells. Bursting activity was also measured for the first time using a GFET. The effect of coupling between the cells and the graphene is especially worth underlining here, due to the small size of the neurons in comparison with the active graphene area. The group also measured the APs of HL-1 cells and embryonic heart tissue, and the real time measurements of all three cell cultures are presented in figure 32

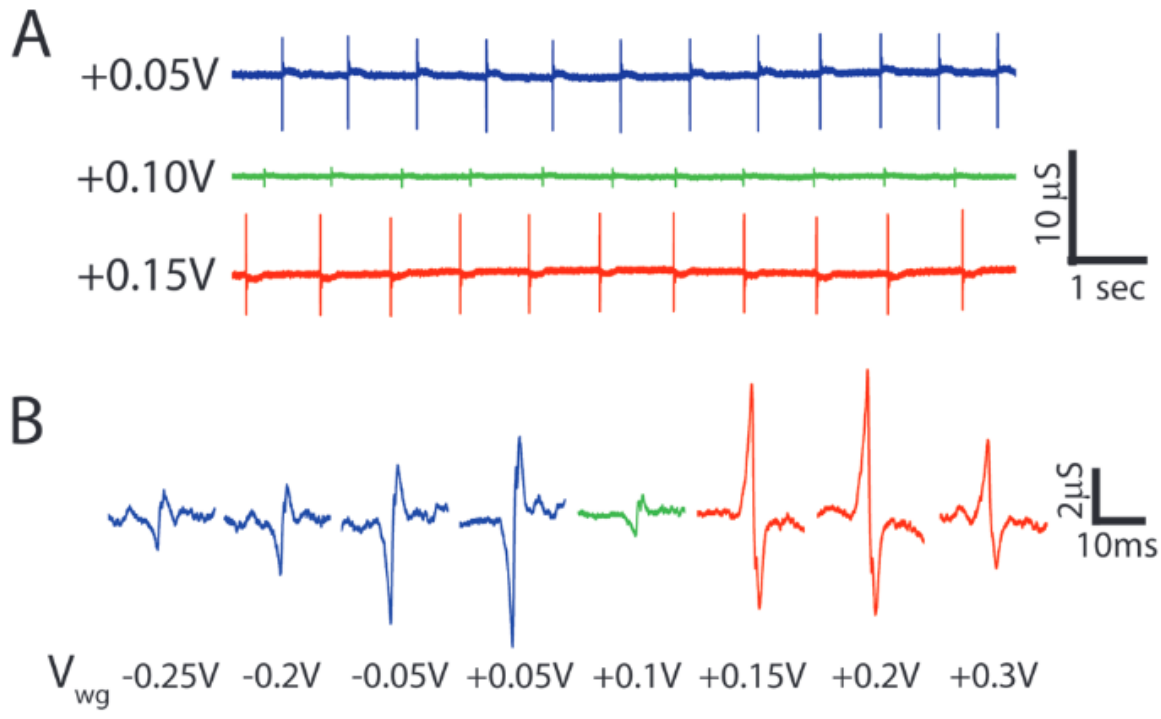

Figure 30. A) Real time measurements of a LGGFET conductances affected by spontaneously beating cardiomyocytes at several gate potentials and B) expanded representative peaks. Reprinted with permission from reference 63. Copyright 2010 American Chemical Society.

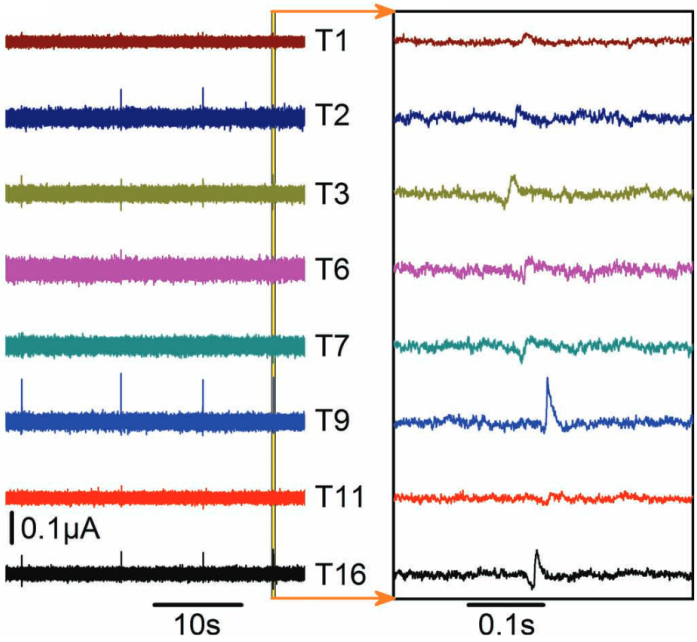

Figure 31. Same time measurement of spontaneously beating cells' APs at different transistors of the same array, and a zoom-in of the data that shows the spatial progression of the AP. Reprinted with permission from reference 64.

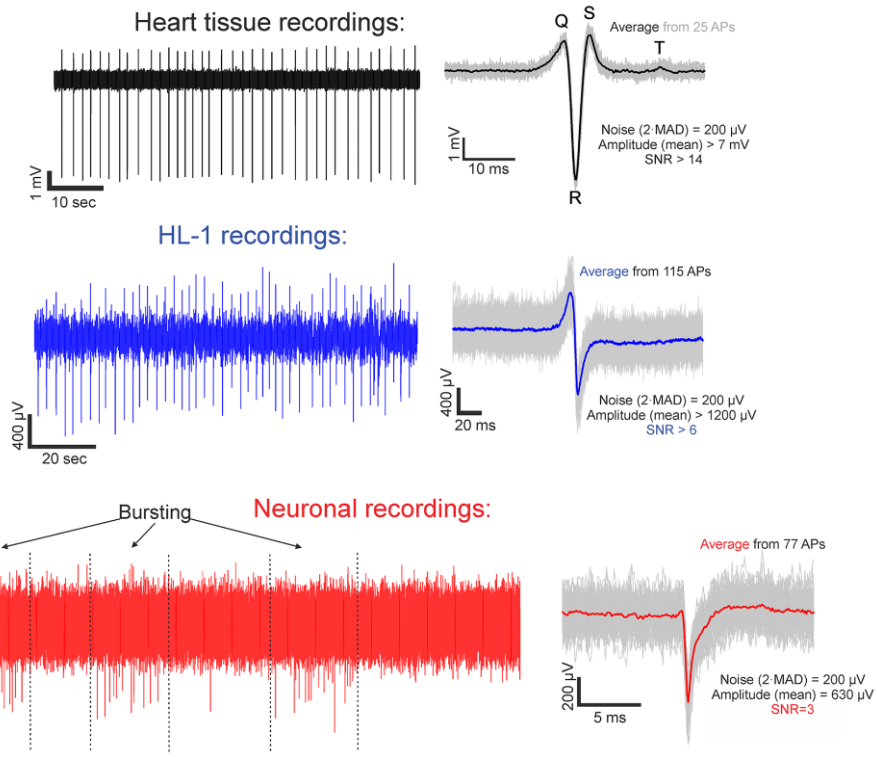

Figure 32. Real time measurements of AP on different kinds of electrogenic cells and averaged signals showing the shape of the AP. Reprinted with permission from reference 25.

Cheng *et al.*[65] studied the effect of suspending graphene on AP measurements. They measured the AP of a rat's heart tissue placed on top of a silicon based LGGFET, after which the tissue was temporarily removed while the silicon was chemically etched off using buffered HF solution. Placing the heart tissue approximately in the same location on the graphene surface yielded current signal amplitude that was three times larger than the original, while device noise decreased by half. Real time measurements of the devices drain-to-source current as the muscle is beating are presented in figure 33. The better signal is caused by three factors. First, etching of the silicon removes the effect of extrinsic charge impurities caused by the silicon-graphene interface. These impurities are known to cause Coulomb scattering in the graphene, resulting in a lower transconductance. Second, the graphene is protruding out of the chip surface. This leads to tighter binding between the cell and the graphene, which in turn leads to a greater signal amplitude. Lastly, as the lowest detectable signal correlates directly with the amount of noise in the system, the etching's lowering of normalized current noise power by 5-10 fold distinctly increases device performance.

Hess *et al.*[66] studied the mechanics of sensing electrogenic cells by LGGFETs. The examined culture compromised of human embryonic kidney cells that were modified with Shaker B Delta6–46 T449V, to induce K^+ channels to the cells. Besides the usual gate electrode, the measurement was complemented with a patch-clamp pipette, that allows the simultaneous measurement on intracellular potential and the ion currents across the cell membrane. The transistor itself is used to monitor the cleft potential. A circuit diagram of the setup is presented in figure 34. The cell membrane is considered a Hodgkin-Huxley equivalent element and the transistor is described as point-like. The contact between the Hodgkin-Huxley element and the electrolyte can be simply modeled as a resistor with a single conductance and this is highlighted

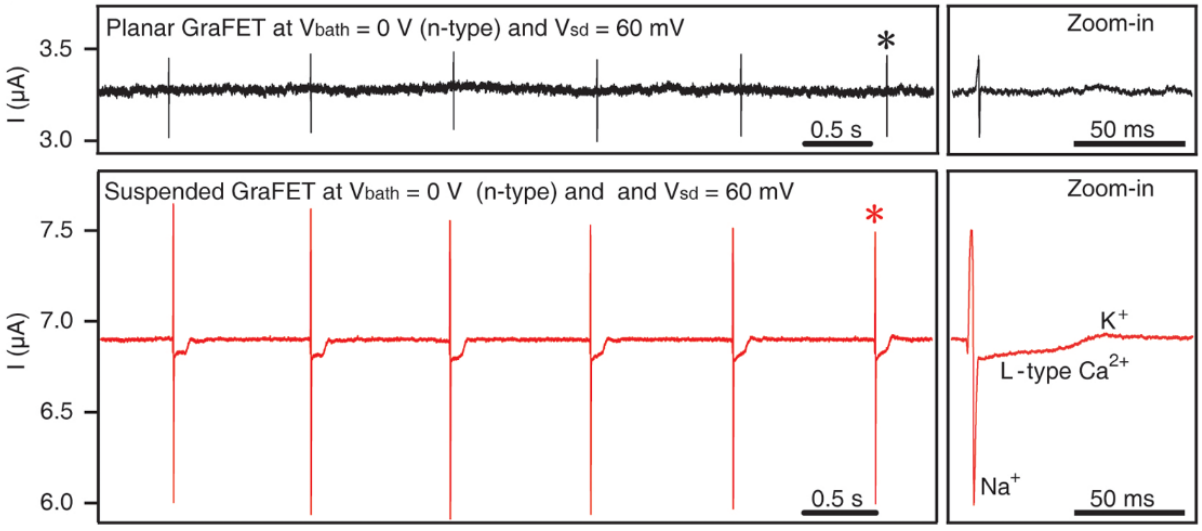

Figure 33. Real time measurements of a beating rat's heart muscle using a silicon based LGGFET and a suspended one. Reprinted with permission from reference 65. Copyright 2013 American Chemical Society.

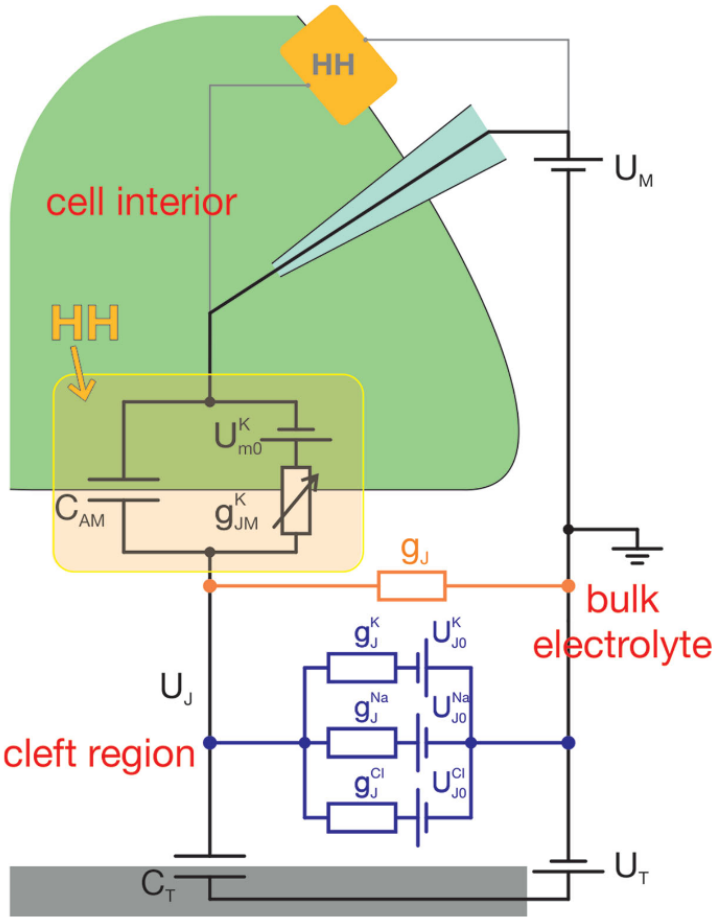

Figure 34. A circuit diagram of a cell and graphene surface interface in a patch-clamp measurement. HH highlights the Hodgkin-Huxley element, C_{AM} denotes the capacitance of the attached membrane, $g^{\mathrm{K}}_{\mathrm{JM}}$ the K^+ channel's voltage dependent conductance, $U^{\mathrm{K}}_{\mathrm{m0}}$ the Nernst potential; C_{T} the point-like capacitance of the transistor, U_{M}, U_{J} and U_{T} the potentials inside the cell, in the cleft and in the transistor; g_{J} and U_{J} the cleft conductance and voltage; $g^{\mathrm{i}}_{\mathrm{J}}$ and $U^{\mathrm{i}}_{\mathrm{J0}}$ (where i = K, Na, Cl) the cleft conductances and potentials dependent on the different ions. Reprinted with permission from reference 66.

with orange in the figure.

This model is not perfect for modeling the cleft potential due to the K^+ ions flowing to the cleft. As the cleft is very narrow, the ions momentarily accumulate in it and induce a positive charge before en equilibrium with the bulk electrolyte is achieved. This potential difference causes and electric force. For this end, Na^+ ions are depleted from the cleft, and Cl^- ions are pulled in. This is shown as blue in figure 34. Effective change in the cleft potential with different depolarization potentials and fits with the point contact model and the model accounting for the ion flow are shown in figure 35.

A DC measurement consists of applying a holding voltage of $-60\,\mathrm{mV}$ to the cell to ensure all the K^+ channels are closed. To remove capacitive effects from the measurement, the measurement pulses were preceded by four pulses with quarter their amplitude, and these were subtracted from the actual measurement. The ion channels were then opened by 10 ms pulses

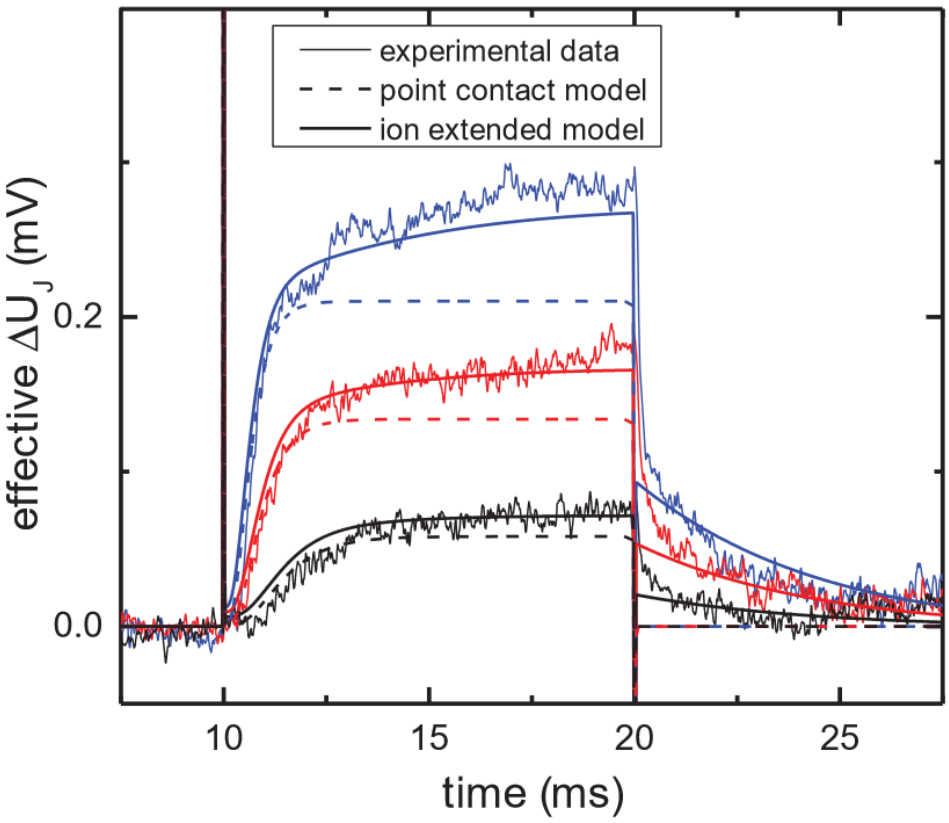

Figure 35. The effective change in cleft potential at 40 mV (black), 60 mV (red) and 80 mV (blue) pulses and fits. Reprinted with permission from reference 66.

with amplitudes of 40 mV, 60 mV or 80 mV with regard to the holding voltage.

4.7 Effect of substrate

The FET technology has its roots in silicon methods, but there are other options. An important property introduced to a GFET by the substrate is bendability. Silicon based transistors are extremely rigid and hence poorly suited for *in vivo* devices. Other proposed substrate materials have been PET,[44,48,59] poly(ethylene naphthalene) (PEN),[11,62] PI,[25,36,67] and silk film.[49] Unfortunately, despite its great promise, no actual bending tests were reported for the silken device. The bending properties of a device do not appear to be related to the type of graphene used, i.e. graphene and rGO both have similar properties.

A dopamine sensor with a PET substrate was deemed to have no particular effect on measuring due to bending.[59] A glucose sensor with the same substrate on the other hand was actually found to have better performance in detection during bending. This was deemed to be due to a larger effective surface area. The same device was also found to have a slightly shifting dirac point as the device was bent.[48] The last PET based device had its resistance changed as a function of bending radius. This effect was found to be reversible, and the device was noted to be extremely durable with regard to bending.[44] The PEN devices were found to have similarly good response to bending, as detection performance dropped by less than 5 % after twenty[11] and a thousand[62]

bending cycles.

Polyimide was chosen because it is a flexible and biocompatible polymer with many biological applications. It is also easy to pattern from photosensitive PI.[36] The first PI device was noted to have excellent durability with regards to bending, having its performance vary less than 5 % after 500 bending cycles. A PIonS device on the other hand had an array of transistors, and a part of the GFETs oriented along the bending axis did not survive 300 to 1000 bends. All GFETs oriented perpendicular to the bending axis did survive, and none showed any meaningful reduction in performance. The destruction on a part of the GFETs was suspected to be due to failing contacts, implying an easily fixable problem instead of a fundamental one.

Of the presented devices, polyimide appears to consistently have the best normalized transconductance, especially among devices reported in the same study. The high transconductance value of the diamond device is of some suspicion, due to the uncertain nature of its length. Another quality that is unaccounted for is the ionic strengths of the measurements, making direct comparisons between different papers approximate at best.[25]

Table 7. The most important parameters of discussed GFETS. Only single transconductance and square normalized transconductance values are provided where the quantities were not specified for both.

Substrate	W/L	$\lvert g_m \rvert$	$\lvert g_m \rvert \,\square\, V_{\mathrm{DS}}^{-1}$	Year	Reference
SiC	40 µmx10/20 µm[1]	1.14 mS V^{-1}	285/570 µS V^{-1}	2011	31
SiO_2[2]	-	-	1.60 mS V^{-1}	2017	25
Diamond	40 µmx10/20 µm[1]	4.23 mS V^{-1}	1.06/2.2 mS V^{-1}	2011	31
Si/SiO_2	20 µmx3 µm	4.2 mS V^{-1}	630±580 µS V^{-1}	2016	67
PIonS	20 µmx3 µm	12.7 mS V^{-1}	1.9±0.9 mS V^{-1}	2016	67
PI	60 µmx40 µm	2.57 mS V^{-1}	1.71 mS V^{-1}	2014	36
PI[2]	-	-	1.34 mS V^{-1}	2017	25
Sapphire	20 µmx3 µm	2.4 mS V^{-1}	360±180 µS V^{-1}	2016	67
HfO_2[2]	-	-	1.43 mS V^{-1}	2017	25

[1]Two differing channel lengths were provided in the text with only a single transconductance value. Square normalized transconductances are calculated for both cases in the respective order.

[2]Transistors fabricated with multiple W/L ratios had their maximum normalized transconductance values averaged.

5 Applications of graphene based devices in neurobiology

The most typical method for neurobiological measurements is using MEAs. These however have a couple of major drawbacks. Their impedance and levels of noise are both inversely proportional to their size, leading to inevitable compromises between spatial resolution and SNR. Their high impedance also limits on-chip multiplexing. Lastly, the measured signal amplitudes in neurobiology are very small and often require preamplification, which considerably complicates device fabrication. All of these problems can be solved by using GFETs that have low impedance, sensitivity that is only dependent on the W/L ratio and high transconductance, all the while being highly flexible, biocompatible and stabile in biological matrices.[68]

Blaschke *et al.*[69] used an array of 16 GFETs to map the brain activity of the visual cortex of a rat. The subjects were anesthetized during all operations. Craniotomy was performed on the rats to access the primary visual cortex of the left hemisphere, and the GFET array was subsequently placed on top of the cortex. Three kinds of signals were induced and measured. First the brain had directly applied bicuculline to it, resulting in pre-epileptic activity. Smaller signals were induced by illuminating the rat's right eye with a LED for 100 ms every few seconds. Slow oscillations typical to slow-wave sleep and deep anesthesia were also measured. For comparison, the measurements were made concurrently with a typically used platinum microelectrode array with 8 and 24 channels for electrodes with 10 µm and 50 µm active measurement area diameters, respectively. The measurements are presented in figures 36 A-C. Average SNRs were 62 ± 5.5; 53 ± 11 and 26 ± 5.5 in the pre-epileptic measurement and 9.85 ± 0.67; 6.02 ± 0.68 and 8.33 ± 1.05 for the spontaneous oscillations for the graphene transistor, smaller electrode and larger electrode respectively. The local nature of the signals induced by light stimulation rendered meaningful SNR comparisons obsolete. These measurements show that graphene based LGFETs are able to compete with existing MEA technology, while offering significant advantages.

Hébert *et al.* used a similar measurement setup to measure synchronous activity, visually evoked and auditorily evoked responses from rat's brain. These measurements are presented in figures 36 D and E. They used a custom made circuit setup to handle the signals. The circuit diagram is presented in figure 37. The low and band pass filters are used to separate the AC ($frequency < 0.1$ Hz) and DC (0.1 Hz $< frequency < 5$ kHz) parts of the signal. This setup allows the transformation of voltage signals into current signals, and for separate amplification of the different signals.

The spontaneous synchronous activity was successfully measured by 11 transistors and $3 - 4$ Hz oscillations were found. The activity was measured from the motor and somatosensory cortical areas. Visual evoked potentials were measured from the contralateral visual cortex after illumination of the right eye with 100 ms pulses from a LED. The auditory-evoked potentials were

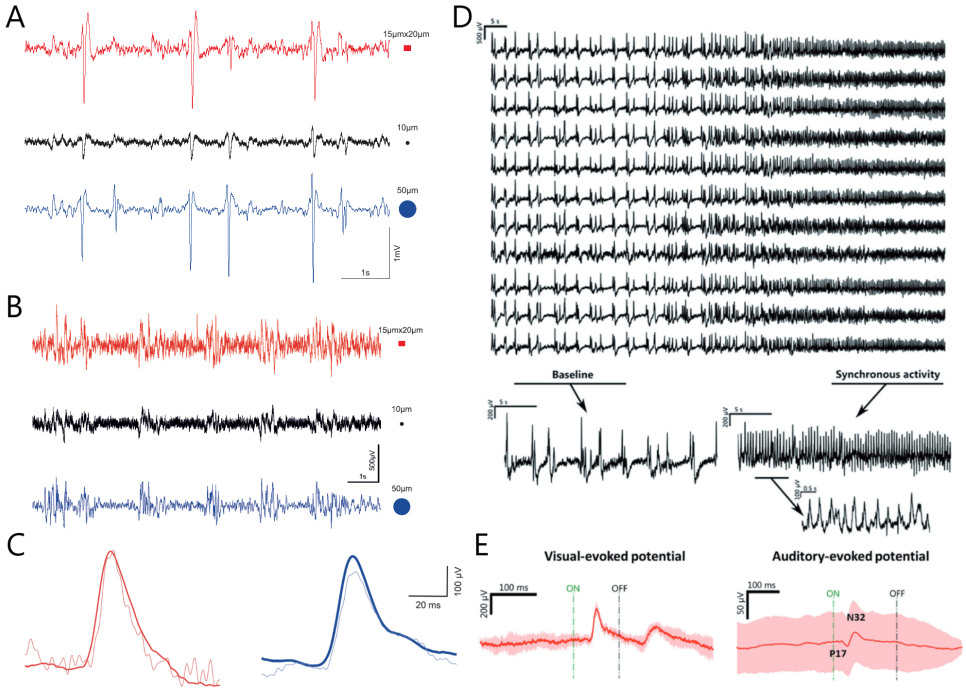

Figure 36. A)-C) Concurrent measurements of a rat's visual cortex using a LGGFET (red) and platinum microelectrodes of different active area diameters (black and blue). A) shows pre-epileptic activity induced by bicuculline, B) spontaneous brain activity during deep anesthesia and C) a single (lighter) and averaged over 66 measurements (darker) events induced by LED stimulation. D) shows spontaneous synchronous activity and E) potentials evoked by visual and auditory stimuli. D) and E) reprinted with permission from reference 68.

measured from the left hemisphere and induced by 8 kHz pure tones (100 ms duration with 3 ms rise and 30 ms fall time). The low amplitude of the auditory-evoked signal was partly assessed to be due to imperfect placement of the array on the location corresponding to 8 kHz.

Recording signals from the cortex surface yields an ensemble of signals from the underlying neurons. Depth probes, classically consisting of things like microwires, provide the best infor-

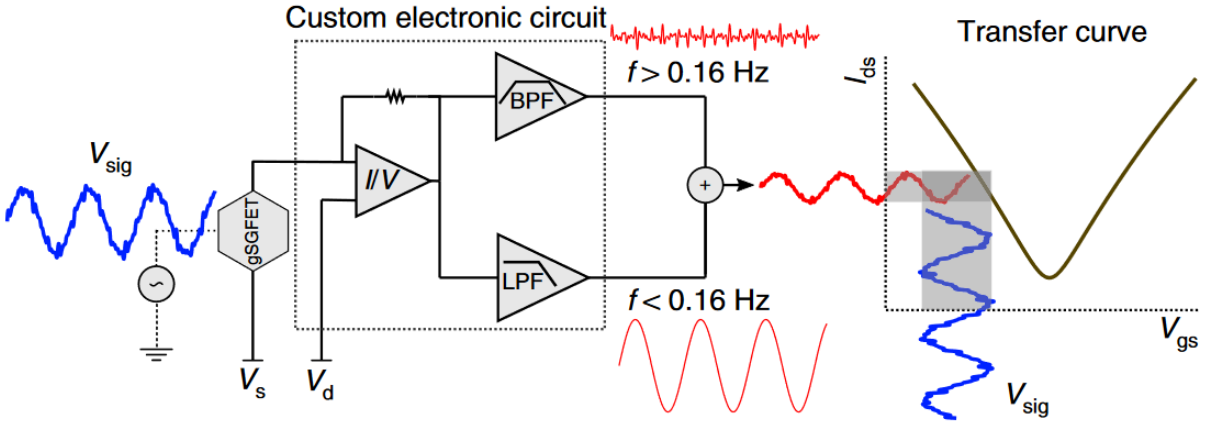

Figure 37. A measurement setup used for simultaneously measuring AC and DC signals. A low pass filter and a band pass filter are used to separate the signals. V_{sig} is the voltage signal amplitude.

mation about the proceedings of the neurons, but can cause inflammatory responses and even loss of neurons. Du *et al.*[70] developed dual modality probes based on LGGFETs for measuring the potential signals from a rat's brain. Two probes were used simultaneously. The first one was bent onto the surface of the lateral parietal association cortex, and the second one was inserted 800 µm deep into the primary somatosensory cortex with 1000 µm lateral separation between the two arrays. It was found that during two weeks of implantation, only minor glial damage was inflicted onto the cortex tissue, which was consistent with the effect of earlier depth probes.

Applying penicillin to the brain surface was used to introduce epileptiform activity, and the dual modality measurements are presented in figure 38. It is noticeable from the data that at the beginning of the measurements, the amplitude of the signals first increases and then stabilizes. The surface probe introduced three to five times larger signal amplitudes, which is due to larger penicillin concentration on the surface. At the beginning of the activity, the depth recordings also trailed the surface recordings by 30 – 40 ms, implying that the activity originates from the surface region. On the other hand, synchrony between the regions increases as the amplitudes rises, as the delay between the spikes lowers.

Brain activity happening at frequencies lower than 0.1 Hz is called infraslow activity and it is connected to such things as brain states. Cortical spreading depression (CSD) also happens at these frequencies. CSD is a wave of hyperactivity followed by a wave of suppressed activity.

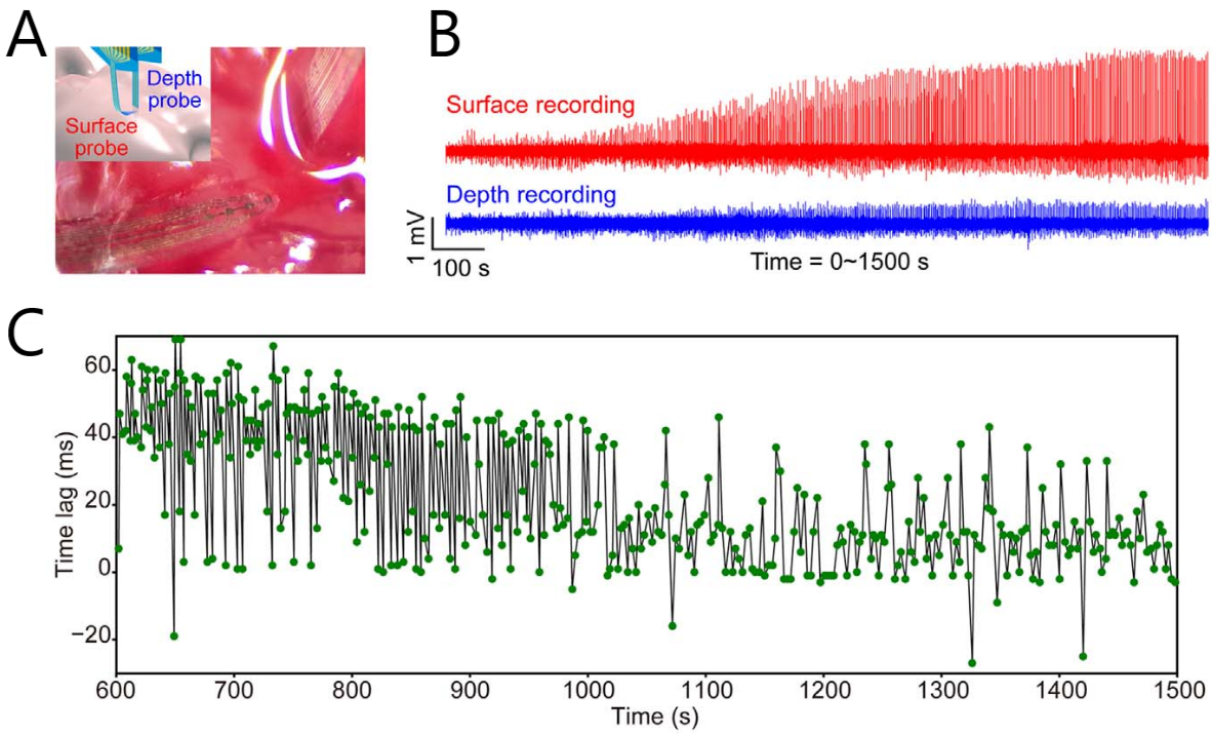

Figure 38. A) optical image and a schematic representation of the measurement setup, B) real time measurement of epiletpiform activity on a rat's brain, and C) time delay between correponding spikes as a function of time. Reprinted from reference 70, copyright 2018, with permission from Elsevier.

CSD can be observed in persons suffering a stroke or during migraines. Typical measurements have consisted of either different kinds of electrodes directly on top of the brain or noninvasive techniques such as electroencephalography and magnetoencephalography. Limitations in the electrode measurements include, but are not limited to, low spatial resolution, intrinsic high-pass filtering and possible toxicity of the electrodes. The noninvasive techniques suffer also from poor spatial resolution, and averaged signal.[5]

Masvidal-Codina *et al.*[5] fabricated GFETs to measure these very low frequencies. The devices were tested from 10^{-2} Hz to 10^{3} Hz and were found to have only little deviation in their transconductances. They measured CSD induced by 5 mM KCl on Wistar rats. They used similar setup as in figure 37 on a array of 14 transistors. Their low pass filter was at $frequency < 0.16\,\text{Hz}$ and band pass filter at $0.16\,\text{Hz} < frequency < 160\,\text{kHz}$. Here the low pass filter measures the CSD whereas the signal bypassing the band pass filter is the local field potential. The measurements are presented in figure 39 A, where the inhibition of the local field potential after CSD is evident. The polarization of the CSD signal is due to the transistor being polarized in the hole conduction regime.

The group also used the array to map the spreading of the CSD. The epicordial mapping reveals that while the initial signal is similar for all the transistors, the following recovery differs between areas. This is shown on the spatial map of the transistors in figure 39 B. It is worth highlighting that this information is lost in recordings using microelectrodes concurrently with high-pass filters, where only the initial signal onset is perceived. CSD results also in increase in regional cerebral blood flow, but earlier measurements on the coupling between the two have been lacking. By combining the lateral mapping with laser speckle contrast imaging, the group was able to show the simultaneous nature of these two events, as shown in figure 39 C. An intracordial array of 15 transistors, was also used to map entire depth of the rat cortex and corpus callosum. In figure 39 D the depth evolution of the CSD is clearly shown, alongside a schematic of the depth probe.

Table 8. Details of LGGFETS for *in vivo* detection. The transconductances are measured *in vivo*.

Material	Substrate	W/L	Array	$\lvert g_\text{m}\rvert V_\text{DS}^{-1}$	$\lvert g_m\rvert V_\text{DS}^{-1}\square$	Year	Ref
Graphene	PI	20 x 15 μm^2	16	$\sim$1 mS V^{-1}	$\sim$0.75 mS V^{-1}	2017	69
Graphene	PI	80 x 30 μm^2	16	1 mS V^{-1} (1)	0.375 mSV^{-1}	2018	68
Graphene	SU-8	30 x 20 μm^2	8	0.9 mS(1)		2018	70
Graphene	PI	100 x 50 μm^2	16	$\sim$0.27 mS	$\sim$0.14 mS	2019	5

(1) measured at V=0, in PBS

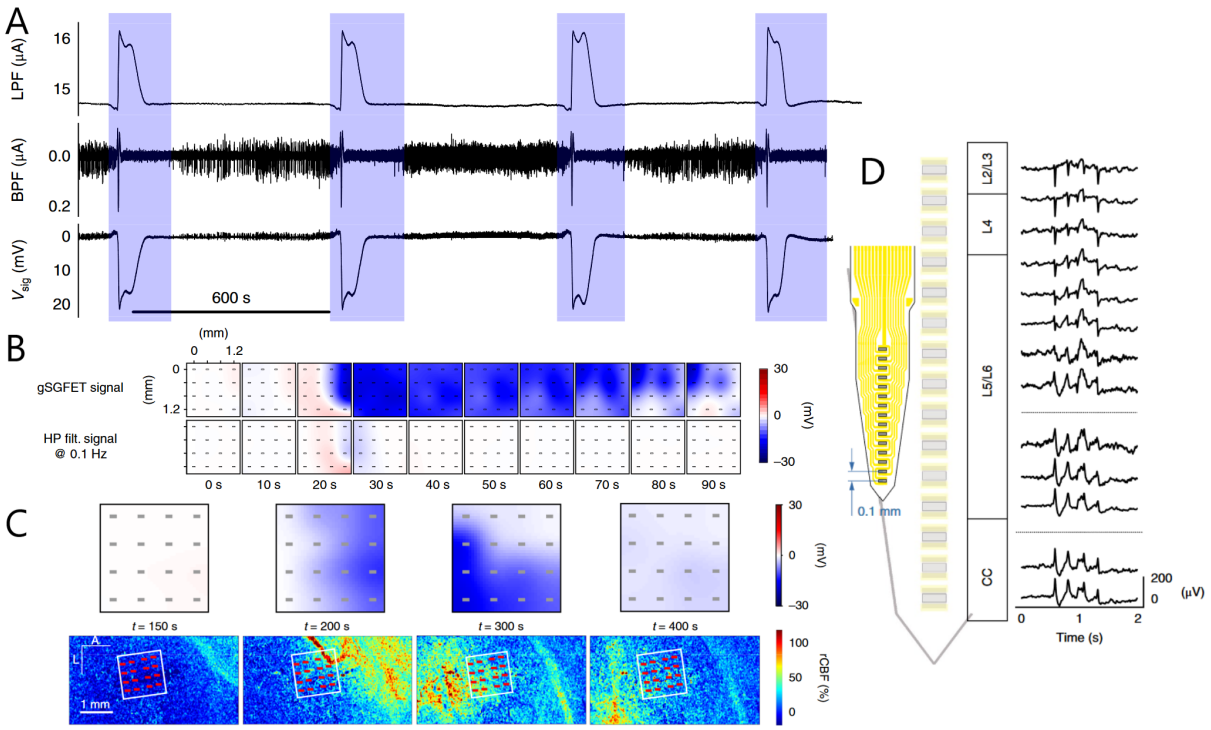

Figure 39. A) Recordings of CSD after four inductions (blue shade). B) Spatial mapping of CSD using a GFET and a high-pass electrodes. C) Simultaneous spatial mapping of CSD and regional cerebral blood flow. D) A schematic of an intracordial probe and depth measurements at different cortex layers (L1 - L6) and corpus callosum. Reprinted by permission from Springer Nature: reference 5, copyright 2019.

6 Summary

Graphene is a two-dimensional allotrope of carbon that has the atoms arranged in a hexagonal lattice. The carbon atoms are sp^2-hybridized and form three σ-bonds with neighbouring atoms, leaving the last valence electron to the p orbital and leading to a filled π band and an empty π^* band. This bonding leads to graphene being extremely strong and flexible, and to it having remarkable electrical properties. Graphene can have charge carrier mobilities as high as $200\,000\,\mathrm{cm^2\,V^{-1}s^{-1}}$, which is hundreds of times higher than those in silicon. Graphene is also a zero-gap semiconductor, i.e. the density of states at the intersection of conduction and valence bands is vanishingly small, and it has a conical energy spectrum near the Fermi energy. The material's electrical properties can be altered by chemical and electrical doping.

A graphene field effect transistor has a sheet of graphene as a conducting channel and an external gate electrode behind an insulating layer for detection or amplification. Typical measured parameters are drain-to-source current as a function of gate voltge, an especially the maximum transconductance $g_\mathrm{m} = \Delta I_\mathrm{DS}\,\Delta V_\mathrm{GS}^{-1}$, charge carrier mobility and Dirac point location. The $I_\mathrm{DS} - V_\mathrm{G}$ curves are V-shaped because of the ambipolar nature of graphene. The shape is typically somewhat asymmetric, due to impurities of the substrate and access resistance between the graphene and the source and drain electrodes. Effectiveness of the transistor can be increased

by incorporating a liquid gate or by etching off the substrate. Liquid gating makes GFETs well suited for biological sensing as most targets reside naturally in aqueous media.

GFETs are naturally sensitive to certain small molecules, such as hydronium and hydroxyl ions. These are detected as they modulate the electric double layer on the graphene's surface, but the detection is in no way selective. LGGFETs have also been functionalized in a multitude of ways to detect even femtomolar concentrations of biological molecules with high selectivity. Graphene, and rGO, can be functionalized by covalently or noncovalently binding active elements to their surface. These active elements can then either break down the target molecules to release molecules that are detected by the graphene, or the target molecules themselves can be altered to change their effect on the surface. Functionalization of the gate electrode is also done sometimes. Lastly, the reaction speed of the probe molecules with the targets is the detection rate limiting step and as such, real time detection of most targets is usually achievable.

Neurological sensing using GFETs is typically conducted using an arrays of transistors placed on top of the cerebral cortex and/or penetrating into it. GFETs have been used to measure signals induced by visually or auditorily stimulating the subjects, pre-epileptic activity induced by chemicals, and infraslow activity. These arrays have been shown to outperform the classical invasive methods in spatial and temporal resolutions.

Experimental section

7 Objectives

As the end goal of the project is the development of an interface between nerves and machines, it is important to know the behavior of proteins on a graphene surface. In the experimental section of this thesis, protein adhesion to two-photon oxidized graphene was studied. Samples with grids of oxidized graphene were coated with a layer of biotinylated BSA (b-BSA), which was then functionalized with a dye molecule *via* another protein.

BSA is a 68 kDa protein that can typically be considered as a prolated ellipsoid, with dimensions of 40 Å and 140 Å.[71] B-BSA was functionalized with 8 – 16 mol of biotin per mol albumin. The biotin molecules were covalently attached through their carboxy groups to the amino groups of the protein, forming an amide bond. The utilized dye molecule was fluorescein isothiocyanate (FITC). It is the most commonly used[72] green-fluorescent labeling dye. FITC was covalently bound to avidin with a labeling ratio of 2 – 4 mol FITC per mol avidin. Avidin is a tetrameric 66 kDa protein, that can bind to biotin with a dissociation constant of 1.3×10^{-15} M. The binding sites lie 9 Å deep within each of the subunits. The binding is so strong, that the conditions required for breaking the bond also dissociate the protein subunits.[73] The structures of BSA, biotin, avidin and FITC are presented in figure 40.

The samples were studied with atomic force microscopy (AFM), Raman spectroscopy and fluorescence lifetime imaging (FLIM). AFM was used to monitor the sample's condition and surface properties, Raman to follow the state of oxidization, and FLIM to measure the fluorescence quenching effects of graphene.

8 Theoretical background

8.1 On two-photon oxidized graphene

The properties of graphene are known to be tunable by bending and doping, as well as by changing its shape and dimensions.[74] Patterning by lithographic methods has its own problems with disorder, especially at the edges, induced by the lithographic process. Bending graphene on the other hand faces adversity when creating complex shapes.[75,76] Chemically oxidizing graphene creates a tunable bandgap, but the doping takes place on the whole surface and is irreversible due to the amount of damage induced to the graphene. These problems can be overcome by using femtosecond laser induced two-photon oxidation of graphene. Using this method, the graphene network alongside its electrical properties are preserved outside of the oxidized zones. The electrical properties are naturally affected in the oxidized zones, allowing for good control by using different levels of oxidation and different sizes of the affected zones.[74]

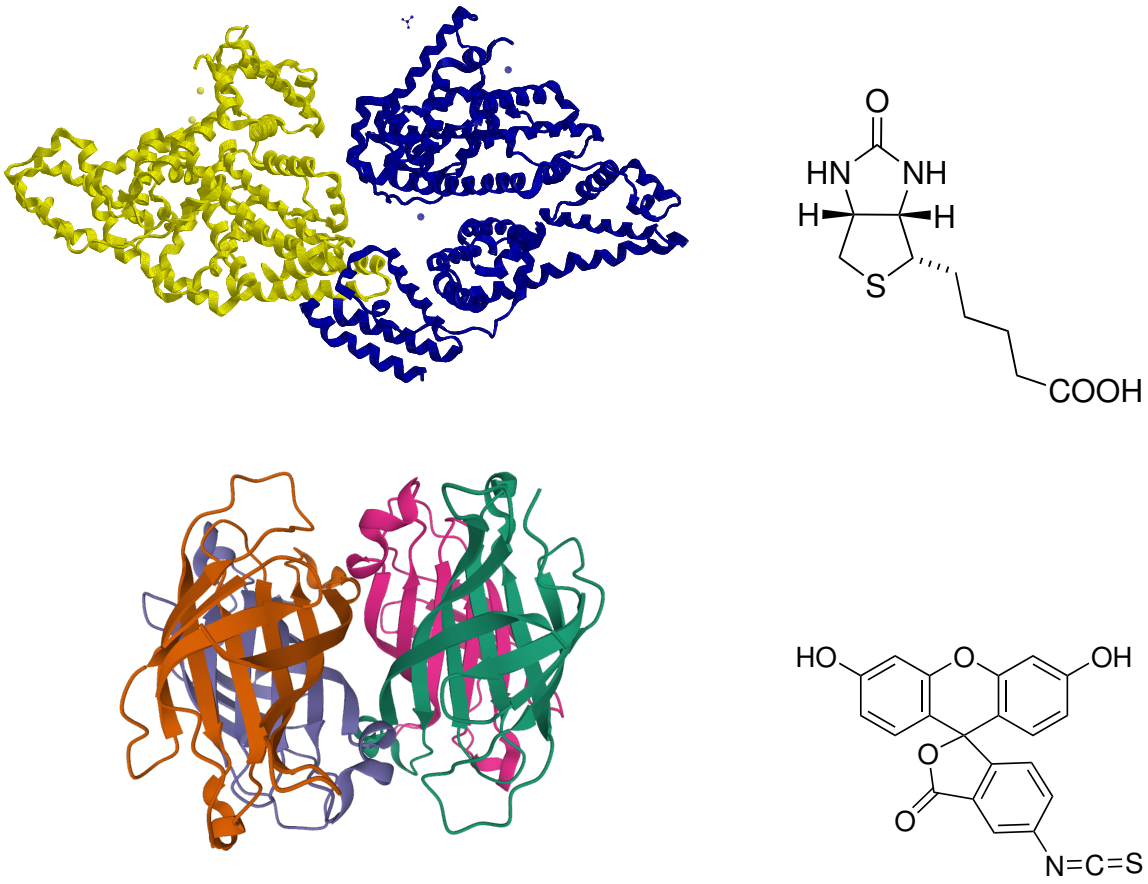

Figure 40. The structures of BSA (top left, PDB structure 3V03), biotin (top right), avidin (bottom left, PDB structure 1VYO), and FITC (bottom right).

The formation of the oxidized zones starts by creation of point-like oxidized seeds, which then begin to grow until they merge into larger islands, and finally the complete oxidized area. The level of oxidation is not completely proportional to the oxidation time, as things like ambient conditions can alter the result. Composition of the oxidized areas differs notably from chemically oxidized graphene. GO usually contains roughly the same amount of epoxide, hydroxyl and carboxyl groups. If GO is oxidized heavily, the epoxide groups start to dominate to some extent. In two-photon oxidized graphene, hydroxyl groups dominate epoxide groups somewhat, but when 70 % of the carbons have been oxidized, less than 5 % of them contain carboxyl groups.[77]

8.2 Surface chemistry of biotinylated BSA

The structure of BSA is constructed of >72 % of α-helix. It can be divided into three structurally similar domains, each of which contains two sub-domains. BSA is know to adsorb onto graphene, as discussed earlier (section 4.1). The conformation of BSA is readily altered by external factors, such as binding to hydrophobic or hydrophilic surfaces. When binding to hydrophobic surfaces, the protein rearranges its secondary and tertiary structure so that its hydrophobic groups, typically contained within the molecule, become available for binding.

Step edges are also expected to increase protein binding, alongside chemical activity, due to more binding sites for anchorage.[78,79] When binding to GO, strong hydrogen bonds between the surface and the protein are responsible for most of the damage to the protein's structure.[80]

Up to 50% of α helixes of BSA are denaturated when it adsorbs to a silica surface. A monolayer of protein adsorbed to this surface always has a thickness less than 40 Å, meaning that BSA adsorbs with longitudal axis parallel to the surface. The BSA layer thickness increases as a function of incubation solution concentration. This leads to the conclusion that the degree of denaturation decreases as BSA concentration increases.[81] The binding of BSA onto surfaces is also a function of their roughness.[78]

Rubio-Pereda *et al.*[79] have conducted molecular dynamics simulations on the binding of BSA onto few-layered graphene. It should be noted that hydrophobicity of few-layered graphene is different from monolayer graphene, and thus the results cannot be directly translated. They found that van der Waals forces have a major contribution to the binding, but that binding by the hydrophilic sites was also worth mentioning. Ionic strength of the solution also affects the interactions.

8.3 Förster resonance energy transfer

Fluorescence has many properties, including quantum yield, wavelength, polarization and lifetime, that are used widely for different sensing purposes. Fluorescence lifetime represents the average time a molecule spends in the excited state before emitting a photon, and it can be used to probe the molecular environment of a molecule. This is done by studying changes in the dye's decay kinetics. Alterations can be caused by the surroundings offering alternate relaxation pathways for the excited state. An often used theory for modeling the change is Förster resonance energy transfer (FRET), that describes the transfer of energy from the excited state (donor) to a suitable acceptor. An excited fluorophore can be thought of as antenna, with an oscillating electromagnetic field around it. Two molecules close to each other can couple resonantly to each other, leading to transfer of energy by a Coulombic mechanism. Assuming that the process follows Fermi golden rule, the transition can be written as

$$k_{\mathrm{T}} = \frac{2\pi}{\hbar} |\left\langle \mathrm{D}^{*}\mathrm{A}\right| \mathbb{H}_{\mathrm{int}} \left|\mathrm{DA}^{*}\right\rangle|^{2} \rho(E_{\mathrm{D}^{*}\mathrm{A}} = E_{\mathrm{DA}^{*}}), \tag{22}$$

where D and A denote the donor and acceptor respectively, * indicates the excited state, and the interaction Hamiltonian is

$$\mathbb{H}_{\mathrm{int}} = \frac{\boldsymbol{\mu}_{\mathrm{A}}\boldsymbol{\mu}_{\mathrm{D}}}{4\pi\varepsilon_{0}n^{2}r^{3}} - \frac{3(\boldsymbol{\mu}_{\mathrm{A}}\mathbf{R}_{\mathrm{AD}})(\boldsymbol{\mu}_{\mathrm{D}}\mathbf{R}_{\mathrm{AD}})}{4\pi\varepsilon_{0}n^{2}r^{5}}, \tag{23}$$

where $\boldsymbol{\mu}$ is the transition dipole moment vector, r the distance between the molecules, $\boldsymbol{R}_{\mathrm{AD}}$ the vector between the molecules, and n the refractive index. Lumping all the orientational

dependence into a dimensionless parameter κ, the Hamiltonian can be written as

$$\mathbb{H}_{\text{int}} = \frac{\kappa}{4\pi\varepsilon_0 n^2}\frac{\mu_{\text{A}}\mu_{\text{D}}}{r^3}, \tag{24}$$

where μ is the transition dipole moment magnitude. This treatment assumes that the states are single eigenstates with well-defined energies. Real molecules exist typically as a Boltzmann distribution of vibrational states, with a variety of possible transition targets.[82,83] This is why in practise, other formulations are more commonly used. The rate of FRET can be written as

$$k_{\text{T}}(r) = \frac{1}{\tau_{\text{D}}}\left(\frac{R_0}{r}\right)^6, \tag{25}$$

where τ_{D} is the lifetime of the donor with no acceptor present, and R_0 is the critical distance, where the rate of FRET equals the rate of radiation. Here the extreme distance dependence can be seen, as the rate is proportional to the inverse of the sixth power of the intermolecule distance. The critical distance, or Förster distance, can be calculated by

$$R_0^6 = \frac{9\ln 10}{125\pi^5 N_{\text{A}}}\frac{\kappa^2\Phi_{\text{D}}}{n^4}J(\lambda), \qquad J(\lambda) = \int_0^\infty F_{\text{qD}}(\lambda)\varepsilon_{\text{A}}(\lambda)\lambda^4 \text{d}\lambda, \tag{26}$$

where N_{A} is the Avogadro constant, κ^2 the oriental factor of the donor and acceptor dipoles, Φ_{D} the donor quantum yield, and $J(\lambda)$ the spectral overlap integral. The integral includes the terms F_{qD} for donor quantal spectrum (proportion of donor fluorescence yield that falls in $\text{d}\lambda$), ε_{A} the acceptor extinction coefficient, and λ the wavelength. A statistical average value of $^2/_3$ for κ^2 is often used for free molecules, but it should be noted that degrees of freedom can be restricted, for example, by binding the molecules to proteins. The distance dependence can also be seen at the equation of FRET efficiency

$$E = \frac{k_{\text{T}}(r)}{\tau_{\text{D}}^{-1} + k_{\text{T}}(r)} = \frac{R_0^6}{r^6 + R_0^6}. \tag{27}$$

For a case where the donor approaches a 2D plane of acceptor molecules at a density ρ and a perpendicular distance r, the expression of efficiency changes to

$$E_{\text{plane}} = \frac{R_0^6}{\left(\frac{2}{\pi\rho}\right)r^4 + R_0^6}, \tag{28}$$

which is dependent only on the fourth power of distance between the surface and the donor. This situation is analogous to a FITC molecule approaching graphene surface.[83]

8.4 Fluorescence quenching of graphene

Graphene is known to quench the fluorescence of dye molecules.[78,84] The quenching mechanism was first theoretically examined by Swathi and Sebastian,[85–87] who modeled the graphene surface according to the tight binding model and Dirac cone approximation. Dipolar approximation was used for the interarction, i.e. it was again thought of as Coulombic, essentially the same as in FRET. They arrived at a rate equation

$$k(r) = \frac{3\pi e^2}{512\Omega h^2 \varepsilon_0^2} \frac{\mu_{\mathrm{eg}}^2 \sin^2\theta^2 + 2\mu_{\mathrm{eg}}^2 \cos^2\theta}{r^4}, \tag{29}$$

where μ_{eg} is the modulus of the transition dipole moment of the dye, θ is the angle between the transition dipole moment and the line orthogonal to the graphene surface, and Ω is the frequency related to the energy between two energy levels

$$\Delta E_{\mathrm{eq}} = E_{\mathrm{e}} - E_{\mathrm{g}} = \hbar\Omega, \tag{30}$$

where E_{e} and E_{g} are the energies of the excited and ground states. Equation (29) displays a clear dependence on the inverse of the fourth power of distance, and it is valid for distances of 20 – 400 Å. The deviation is not large even for shorter distances. According to this equation, the critical distance for quenching of pyrene fluorescence by graphene is 300 Å, which is extremely long. Averaging over all possible transition dipole moment orientations, the expectation value

$$\langle k(r) \rangle = \frac{\pi e^2}{64\Omega h^2 \varepsilon_0^2} \frac{\mu_{\mathrm{eg}}^2}{r^4} \tag{31}$$

can be derived. Gaudreau *et al.*[88] have worked out a similar equation for the quenching, where the rate does not depend on the properties of graphene, for 1 – 15 nm separation between the graphene and the fluorophore. In this equation the rate of transfer from the emitter to graphene (Γ_g) is given by

$$\frac{\Gamma_g}{\Gamma_0} \approx 1 + \frac{3^2 \nu}{2^8 \pi^3 (\varepsilon + 1)^2} \alpha \left(\frac{\lambda_0}{r} \right)^4, \tag{32}$$

which is dependent on the emission rate and wavelength of the fluorophore in absence of graphene (Γ_0 and λ_0), permittivity of the substrate (ε), and the orientation of the emitting dipole ($\nu = 1$ for parallel and $\nu = 2$ for perpendicular orientation). $\alpha = e^2 (2\varepsilon_0 hc)^{-1}$ is the fine-structure constant. They found that the relation fits to the experimental results well without any additional fitting parameters. Chen *et al.*,[89] Lee *et al.*[90] and Kaminska *et al.*[91] have experimentally verified the r^{-4} dependence.

Doping graphene changes the quenching properties.[80,85,90,92] Lowering the Fermi level of graphene below half of the photon's energy disables the interband transition due to depletion of the electrons. On the other hand, if the Fermi level is increased by the same amount, filling of the

conduction band by electrons forbids the transition. This is presented graphically in figure 41. Besides electron-hole interactions, doped graphene $|E_F > \hbar\omega|$ can have its plasmons excited, providing a new pathway for quenching of fluorescence. Plasmons are the collective oscillations of delocalized electrons. The quenching effect can be calculated by[93]

$$\Gamma_{sp} \approx \frac{(2\pi)^4}{(\varepsilon+1)\hbar}(|\mathbf{d}_{\parallel}|^2 + 2|\mathbf{d}_{\perp}|^2)\frac{e^{-\frac{4\pi r}{\lambda_{sp}}}}{\lambda_{sp}^3,} \tag{33}$$

where $\mathbf{d}_{\parallel}$ and $\mathbf{d}_{\perp}$ are the dipole matrix element contributions parallel and perpendicular to the graphene, and λ_{sp} the surface plasmon wavelength. This evaluation is within the random phase approximation. The exponential effect of plasmons on the rate of decay is presented in figure 42. Plasmons dominate the decay below E_F, after which there is a dip in the rate. This is followed by onset of interband transitions at $\hbar\omega = E_F$, after which the rate returns to a value independent of E_F and begins to resemble the case of undoped graphene.[90,93]

Besides pure electrical doping, inducing defects into the graphene also changes the quenching properties. Guo *et al.*[94] measured the quenching efficiency of graphene treated with hydrogen and Ar^+ plasma. Hydrogenation creates sp^3 type defects to the graphene, which makes the graphene more insulating. The Ar^+ plasma treatment on the other hand creates vacancies in the electronic structure of graphene. Both of these reduce the amount of available unbound carriers for the graphene, thus decreasing the effect of energy transfer. They also found that at similar defect densities, the hydrogen plasma treatment had a more pronounced effect on the quenching efficiency. This indicates that the nature of defects also affects the quenching properties.

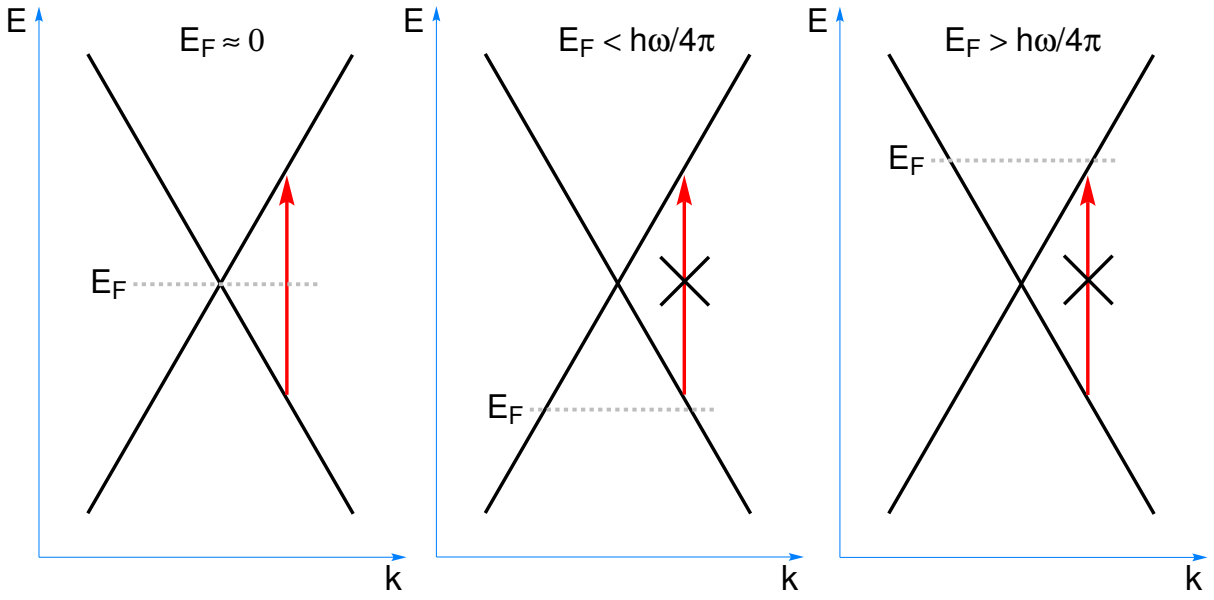

Figure 41. The effect of doping on interband transitions of graphene electrons.

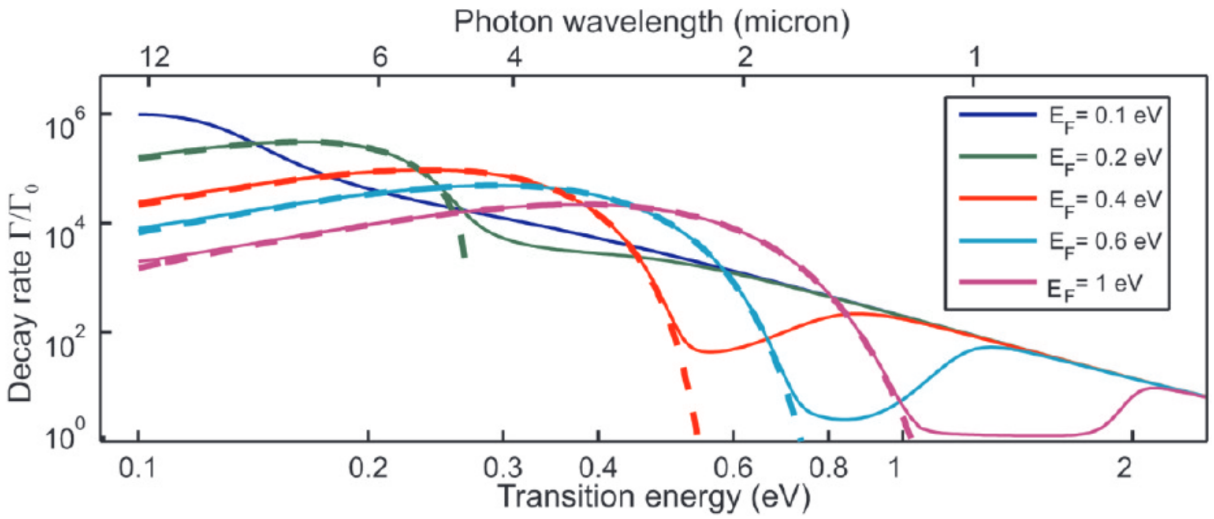

Figure 42. Decay rate of an excited emitter perpendicular to a graphene surface, with a 10 nm separation, at different Fermi energies. The decay rate is normalized to the value without graphene present. Solid line represent the total decay rate, and the dashed lines show the contribution of the surface plasmons. Reprinted with permission from reference 93. Copyright 2011 American Chemical Society.

8.5 Fluorescence of the probe molecule

Free FITC exhibits a single fluorescence lifetime of 3.7 – 4.1 ns, depending on pH. Increasing FITC concentration is also known to lower its lifetime due to dynamic fluorescence quenching, i.e. the dye molecules quench the fluorescence of one another through FRET.[78] FITC is prone to photobleaching and as such it should be kept covered from excessive light, preferably in a refridgerator.[72]

Covalently binding of FITC to BSA through their isothiocyanate and ε-amino groups provides the dye's excited state other possible relaxation pathways. There are multiple available ε-amino groups in BSA for binding, and it is not specific to any one. Binding forces the dye molecules close to each other, and thus quenches the fluorescence intensity and causes the emergence of additional lifetimes.[72,78] Tryptophan and tyrosine may also quench FITC fluorescence[71,78]

Average lifetime of BSA-FITC is known to decrease as labeling ratio increases.[95] Different lifetimes result from different ranges between dye molecules. The longest lifetime can be attributed to FITC located at the outer rim of BSA, whereas intermediate lifetime components are due to FITC molecules closer to each other. The shortest one can be caused by high local concentration of dyes, or even their dimerization.[81,95,96] Also in some cases, especially short lifetimes (i.e. $\sim$0.1 ns) may be just artifacts caused by backscattering of excitation light.

Different lifetimes measured for BSA-FITC in different solutions and bound to certain surfaces are presented in table 9. Variance can easily be found between different conditions in solution, different labeling ratios and different substrates. At lower labeling ratios, two lifetimes are usually present. Increase in the ratio, or adhesion of BSA to a substrate introduces a third one. In

the case of nanodiamond substrate, a fourth one is observed. BSA binding to different surfaces results in various secondary and tertiary structures for the protein. This in turn changes the inter dye distances, as well as the distances between dye molecules and the surface. This results in different lifetimes upon adsorption.[78] The longest lifetimes on polycaprolactone surfaces were deemed to be most likely caused by the surface, instead of the dye molecule.[96]

Table 9. BSA-FITC lifetimes at different environments

FITC:BSA	Solvent/ surface	τ_1 [ns]	τ_2 [ns]	τ_3 [ns]	τ_4 [ns]	Ref
1:1	PBS, pH 7.4	1.00	3.98	-	-	95
2:1	PBS, pH 7.4	1.02	3.93	-	-	95
3:1	PBS, pH 7.4	0.48	1.85	3.61	-	95
7:1	PBS, pH 7.4	1.75	0.45	3.59	-	95
1:1	PBS, pH 7.4, polycaprolactone	1.14	4.12	22	-	96
3:1	PBS, pH 7.4, polycaprolactone	1.35	4.42	25.2	-	96
10:1	PBS, pH 7.4, polycaprolactone	1.16	3.73	17	-	96
1:1	0.1 M Na_2CO_3	0.81	3.91	-	-	71
1:1	0.1 M Na_2CO_3, hydrophilic	0.67	2.95	-	-	71
1:1	0.1 M Na_2CO_3, hydrophobic	0.81	3.91	-	-	71
5:1	0.1 M Na_2CO_3	0.64	3.62	-	-	71
5:1	0.1 M Na_2CO_3, hydrophilic	0.52	2.74	-	-	71
5:1	0.1 M Na_2CO_3, hydrophobic	0.60	2.23	-	-	71
7-12:1	Tris, pH 7	0.28	1.04	3.17	-	78
7-12:1	Tris, pH 7 β-SiC	0.13	0.66	3.71	-	78
7-12:1	Tris, pH 7 nanodiamond	0.13	0.66	2.54	3.71	78

8.6 Atomic force microscopy

Atomic force microscopy is an adaptation upon Nobel prize winning scanning tunneling microscopy. Scanning tunneling microscopy measures a tunneling current between an imaging tip and a sample surface. This technique has an obvious drawback in requiring a conducting sample. Another downside to the method is a requirement of ultrahigh vacuum. Both of these are overcome by AFM. Binnig, Quate, and Gerber realized in 1986 that in the distances where the tunneling current could flow, other intermolecular forces between the tip and the sample were

also strongly present. Measuring these forces abolishes the requirements for conduction and vacuum, as the forces are present at every surface and regardless of adsorption and desorption of ambient molecules on the surface.

The measurement tip is affixed onto a relatively flexible cantilever. For sensing tip-sample forces, the cantilever should be rigid with regard to other directions. As forces affect the tip, the cantilever bends according to Hooke's law. Typically a laser is pointed at a reflective cantilever, and the reflected light is collected. Bending of the cantilever changes the end position of the laser, and information about the bending is extracted from the displacement. As the cantilever should remain at a constant position, the sample is fixed to a piezoelectric stage to allow for repositioning. A schematic of the measurement setup is presented in figure 43. AFM can be run in static and dynamic force operation modes. In measurements of static forces, the force between the tip and the sample is kept constant, and the interpretation is simple: the image is a map of surface height. This mode requires hard tips and samples, and can lead to damaging the sample. On the other hand, deliberate shaping of the sample is made possible. In dynamic modes the cantilever is driven to oscillate at frequency close to its eigenfrequency. Dynamic mode's can be either amplitude or frequency modulated. These were first intended to be used as non-contact, utilizing only the attractive forces between the tip and the sample. A tapping mode, where the tip taps the surface, utilizing also repulsive forces was later introduced.[97]

Tapping mode AFM employs a lock-in amplifier to maintain a constant frequency and amplitude of cantilever oscillation. Constant frequency is maintained through a constant driving frequency, and constant amplitude by changing the tip-sample separation. This results in the attained force curve only including averaged information about the attracting and repulsing interactions.

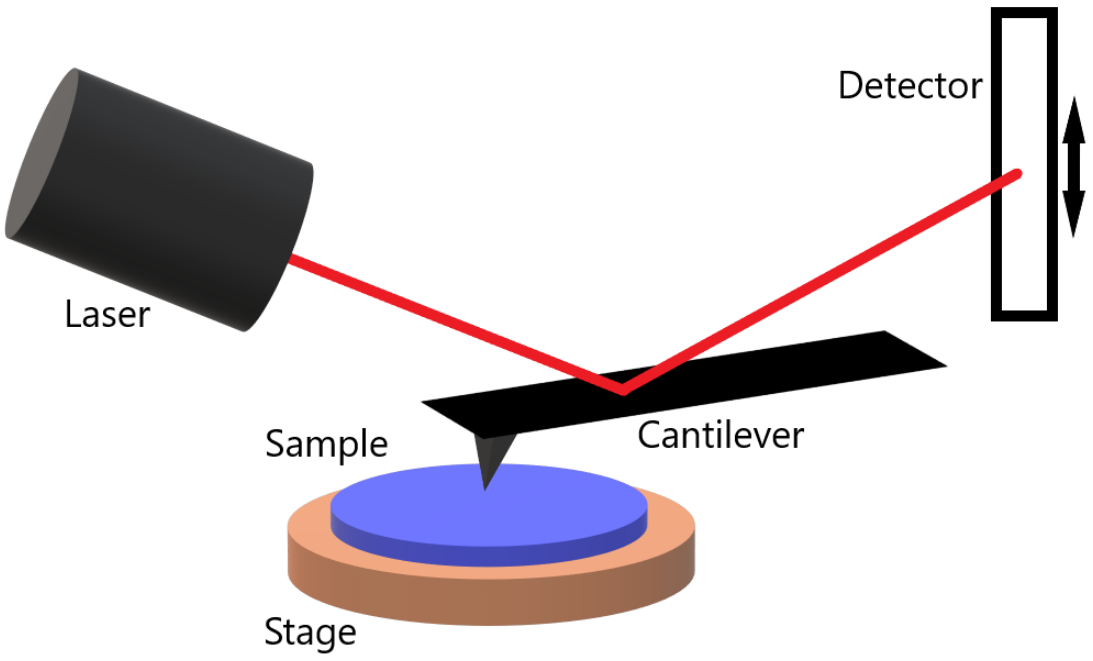

Figure 43. A schematic representation of an AFM measurement.

A significant breakthrough in AFM imaging was the introduction of peak force tapping. It differs in operation principle from regular tapping mode by being operated in frequencies well below the eigenfrequency, avoiding the filtering effect and dynamics of a resonating system. This allows for direct force control. As the tip approaches the surface, it experiences attractive van der Waals forces. Closer to the surface these forces become large enough to snap the tip to contact. After this, the shorter range repulsive forces start dominating the interaction. Retraction is triggered by reaching a set peak force. As the tip begins to retract, it goes through an adhesion minimum, followed by detaching from the surface.[98,99]

8.7 Raman characteristics of graphene

Raman process is the inelastic scattering of incident light. The magnitude of Raman signal is proportional to the polarizability of the target. Polarizability is an anisotropic property, i.e. it can have different magnitudes at the same distances but different directions. When a molecule in a state comes to contact with radiation, that does not correspond to the energy difference between the initial state and any other state, the radiation induces a dipole moment to the molecule. The molecule is now in a virtual state. The molecule can then return to the original energy level when the radiation is scattered. This is called Rayleigh scattering. Sometimes, much more rarely, the molecule returns to a state that is higher or lower in energy, and this is called Raman scattering. When the molecule returns to a higher energy level, it is called a Stokes scattering, and the scattering photon has lower energy. The opposite case is called anti-Stokes scattering. Due to the small probability of Raman scattering, powerful lasers are typically used as sources of electromagnetic radiation. Energy level diagram of the different scattering processes is presented in figure 44.[100]

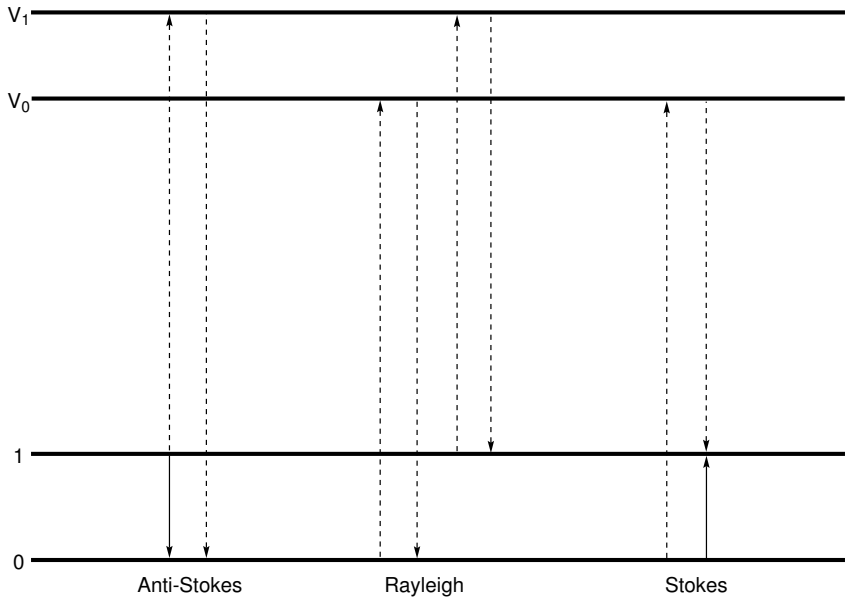

Figure 44. Raman and Rayleigh scattering processes to virtual states V_0 and V_1. Dashed lines indicate the Raman transitions, and solid lines indicate the overall transitions.

The most prominent Raman features of graphene are the D, G and 2D bands, located at 1350 cm^{-1}, 1582 cm^{-1} and 2700 cm^{-1}, respectively (514.5 nm laser excitation wavelength). The G band is a doubly degenerate phonon mode at the Brillouin zone center with E_{2g} symmetry. It represents the presence of sp^2 hybridized networks of carbon. D band is induced by defects in the lattice, as it is a forbidden (A_{1g}[101]) mode in pristine graphene. 2D is any overtone of D band, but as it is symmetry allowed, it can be found even in pristine graphene.[102] Both the D and 2D bands peak positions are a function of irradiation energy. The relationship between integrated areas of D and G peaks has been used for a long time as an indication of defect density. Crystallite size in nanometers can be calculated by

$$L_a = \frac{560}{E_l^4}\left(\frac{I(D)}{I(G)}\right)^{-1}, \tag{34}$$

where $I(D)$ and $I(G)$ are the integrated D and G peak areas, and E_l is the laser energy in electronvolts.[103] As the amount of defects is increased, e.g. by increasing irradiation dose, the Raman spectrum of graphene evolves as follows: first the D band appears, which is followed by widening of the peaks and eventual failure of the equation (34). This behavior is presented in figure 45.[101] The breaking down is because of two competing mechanisms contributing to the D band. Each point defect can be thought as having two circular areas, where the smaller is the area of the damaged graphene network, and the larger is the proximate area that has its energy levels mixed due to the defect. The former area contributes less to the D band due to the lattice breaking down. With lower defect densities, increasing the density increases the D band, as more electrons (or holes) will come in contact with the D band enhancing circles. As the defect density increases sufficiently, new defect sites will have to overlap with the outer rings of other defects, decreasing the D band intensity.[104] Another indicator of disorder is the full width at half maximum of the G peak, the increase of which denotes the decay of the sp^2 hybridized lattice. This can be used, in certain situations, to separate between increasing and decreasing $I(D)/I(G)$ regions.[101] The Raman peaks of two-photon oxidized graphene remain relatively narrow for highly oxidized graphene.[74]

8.8 Fluorescence of graphene oxide

Pristine graphene is not fluorescent. This can be changed by oxidizing the graphene, as GO has a broad emission spectrum, with an emission maximum around 700 nm. The fluorescence has multiple lifetimes: Gokus *et al.*[105] have reported three exponetial components ($\tau_1 = 40\,\mathrm{ps}$, $\tau_2 = 200\,\mathrm{ps}$, $\tau_3 = 1000\,\mathrm{ps}$), whereas Shang *et al.*[106] found four different lifetimes ($\tau_1 = 2\,\mathrm{ps}$, $\tau_2 = 13\,\mathrm{ps}$, $\tau_3 = 90\,\mathrm{ps}$, and $\tau_4 = 2000\,\mathrm{ps}$). The fluorescence is attributed to electron-hole recombination, which is made possible by opening of the band gap. This fluorescence is mostly caused at boundaries between oxidized carbon atoms and sp_2 hybridized regions. All kinds of functional groups participate in causing the photoluminescence.[105,106]

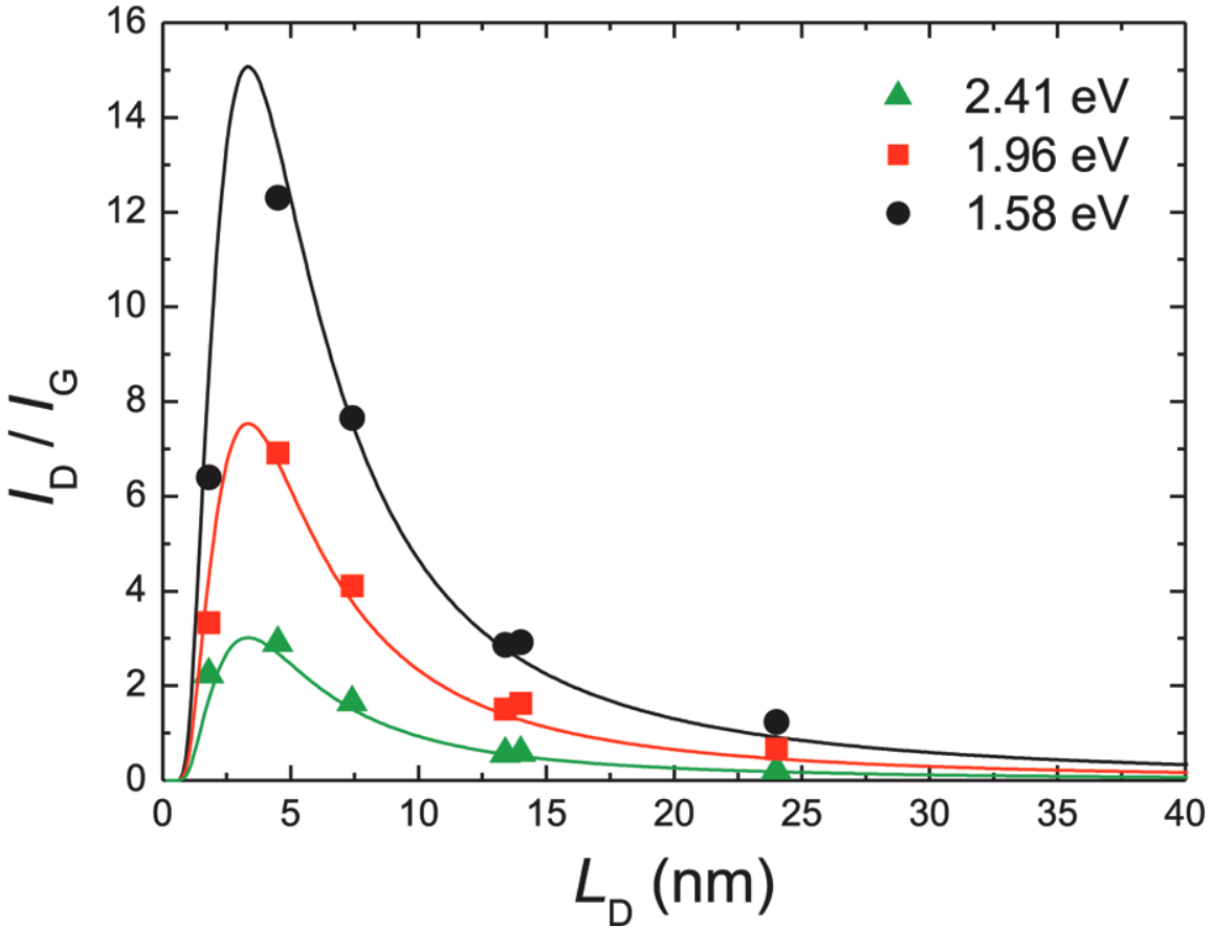

Figure 45. The behavior of $I(\mathrm{D})/I(\mathrm{G})$ as a function of average defect distance. Adapted with permission from reference 101. Copyright 2011 American Chemical Society.

Reduction of GO changes the amount and ratio of oxygen containing functional groups. Different methods of reduction incur different changes.Reduction increases the sp^2 character of graphene, which in turn quenches the fluorescence. This leads to significantly shorter lifetimes, and a blueshift of the steady state fluorescence. It has also been suggested that the change in steady state is due a kinetics effect on the spatially varying band gap, instead of a change in it.[107]

8.9 Fluorescence lifetime imaging microscopy

Fluorescence lifetime imaging microscopy is an imaging technique where contrast is formed by differences in excited state lifetimes. Lifetime is a property of materials that is not dependent on concentration, sample thickness or excitation intensity, which makes it more reliable than emission intensity based methods. However, fluorescence lifetime is affected by external conditions, such as pH, surface adhesion and presence of energy acceptors. This makes FLIM imaging compelling for functional imaging.

Data collection is conducted by time-correlated single photon counting. In this method the sample is illuminated with a pulsed laser. Due to limitations in the detection apparatus, there is a

short dead time after measuring a photon. This can lead to over representation of faster photons, the so called pile-up effect. Pile-up can be counteracted by having lower excitation light intensity and having, approximately, only a single photon emitted during an excitation cycle. The time between excitation and arrival of the emitted photon at the detector is measured and after a sufficient amount of measurements to account for the statistical nature of the emission, the measurements are plotted as a histogram. After taking into account an instrument response function, fitting can be conducted on the data to determine lifetimes. For a monoexponential decay, an error of 10 % can be reached with 185 photons. For biexponential decay, the amount of required photons rises to 10,000–100,000.[108,109] It should be noted that fits with more exponential components, become inherently more untrustworthy, as different decay curves begin to strongly resemble one another. This makes recovering exact lifetimes and amplitudes harder, as lifetimes can be altered to compensate for the amplitude, or vice versa.[110]

In our setup, curve fitting is conducted by the microscope operating program, LAS X, according to equation

$$y(t) = \{\mathrm{IRF}(t + shift_{\mathrm{IRF}}) + Bkgr_{\mathrm{IRF}}\} * \left\{ \sum_{i=0}^{n-1} A[i] e^{\left(-\frac{t}{\tau[i]}\right)} + Bkgr \right\}, \tag{35}$$

where IRF is the instrument response function, t time, n the number of exponential components, $Bkgr$ the tail offset, $Shift_{\mathrm{IRF}}$ the correction for IRF placement, $Bkgr_{\mathrm{IRF}}$ the IRF background, A are the exponential pre-factors, and τ the lifetimes. Goodness of fit is estimated by

$$\chi^2 = \sum i = 1^k \frac{(O_i - E_i)^2}{E_1}, \tag{36}$$

where O_i is the observed value and E_i expected value. A value close to one is desireable.[108]

9 Conduction of experiment

Two chips were prepared, chip **1** and chip **2**. Both of the samples had two two-photon oxidized areas, one of which had a 3x3 grid and the other a 6x6 grid of oxidized squares. The smaller grids are denoted **1** B and **2** E, whereas the larger grids are denoted **1** F and **2** A. Laser irradiation parameters for the grids are presented in figure 46. The squares of the smaller grids are approximately 3 µm wide and the squares of the larger grids approximately 2.5 µm wide. Due to time constraints, chip **2** was never coated with protein, and as such, only some of the measurements have been conducted on it and they are presented when applicable.

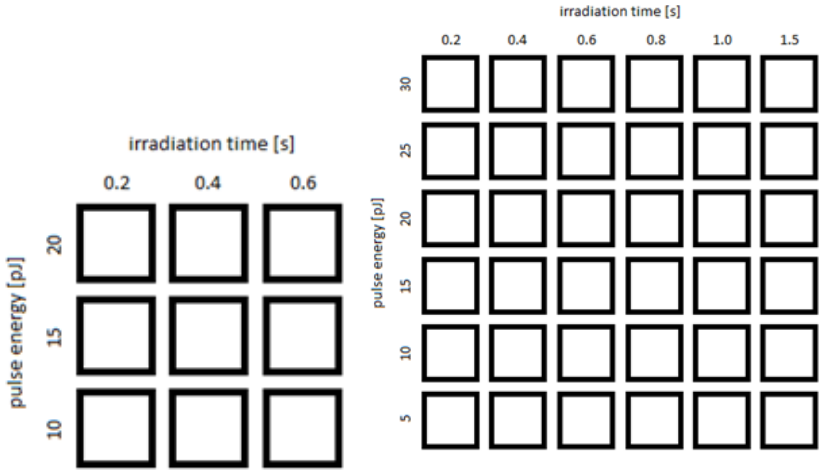

Figure 46. The irradiation parameters of the two-photon oxidized squares for the grids.

9.1 Protein coating of the chip

Chip **1** was coated with b-BSA. This was conducted by incubating the chip in b-BSA solution in room temperature for 24 h. The b-BSA solution was prepared by measuring 0.98 mg of b-BSA (Sigma Aldrich, purity level MG 200, 8 – 16 mol biotin per mol albumin) into 2 mL of PBS (0.1 M, pH 7.3). The PBS solution had been prepared beforehand by dissolving 1.9187 g monosodium phosphate (Merck, pharmaceutical grade) and 6.7110 g disodium phosphate (Merck, analytical grade) into 500 mL of deionized water. The b-BSA solution was diluted by mixing 100 µL of the prepared solution with 4900 µL PBS, for a final concentration of 9.8 mgmL^{-1}. After incubation the chip was washed 10 times with PBS and deionized water.

After protein functionalization the chip was incubated in a solution of Avidin-FITC for an hour. The Avidin-FITC solution was prepared by measuring 0.99 mg of Avidin-FITC (Sigma Aldrich, purity level MG 200, 2 – 4 mol FITC per mol avidin) into a vial with 12.375 mL of PBS for a concentration of 80 µg mL. The vial was covered in foil to prevent photobleaching of the dye, and it was stored in a fridge when not in use. After incubation, the chip was again washed 10 times with PBS and deionized water respectively, and dried by blowing nitrogen on it.

9.2 Optical microscopy

Optical microscopy was conducted on Olympus BX51M. The used objectives were 10× NeoSPlan 10 NIC (NA 0.25) and 50× NeoSPlan 50 NIC (NA 0.70). Optical microscopy images of chip **1** were taken before and after protein coating. Lifetime measurements were conducted on the functionalized chip before optical microscopy, as photobleaching affects the fluorescence intensity but is of little consequence to the optical microscopy.

9.3 Atomic force microscopy

AFM was conducted on Bruker Dimension Icon using peak force quantitative nanomechanical property mapping. The used probes were SCANASYST-AIR. Data analysis was conducted using NanoScope Analysis 1.9. The acquired images were first fitted to plane with a first or second order correction, depending on the image. First order correction accounts for tilt and second order correction for bend. Next the images were flattened to zeroth order. Flattening is also done to eliminate bow and tilt from the image. Oxidized squares, markers, dirt and largest wrinkles were manually excluded from the zeroth order flattening. This was followed by first or second order flattening of the whole image, depending on which made it look better. Height profiles of the squares were measured using step tool, averaging approximately a third of the squares' width, and plotted using Origin.

9.4 Raman

Raman measurements were conducted using a home-built measuring setup with a $\lambda = 532\,\mathrm{nm}$ CW laser (Alphalas, Monolas-532-100-SM). The beam was focused to the sample and collected by a microscope objective (Nikon L Plan SLWD 100x, 0.70 N.A.) The scattered light was dispersed with a 0.5 m imaging spectrograph (Acton, SpectraPro 2500i) using a $600\,\mathrm{mm}^{-1}$ grating, and the signal was detected with an EMCCD camera (Andor Newton EM DU971N-BV). The effect of Rayleigh scattering was diminished with an edge filter (Semrock). A beam splitter was positioned between the objective and the spectrometer for observation of the laser position with a camera. Laser power was 0.25 mW.

Before protein functionalization, single Raman spectra were measured for chip **1**. These were measured from the rows with the largest pulse energies and the columns with the largest irradiation times to observe the chip's state of oxidation. After protein adhesion mapping was conducted on the oxidized regions. Region **1** F was not mapped as the graphene was apparently scraped off the surface of the chip. For chip **2** Raman mapping was conducted before and after protein functionalization, as single spectra were deemed too untrustworthy. The measured spectra were normalized to the silicon band found around $1000\,\mathrm{cm}^{-1}$ by dividing the spectrum by the band's peak value.

The Raman maps were processed by RamanMapViewer provided by Pasi Myllyperkiö. The program provides contour maps of integrated peak area of choice. Further analysis was conducted using OriginPro 2017's Peak Analyzer - Fit Peaks (Pro) functionality. A User Defined baseline was formed using eight manually placed points that were connected by Spline Interpolation. After removal of the baseline, D, G and 2D bands were manually located on the spectra and fitted with Lorentzian functions. Lastly, the spectra were integrated from $1100\,\mathrm{cm}^{-1}$ to $3150\,\mathrm{cm}^{-1}$. From the maps, five spots per square were averaged to obtain more reliable results about the state of oxidization. Tthe extracted spectra were normalized before averaging, but the maps were not normalized.

9.5 Fluorescence lifetime imaging microscopy

FLIM measurements were conducted with Leica SP8 X Falcon confocal microscope. The used objective for dry measurements was Leica HC PL APO (20×, NA 0.75) and for water immersion measurements Leica HC PL APO (63×, NA 1.2). The excitation wavelength was 488 nm and emission was gathered at 498 – 749 nm. Temporal resolution of the device is 97 ps,[111] and an overall dead-time of less than 1.5 ns.[111] Image processing was conducted on LAS X - single molecule detection. Due to the geometry of the microscope, the acquired images were mirror images, and needed to be flipped horizontally. The initial data was presented as a fast FLIM image, where a pixel's average lifetime is presented, red being the longest and green the shortest. Every pixel was then individually fitted with a desired number of exponential components, according to equation 35.

The lifetimes of avidin-FITC were determined in liquid phase using the water immersion objective for the same solution that was used to fabricate chip **1**. The solution was sentrifuged for two minutes at 16.1×10^3 rcf. A drop of the supernatant was placed on a sample holder, and the liquid was measured for two minutes.

Chip **1** was imaged three times: first measurement was done on the dried sample, the second measurement in water immersion after addition of a drop of water, and the third measurement after the sample was dried using nitrogen. The **1** B grid could not be found during water immersion. After global fitting of the imaged area, fits were also conducted for each of the oxidized areas. If the squares contained apparent clusters of longer lifetime components, they were excluded from the fit.

10 Results

10.1 Optical microscopy

Optical microscopy images of chip **1** before and after protein functionalization are presented in figure 47. The oxidized squares are located left of the marker above the number, although they are not visible here. Graphene can be seen as a slightly darker area. The chip has suffered some damage before functionalization, as evident by stripes where the graphene has been peeled off near grids E and F. More damage is easily visible after protein coating as large areas, including the complete functionalized area of grid F, are completely clear of graphene.

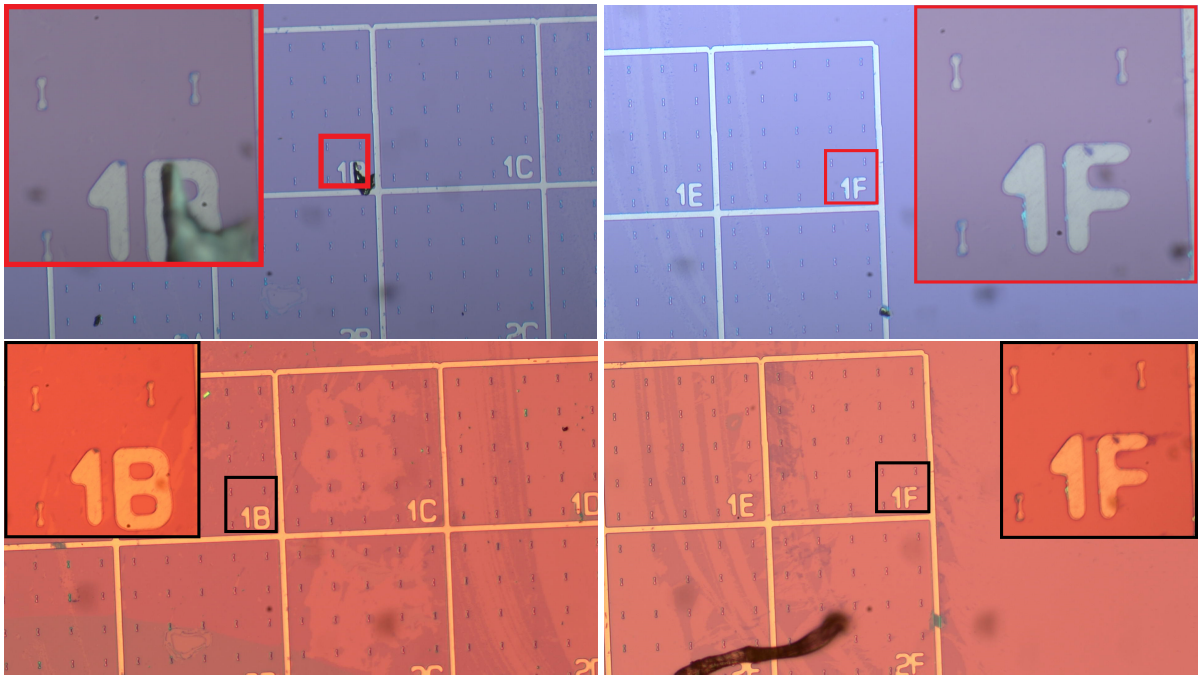

Figure 47. Optical microscopy images of chip **1**. Top row images are taken before and bottom row images after protein immobilization. Insets show the zoomed-in images of the oxidized graphene areas.

10.2 Atomic force microscopy

AFM height sensor images of chip **1** B and F after oxidization are presented in figure 48. The areas have typical ubiquitous wrinkles. It is clear from the pictures that the height of the squares with the same irradiation parameters at different grids do not match. Cross sections of the square heights are presented in figures 49, 50 and 51. There is only little increase in the height of the squares at **1** B rows as a function of increasing irradiation time. For the columns, on the other hand, the effect of laser pulse energy is significant, yet still more prominent on shorter irradiation times. On **1** F a similar trend is distinguishable. The rows show some dependence of square height on irradiation time, but for the columns the effect of laser pulse energy is definitely more significant. The **1** F row with 20 pJ laser pulse energy is somewhat of an outlier, as the peak height maximum is located at the 0.4 s and 0.6 s squares. The bottom row is only faintly

visible for **1** B, and not at all for **1** F. The squares with the shortest irradiation times for the 10 pJ row in **1** F are also disappearing. The heights of the squares were determined by approximating the tops as straight lines at the average height by eyeballing, and assigning a single graphene baseline for a chip. This is illustrated in appendix 1. The baseline for **1** F was at -0.34 nm and at 0.17 nm for **1** B.

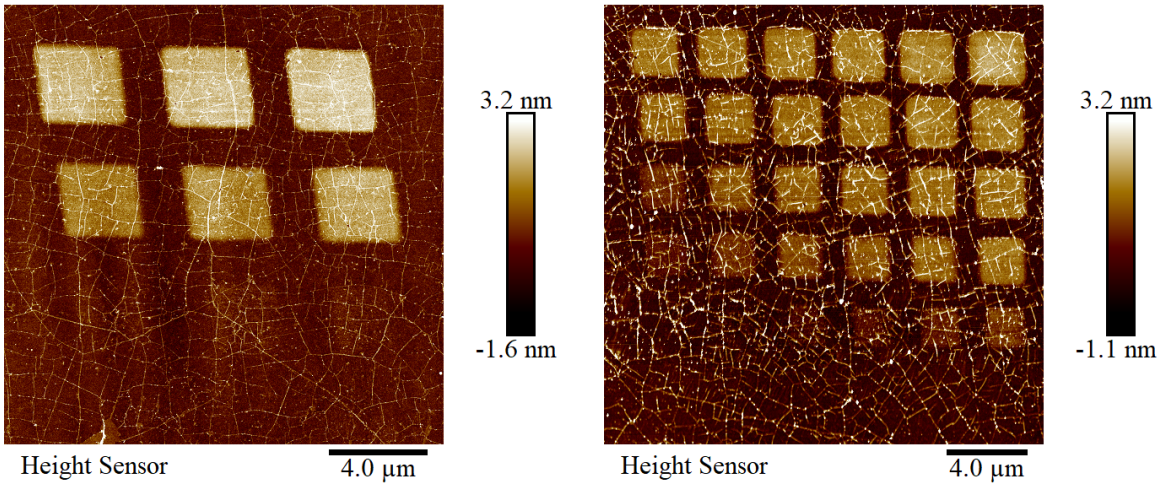

Figure 48. AFM height sensor images of chip **1** B (left) and F (right) after oxidation.

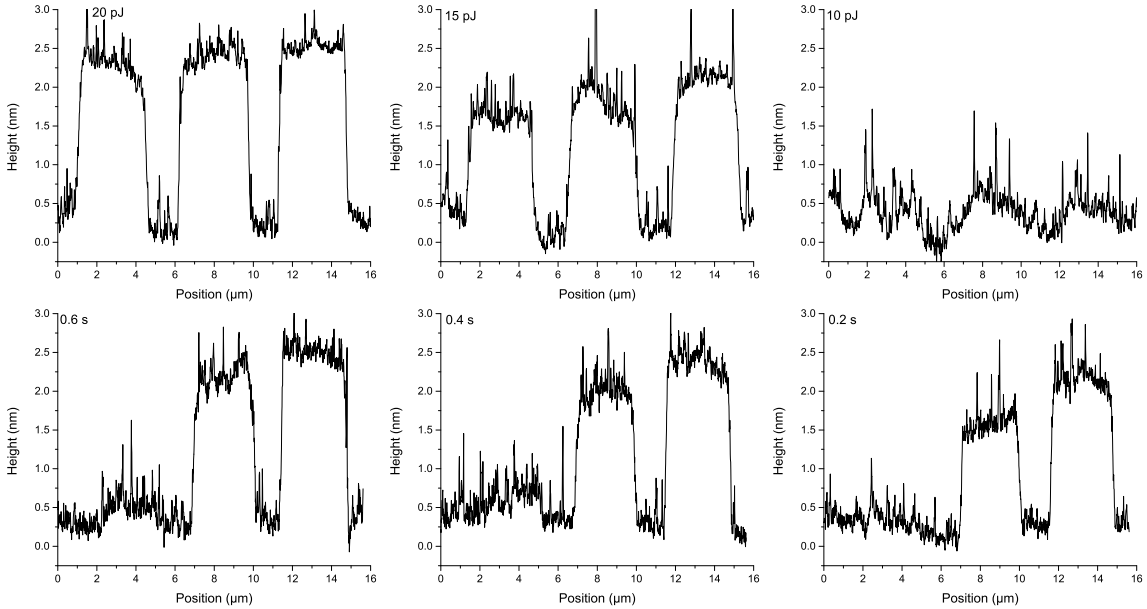

Figure 49. Cross sections of square heights of **1** B after oxidation. Top images show the different rows, whereas bottom images show the different columns.

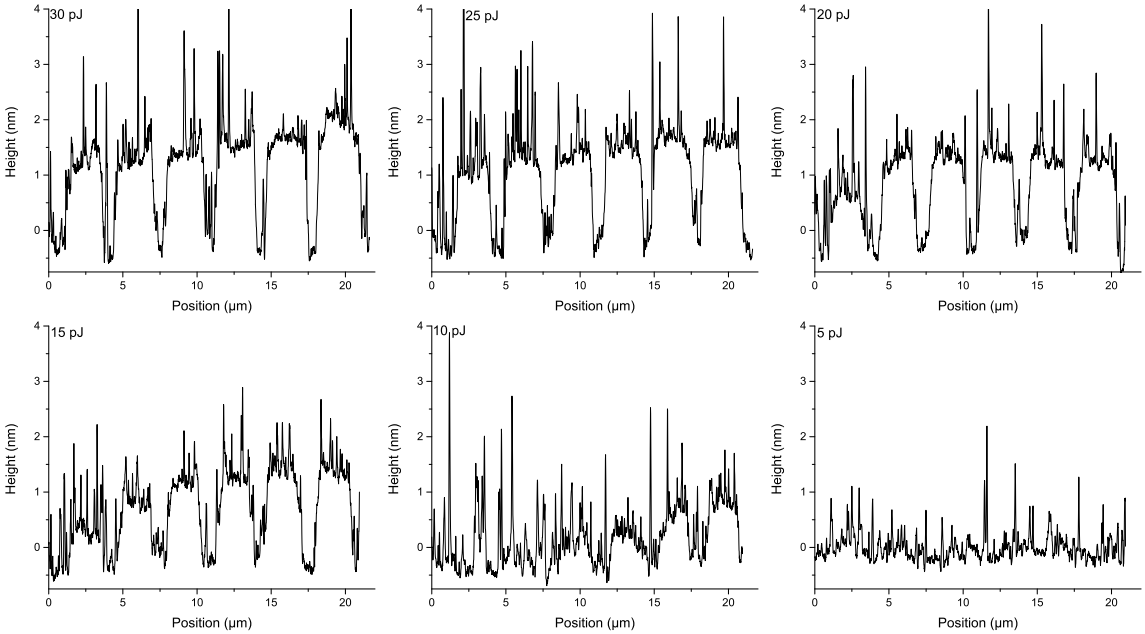

Figure 50. Cross sections of square heights of **1** F rows after oxidization.

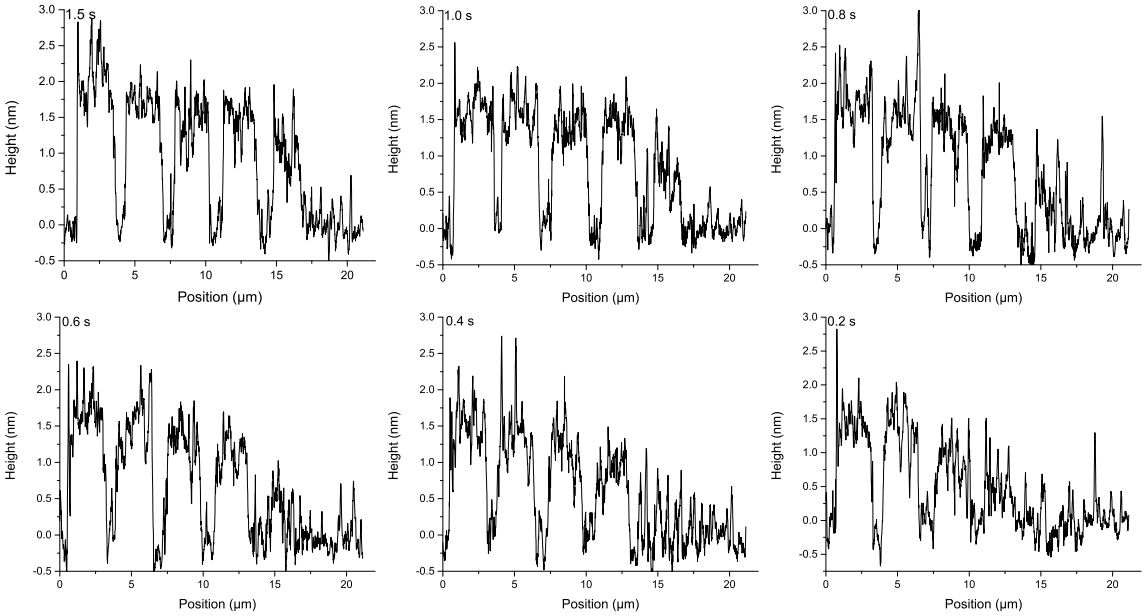

Figure 51. Cross sections of square heights of **1** F columns after oxidization.

AFM height sensor image of **1** B after protein immobilization is shown in figure 52. There are some stripes in the image that were not removable by image processing. These were most likely caused by some protein attaching to the AFM tip. The most distinct difference from before protein adhesion is the complete disappearance of some of the squares; the shapes of the remaining squares are also noticeably more irregular than before. There are some darker areas present, that appear to contain no wrinkles. Cross sections of square heights are also presented in the same figure. A cross section for the lowest row is omitted due to it containing nothing besides noise.

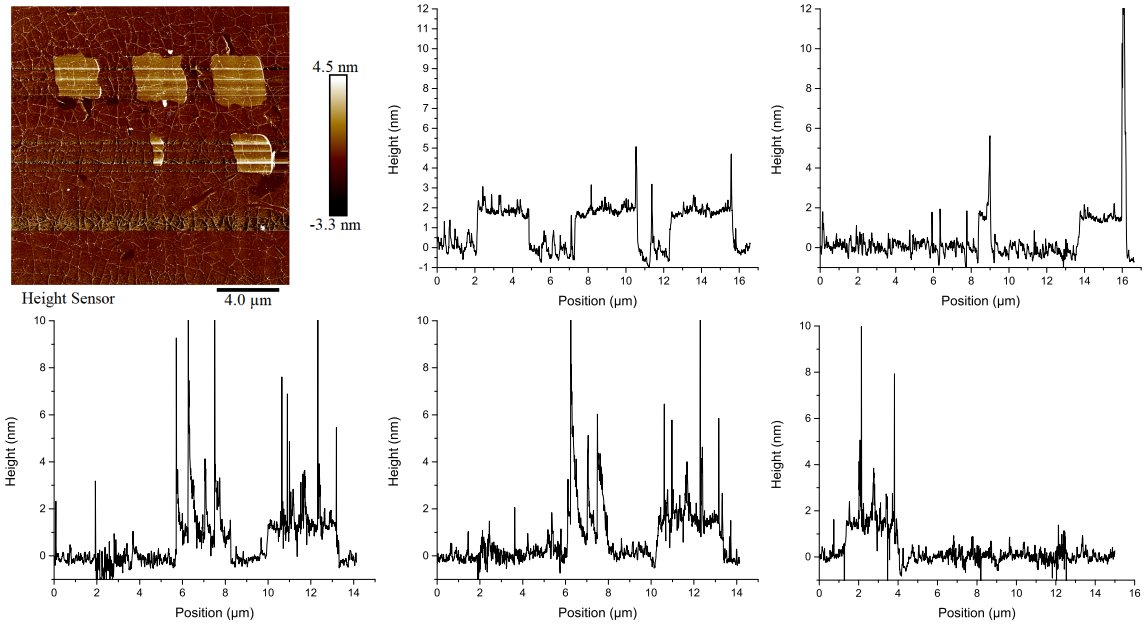

Figure 52. AFM height sensor image of **1** B after protein immobilization (top left), cross sections of its first and second row's square heights (top graphs) and cross sections of its columns (bottom).

10.3 Raman

Single Raman spectra of **1** B and F after oxidization are presented in figure 53. D, G, and 2D peaks are visible in all of them. G bands have some minor variance with changing conditions, and D bands vary significantly. On **1** F there is also significant variation in the 2D peak. The Raman maps of **2** A are presented in figure 54. The first three rows of oxidized squares are clearly visible, and the fourth slightly, in the map of integrated D band. It can also be seen that there is notable D band intensity present even on unoxidized areas, as expected of our sample. There are also some stripes visible, but these are most likely artifacs, as they disappear upon division of D map values by G map values, and plotting the resulting in $I(\mathrm{D})I(\mathrm{G})^{-1}$ map. Only the most oxidized squares are visible in the G and 2D maps, but in $I(\mathrm{D})I(\mathrm{G})^{-1}$, even the fifth row can be told apart from the background. Normalized five-point-average spectra for each square are presented in appendix 2.

Figure 55 shows Raman maps of the same area after protein coating. Map of the integrated D band has a slight resemblance to the AFM image with the top row and the rightmost square of the second row being distinguishable. The other maps do not show any clear shapes, besides the marker and being vertically striped. These stripes once again disappear upon division of D map by G map. Raman spectra of the top row squares, averaged over five points, are presented in appendix 2. Raman maps of **1** F were not measured as the graphene was peeled off.

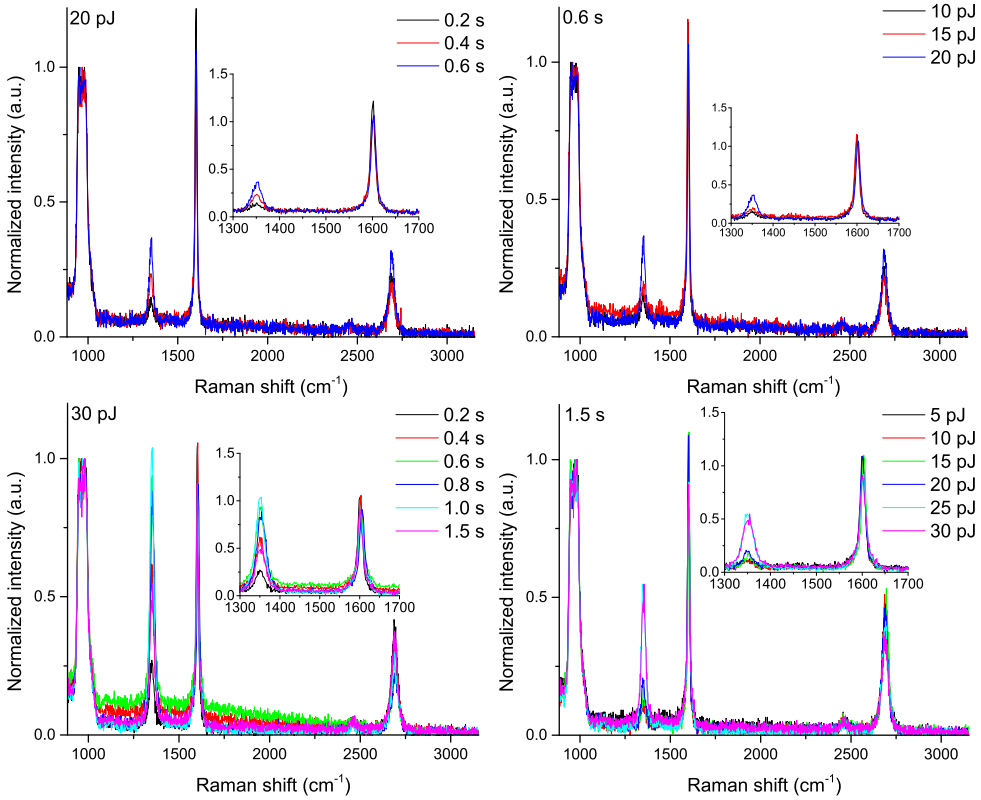

Figure 53. Single Raman spectra of **1** B (top) and **1** F (bottom) at different irradiation parameters.

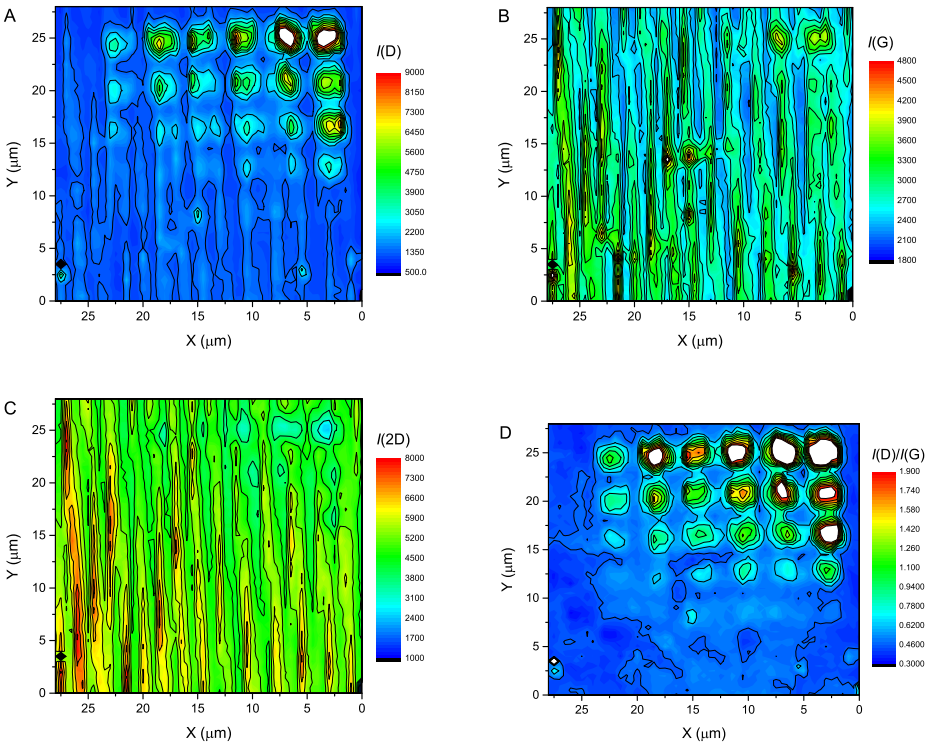

Figure 54. Raman maps of **2** A integrated over A) D, B) G and C) 2D bands, and D) D map divided by G map.

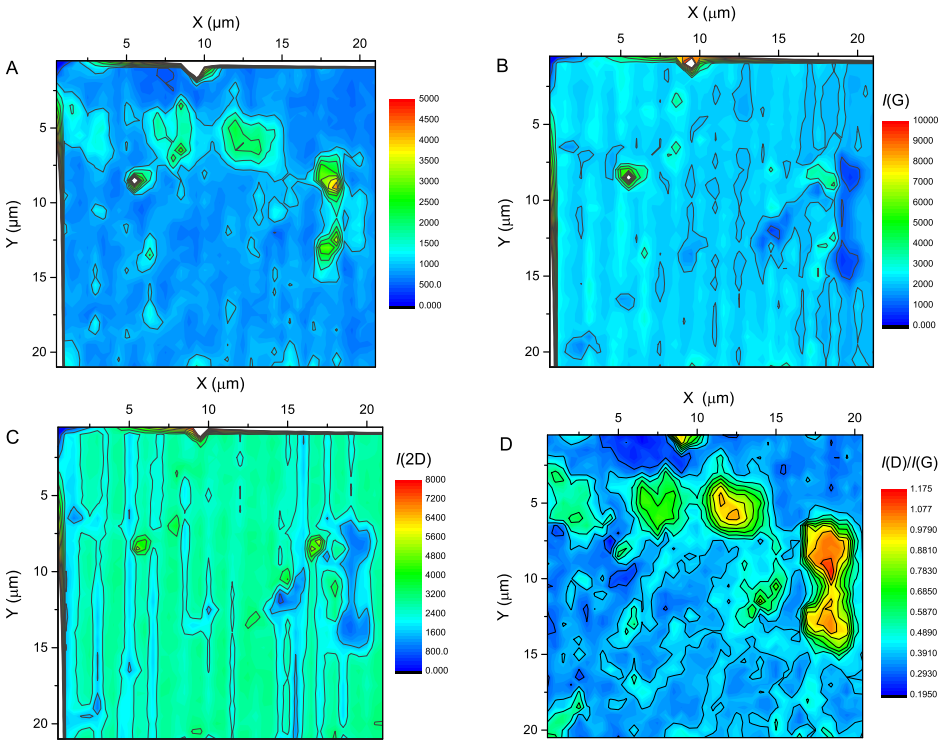

Figure 55. Raman maps of **1** B after protein immobilization integrated over A) D, B) G and C) 2D bands, and D) D map divided by G map.

10.4 State of oxidation

The state of oxidization in graphene is related to the ratio of integrated peak areas of Raman D and G bands. $I(\mathrm{D})I(\mathrm{G})^{-1}$ ratios of **1** B and F as a function of different irradiation parameters are presented in figure 56. Some linearity can be found at the less oxidized positions, but this breaks down as the irradiation times and pulse energies get larger. There seems to be no trend in how the linearity disappears, as the larger pulse energies increase the $I(\mathrm{D})I(\mathrm{G})^{-1}$ value strongly, whereas longer irradiation times result in plateauing of the ratio with an eventual decrease. These values may have some variation caused by the measurement position, and this was counteracted in later measurements by taking Raman maps of the grid areas and averaging five different spots. $I(\mathrm{D})I(\mathrm{G})^{-1}$ ratios of *2* A as a function of laser pulse energy and irradiation time are presented in figures 58 and 57. These graphs have notably more linear nature than their predecessors, implying that the disparities observed for chip **1** were a result of suboptimal measurement position. The graph with the lowest laser pulse energy in figure 57 shows significant irregularity, but this can be attributed to difficulty in finding the weakly oxidized squares amidst the wrinkly graphene. The progression of **1** B after protein coating is presented in appendix 2. The absolute values have increased a little, but no significant changes are visible.

The height of the oxidized squares as a function of $I(\mathrm{D})I(\mathrm{G})^{-1}$ is presented in figure 59. For **1** B, the increase in height appears rather linear, disregarding the single outlier of the lowest row. For **1** F on the other hand, the square heights start plateauing just before the ratio reaches unity.

This is to be expected, as the oxygen containing groups cannot just stack on top of each other. The Raman data available for **1** B is of the most oxidized squares, so the heights most likely exist at the plateauing stage of the curve. It can also be seen, that the heights of **1** B are higher than those of F, despite higher irradiation parameters and $I(\mathrm{D})I(\mathrm{G})^{-1}$ ratios being available in the latter.

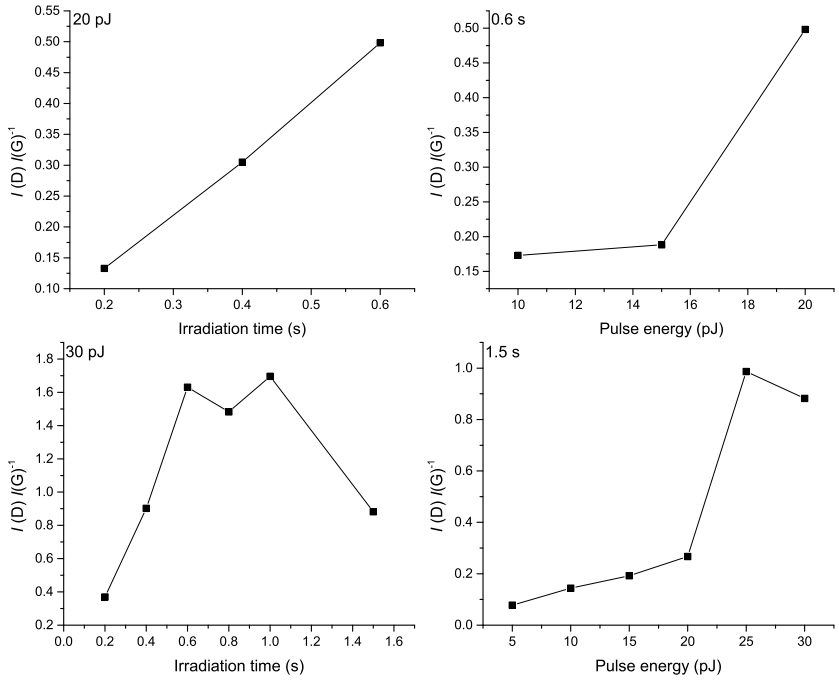

Figure 56. $I(\mathrm{D})I(\mathrm{G})^{-1}$ for **1** B (top) and **1** F (bottom) before protein functionalization as a function of different irradiation parameters.

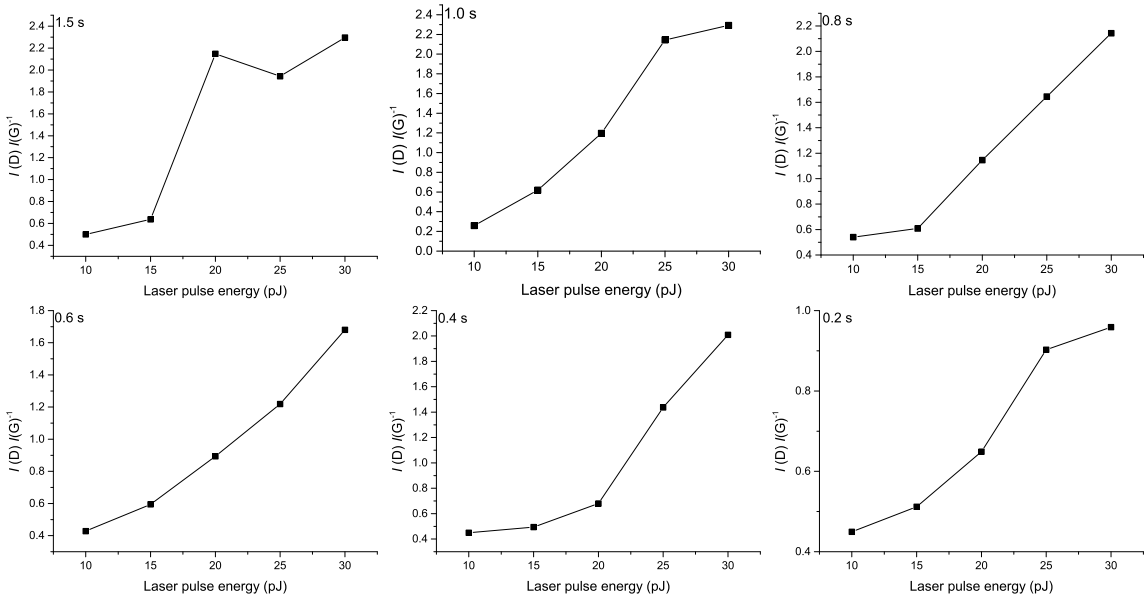

Figure 57. The progression $I(\mathrm{D})I(\mathrm{G})^{-1}$ for **2** A as a function of laser pulse energy at different irradiation times.

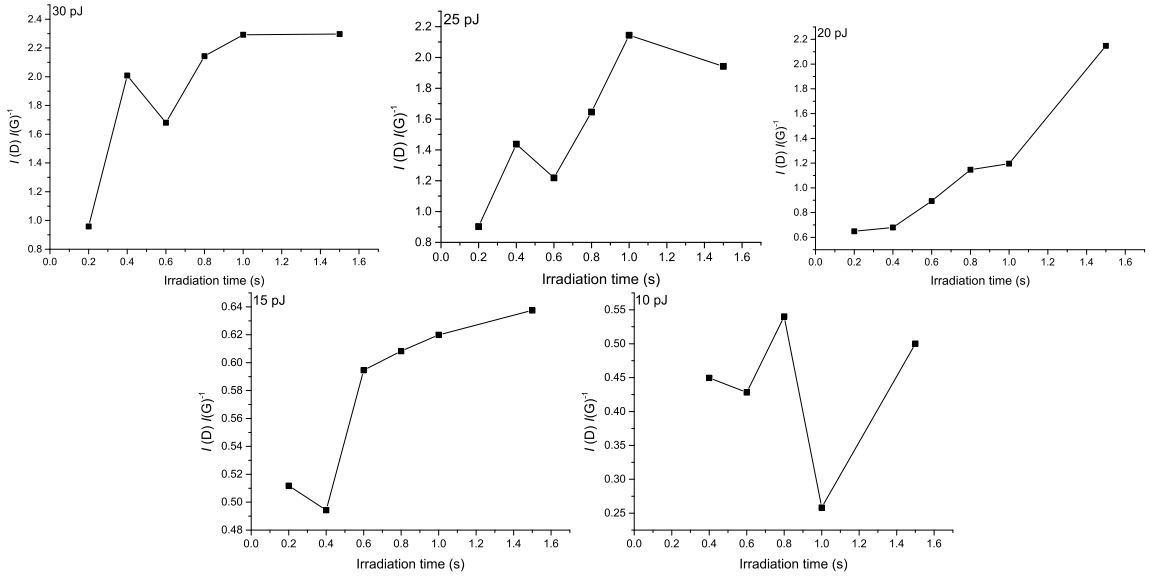

Figure 58. The progression $I(\mathrm{D})I(\mathrm{G})^{-1}$ for **2** A as a function of irradiation time at different laser pulse energies

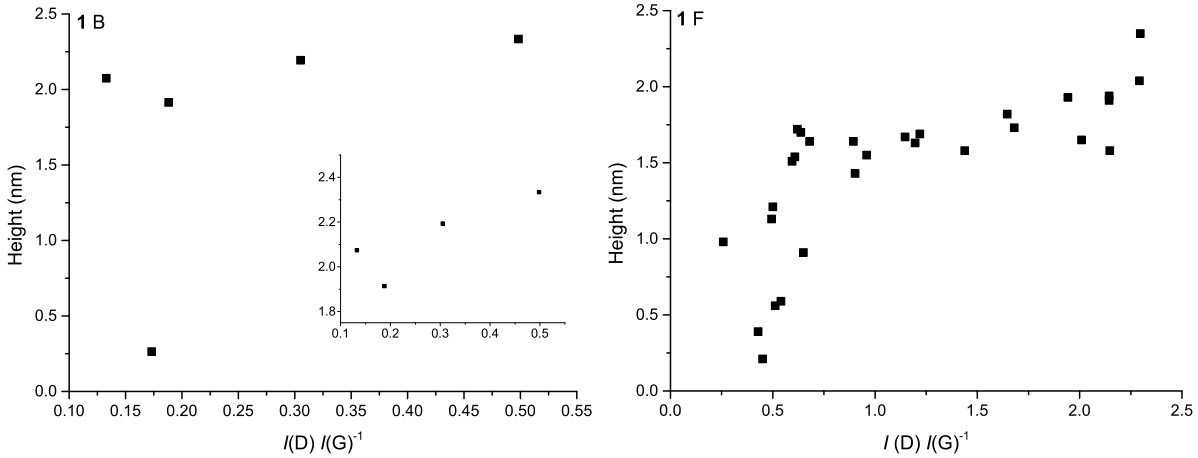

Figure 59. The heights of **1** B and **1** F as a function of $I(\mathrm{D})I(\mathrm{G})^{-1}$. $I(\mathrm{D})I(\mathrm{G})^{-1}$ of **1** F measured on **2** A. The inset is a zoomed-in portion of the same graph.

10.5 Fluorescence lifetime imaging spectroscopy

Best fits for lifetimes and corresponding amplitudes for avidin-FITC and BSA-avidin-FITC bound to certain graphene positions are presented in table 10. The lifetime of BSA-avidin-FITC was not measured due to time constraints. Fast-FLIM image of the graphene areas used for fitting are presented in appendix 3. Fitting parameters for one to four exponential components for all measurements are presented in appendix 4.

Fast-FLIM images of **1** B and **1** F before water immersion are presented in figure 60. The oxidized areas have clearly longer average lifetimes than the pristine graphene, and the average lifetime appears to increase as the level of oxidation does. There are also some clumps of longer lifetimes visible. It is also noteworthy that there is an especially large cluster of this

Table 10. Lifetimes of avidin-FITC (pH 7.4) in solution and lifetimes attached to graphene near different oxidized areas

Material	τ_1 [ns]	τ_2 [ns]	τ_1 [ns]	τ_4 [ns]	A_1 [kCnts]	A_2 [kCnts]	A_3 [kCnts]	A_4 [kCnts]	χ^2
Avidin-FITC	0.343	0.959	2.32	4.01	733	642	489	400	1.35
1 B graphene	0.117	0.270	2.36	-	91.9	6.01	0.0383	-	1.22
1 F graphene	0.167	0.462	1.46	-	97.4	25.3	0.474	-	1.26

longer lifetime component at the marker of **1** F.

Fast-FLIM images of **1** F during and after water immersion, as well as **1** B after water immersion are presented in appendix 3. **1** B was not imaged during water immersion as the oxidized squares were not visible. The water immersion image is messy, with no trace of the oxidized squares. The only visible features are the edges of the marker and another shape at the bottom of the image, used for identifying measurement positions. The image resolution does not recover completely after drying and the oxidized grid is visible only very slightly. For **1** B the grid does not become visible again, although the markers can be found. The image also appears to contain less of the longer lifetime clusters, but an area of slightly longer lifetime appears at the left hand side of the image.

Figures 61 and 62 show the FLIM images of **1** B and **1** F before and after water immersion fitted with a number of exponential components. **1** F after water immersion required three components, but the rest had the goodness of fit increased until the introduction of a fourth component. In all of the images, the shortest lifetime component appears ubiquitous. In figure 61 the longest lifetime component can only be found at the clusters, and the second shortest lifetime appears more prominent at the oxidized squares. The second longest lifetimes differ, **1** B having its behavior lean towards the longer lifetime, whereas on **1** F the behavior is more more like the shorter one. For the images after immersion, no new information is gained for **1** B. For on the

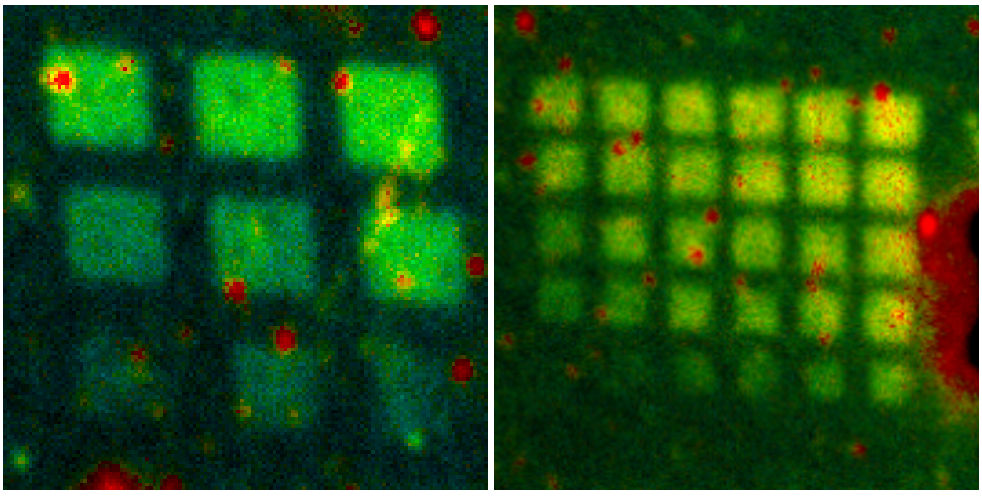

Figure 60. Fast-FLIM images of **1** B (left) and **1** F (right) before water immersion.

other hand **1** F it is found that the squares are not visible so much due to the presence of shorter lifetimes but more due to the absence of longer ones.

Fitting a single lifetime was used as an indicator of average lifetime. Single lifetimes were fitted for all squares and the resulting heatmap for chip **1** is presented in figure 63. In the heatmaps, a square corresponds to a single oxidized area. The same figure also contains the amplitudes and χ^2 values of the fits. Fits with one to four exponential components were applied, and the fitting parameters are presented in appendix 4.

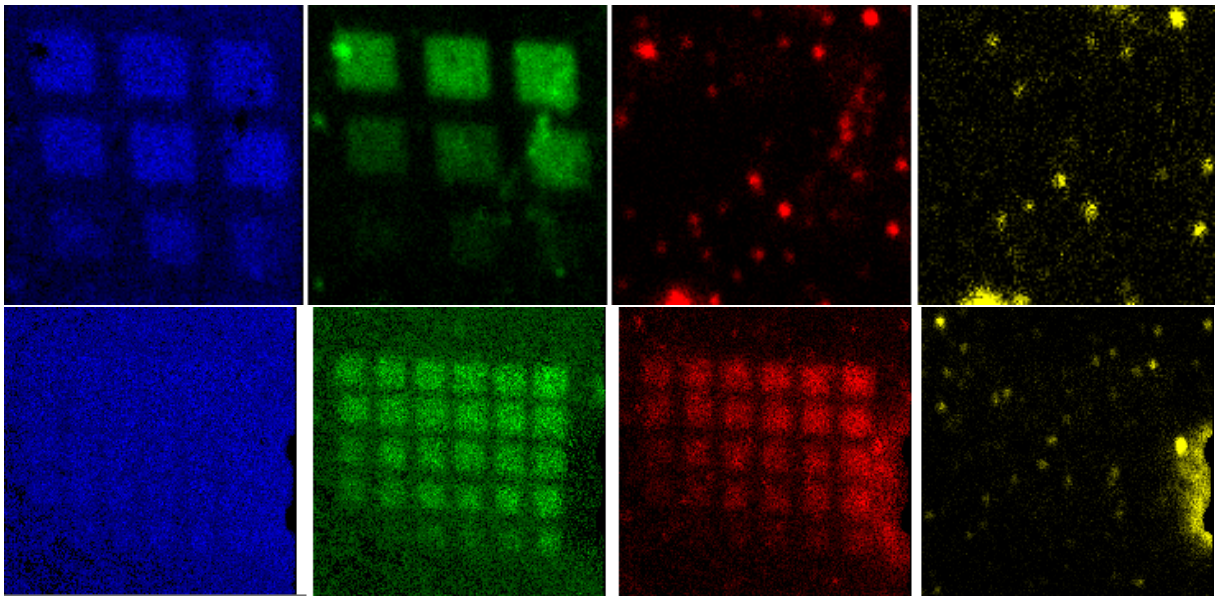

Figure 61. FLIM images of **1** B (top) **1** F (bottom) before water immersion fitted with 0.127 ns, 0.309 ns, 1.47 ns and 4.86 ns, and with 0.172 ns, 0.439 ns, 0.941 ns and 2.76 ns. The images are from left to right in the order of increasing lifetime.

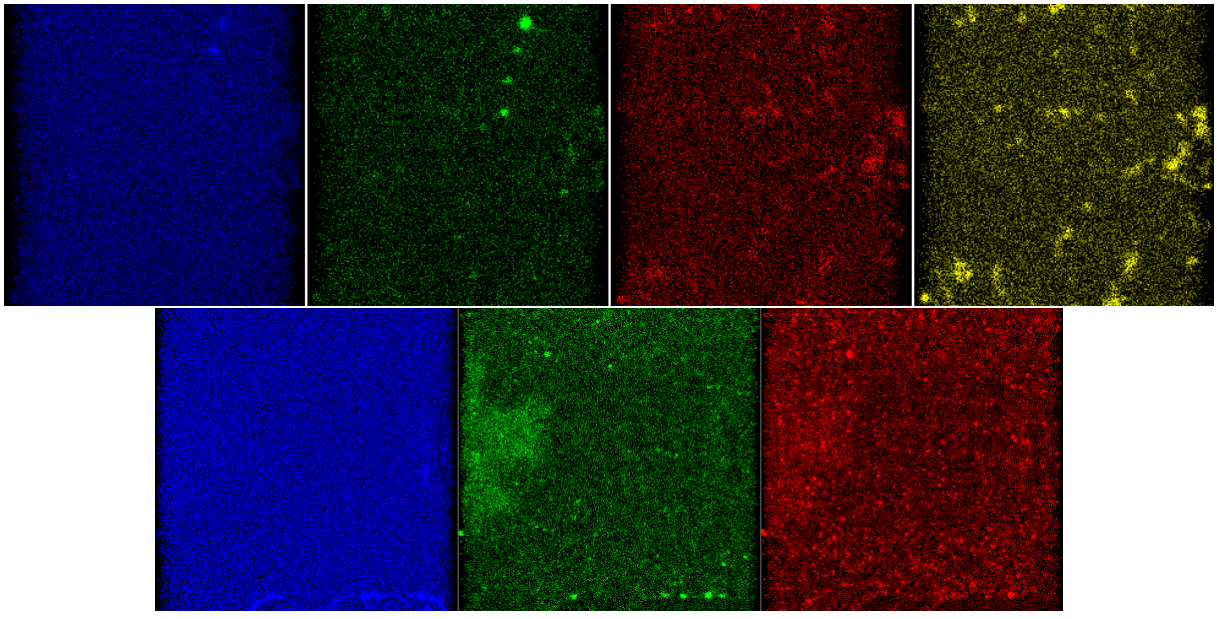

Figure 62. FLIM images of **1** B (top) and **1** F (bottom) after water immersion fitted with 0.096 ns, 0.553 ns, 1.89 ns and 4.82 ns, and with 0.137 ns, 1.197 ns and 4.21 ns. The images are from left to right in the order of increasing lifetime.

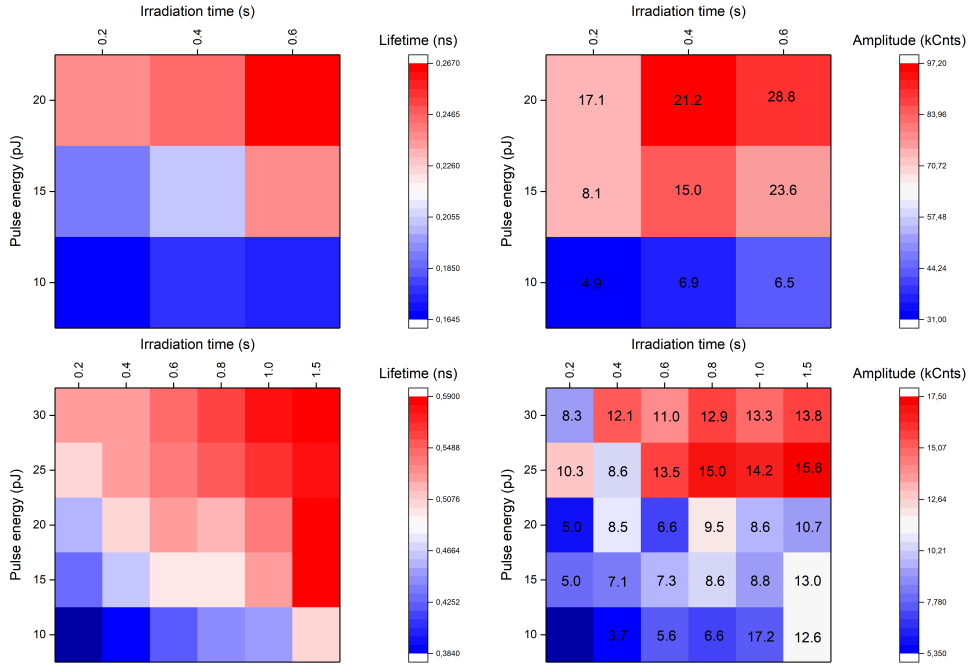

Figure 63. Heatmap of average lifetimes (left) of **1** B (top) and **1** F (bottom) and corresponding amplitudes (right). The numbers on the amplitudes indicate the χ^2 value for the square.

The apparent best fits for the squares were achieved with three exponential components. The heatmaps with three components are presented in figures 64 and 65. Heatmaps of fits with two and four components are presented in appendix 5. Shorter lifetimes are distinctly longer on the more oxidized squares, where they also appear to have larger amplitudes. The longest lifetimes show no real dependence on the state of oxidization, only some sporadic changes. The overall amplitudes lower significantly from τ_1 to τ_2 to τ_3, and differences in orders of magnitude are discernible.

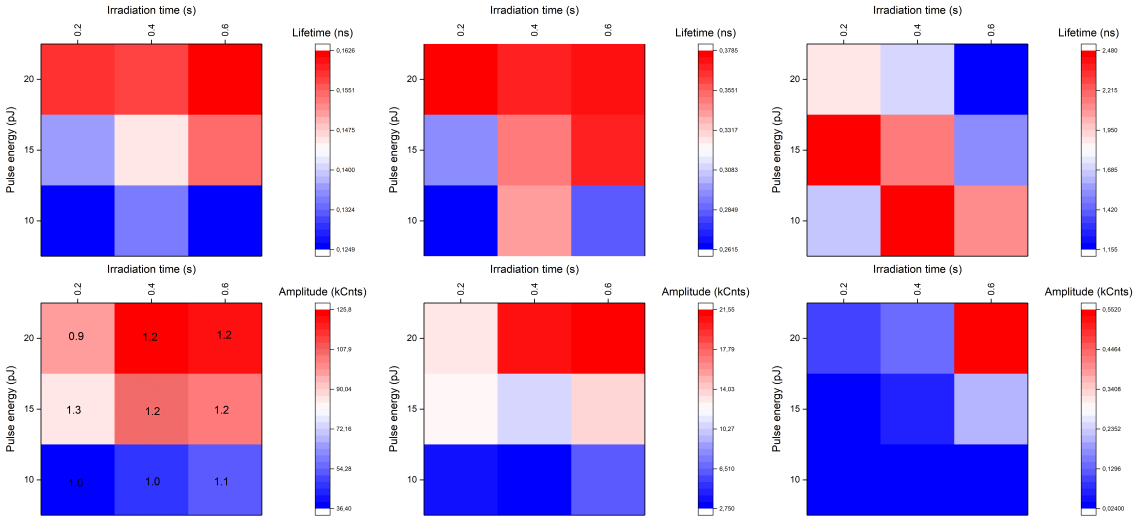

Figure 64. The lifetimes (top) and corresponding amplitudes (bottom) of **1** B fitted with three exponential components. The numbers on the amplitudes indicate the χ^2 value for the fit.

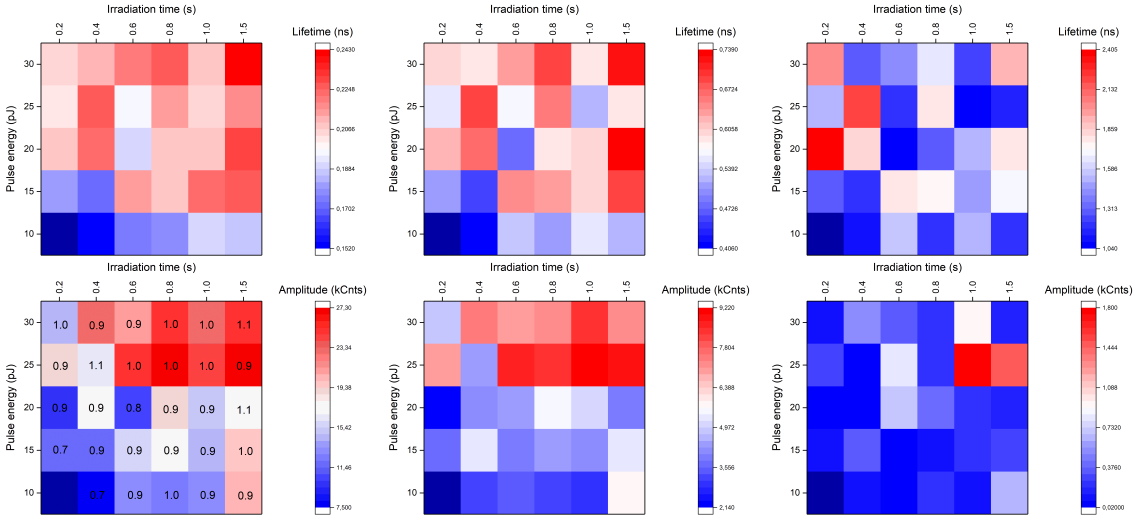

Figure 65. The lifetimes (top) and corresponding amplitudes (bottom) of **1** F fitted with three exponential components. The numbers on the amplitudes indicate the χ^2 value for the fit.

10.6 Changes in lifetime

The lifetimes of dyes are affected by their distance from the graphene surface, which in turn is affected by the state of oxidation. Average lifetime as a function of $I(\mathrm{D})I(\mathrm{G})^{-1}$ is presented in figure 66 for **1** B and figure 67 for **1** F. Resemblance of a trend can be seen, where the average lifetime increases as the state of oxidization does. The graphs formed by the most oxidized rows and columns are presented separately to clarify the origin of the points.

The large variation from the increasing trend is surprising, as the average lifetimes in figure 63 cascade rather smoothly as irradiation parameters change. Another irregularity on the data can be found between B and F: it could be expected that different areas with the same level of oxidization had the same average lifetimes. This is actually not the case here. Even though there are some points available with the same level of oxidization, the highest average lifetime achieved for **1** B is less than 0.25 ns, whereas the lowest ones for **1** F are still over 0.50 ns. Some error can be attributed to the uncertainty in determination of $I(\mathrm{D})I(\mathrm{G})^{-1}$, but other affecting parameters are most likely at play.

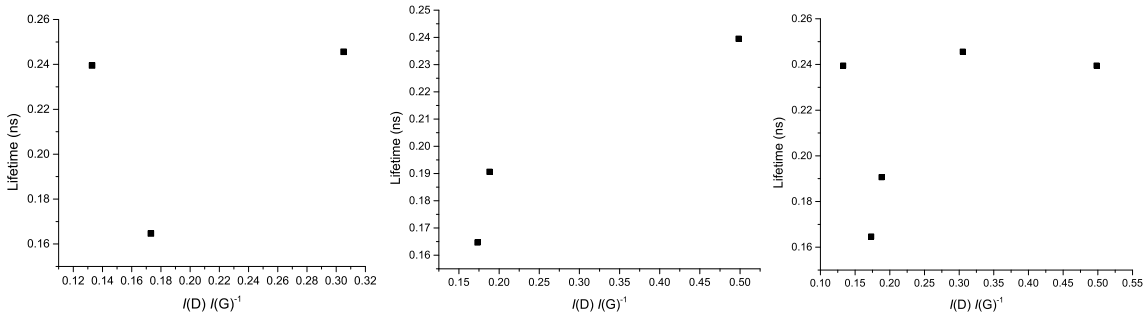

Figure 66. Average lifetime as a function of $I(\mathrm{D})I(\mathrm{G})^{-1}$ for **1** B. Graph on the left is of the 20 pJ pulse energy row, middle graph of the 0.6 s irradiation time column and the rightmost graph is a combination of the other two.

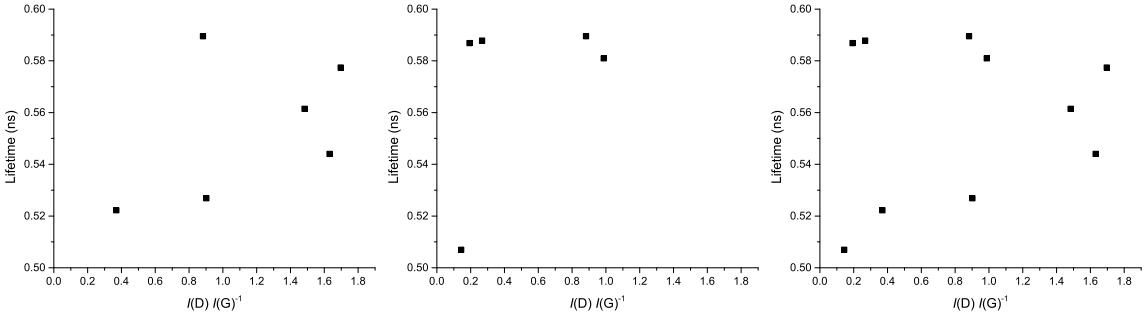

Figure 67. Average lifetime as a function of $I(\mathrm{D})I(\mathrm{G})^{-1}$ for **1** F. Graph on the left is of the 30 pJ pulse energy row, middle graph of the 1.5 s irradiation time column and the rightmost graph is a combination of the other two.

To artifcially increase the amount of $I(\mathrm{D})I(\mathrm{G})^{-1}$ values available, the lifetime data of **1** F was used together with Raman data measured from **2** A, as the irradiation parameters are identical. Average lifetime as a function of $I(\mathrm{D})I(\mathrm{G})^{-1}$ is presented in figure 68, two lifetimes in figure 69 and three lifetimes in appendix 6. It is clear that the average lifetime of the dye increases as the state of oxidation does. Another notable feature in the graph is its striking resemblance with figure 59. For fits with two exponential components, the trend remains similar, although the plateauing is a bit more pronounced. For three lifetime components, the trend starts falling apart.

Average lifetime of **1** B and F as a function of square height is presented in figure 70, where a beautiful linear pattern can be found. Linear fits of the data, with Pearson's R coefficients of 0.95 for both, can be found in appendix 7. When fitting two lifetimes, the linearly increasing behaviour remains nicely for F, albeit with a bit more dispersion. B on the other hand has its second lifetime component decreasing as the square height increases. For three lifetime components, dispersion from the linear trend further increases for F, so much that the longest component has barely any resemblance to it left. B retains the linearity of the shortest lifetime

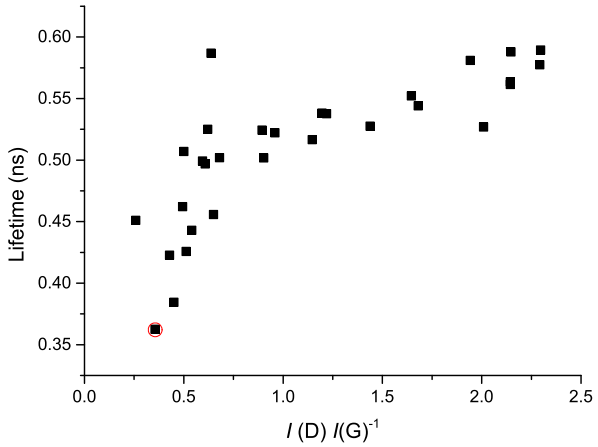

Figure 68. The average lifetime of **1** F squares as a function of $I(\mathrm{D})I(\mathrm{G})^{-1}$ measured on **2** A (identical irradiation parameters). Circled point indicates measurement on unoxidized graphene.

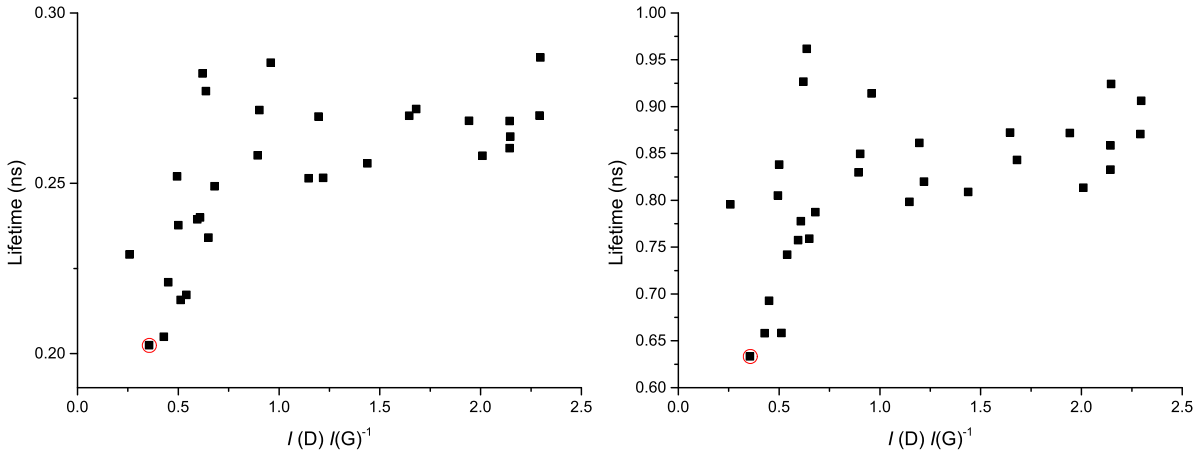

Figure 69. Two lifetimes of **1** F squares as a function of $I(\mathrm{D})I(\mathrm{G})^{-1}$ measured on **2** A (identical irradiation parameters). Circled points indicate measurement on unoxidized graphene.

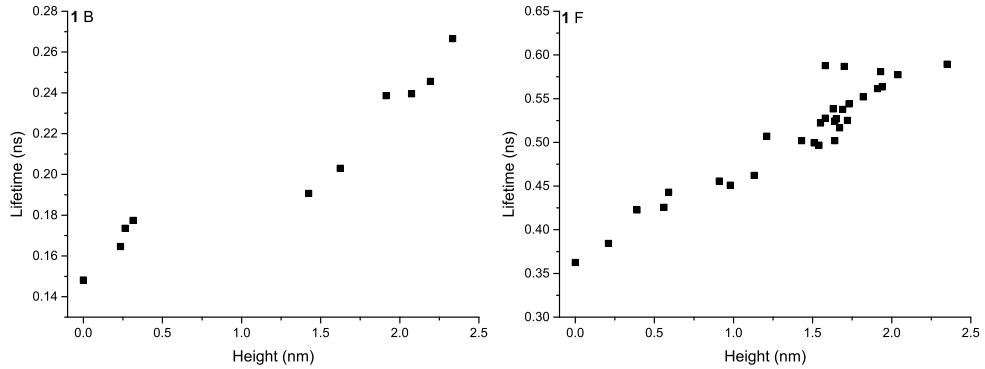

Figure 70. The average lifetime on **1** B and F as a function of square height.

component, and has the middle component also follow the trend, but the longest has again a decreasing inclination.

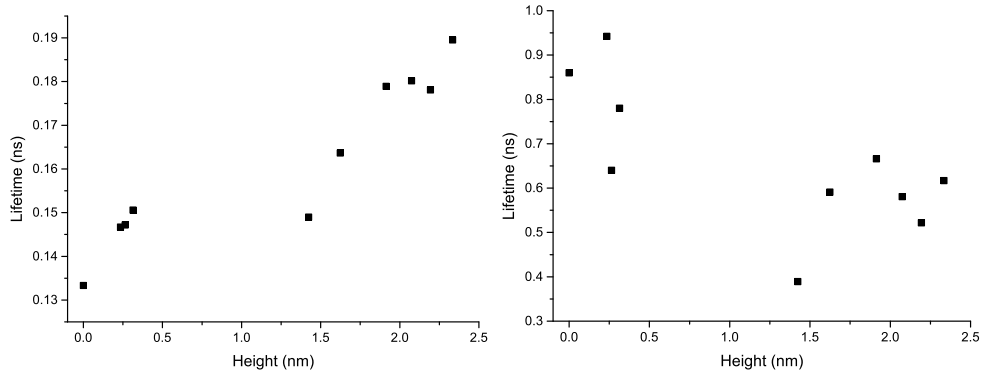

Figure 71. The lifetime on **1** B, fitted with two exponential components, as a function of square height.

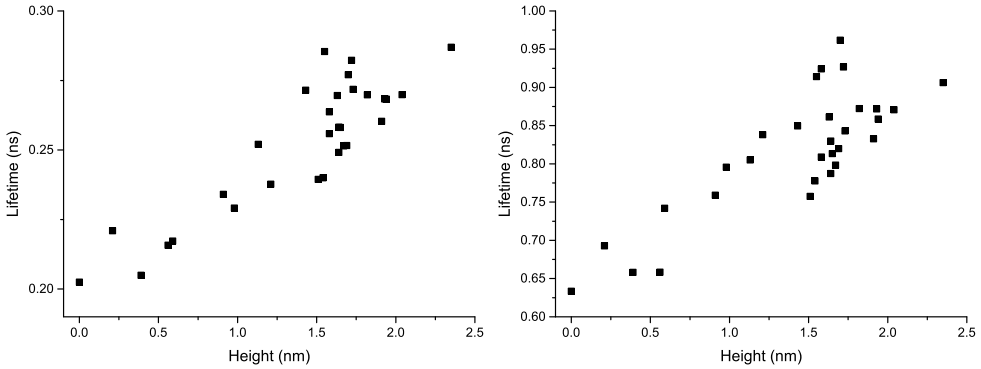

Figure 72. The lifetime on **1** F, fitted with two exponential components, as a function of square height.

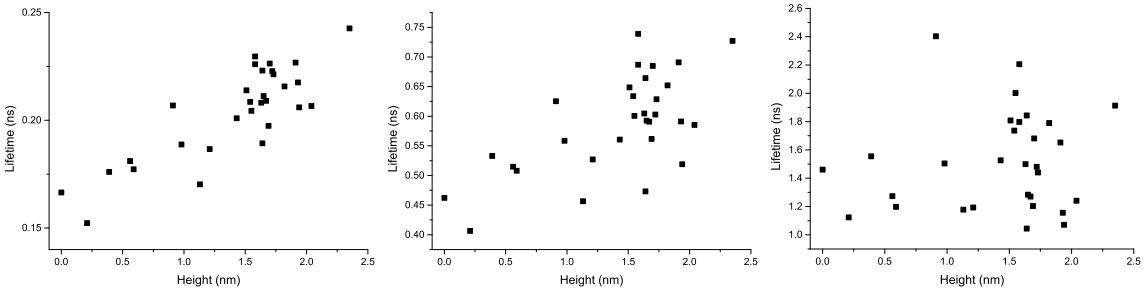

Figure 73. The lifetime on **1** F, fitted with tree exponential components, as a function of square height.

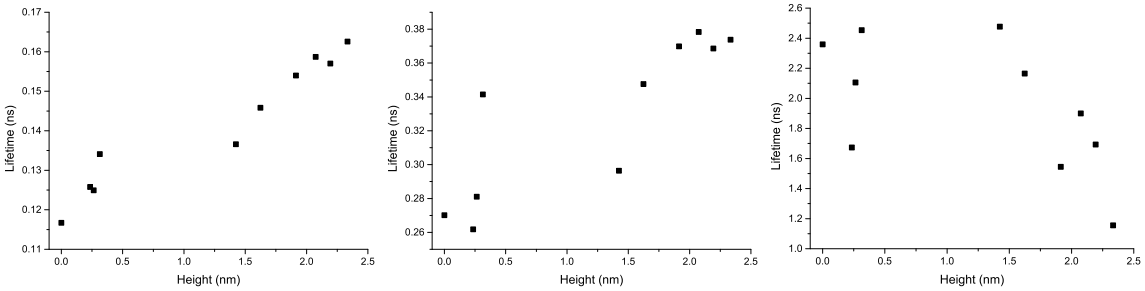

Figure 74. The lifetime on **1** B, fitted with tree exponential components, as a function of square height.

11 Discussion

The height of the oxidized squares is clearly dependent on the level of oxidation, which in turn is affected by the irradiation time and laser pulse energy. For chip **1**, the relationship between irradiation parameters is a lot more sporadic than on chip **2**. This is in part due to the smaller sample size. Averaging five points on the latter chip increases statistical accuracy and gives a better image of the whole square in comparison with a single measurement approximately in the middle of the square.

The height of the squares first increases rapidly with $I(\mathrm{D})I(\mathrm{G})^{-1}$ ratio, but then starts plateauing. Here an effect of square size is found, as the **1** B squares are clearly higher than those of **1** F, and with remarkably lower $I(\mathrm{D})I(\mathrm{G})^{-1}$ ratios. It should be noted, that gauging the height of the squares is approximate at best, due to wrinkles present on top of the squares, as well as their overall irregular shapes.

Average lifetime of the dye is found to follow a very similar trend as square height as a function of $I(\mathrm{D})I(\mathrm{G})^{-1}$. The most interesting result is the linear relationship between the fluorescence lifetime and the square height, that extends all the way to the zero height at the graphene surface. This could imply that parameters such as surface roughness and hydrophobicity do not affect the lifetime in quantifiable amounts. This is with the assumption that these properties change as the level of oxidation progresses, like the increasing amount and changing ratios between different types of oxygen including groups should. This is rather unexpected, as graphene should quench the fluorescence of dyes as a function of reciprocal of the fourth power of distance (or as a function of exp[-r] if plasmons are present). There is also the difference of the absolute lifetime values between the two sites: the longest lifetimes on **1** B are shorter than the shortest ones on **1** F, despite the height ranges being similar. The slopes of the fits are also clearly different. This could be an effect of the square area.

Increasing the amount of lifetime components of the fits to two retains the increasing linearity in the relationship on **1** F, but for **1** B the longer component is actually decreasing as a function of height. Addition of a third lifetime component increases the spread on **1** F so much, that the longest one appears to be mere filler to the fit, and as such no more than two major components that increase linearly with the square height can be identified. This is with the notion, that there exist most likely a distribution of different lifetimes at slightly varying orientations and distances from quenchers. Addition of the second lifetime component to the fit of **1** B has a bit different outcome, as the longer component is actually decreasing with increasing square height. Addition of a third component shifts this decreasing character again to the longest lifetime. The irregularity on could be explained by the amount of deposits visible in figure 60: majority area of the lowest squares' areas is covered by these longer lifetime clusters, which may have disrupted the extraction of a "pure" lifetime.

Most lifetimes presented in table 9 are distinctly larger than the ones attained here. Only ones that come close are the results by Handschuh-Wang *et al.*,[78] although they had longer lifetime components present, which are not observable here. However, even their results are closer to the lifetimes attained for avidin-FITC (table 10). The shortest lifetimes measured could be due to fluorescence of the oxidized graphene, as the values measured for GO are in the same magnitude order (section 8.8).

Analyzing the fitting parameters (appendix 4) shows that the χ^2 values of **1** F fits with two lifetimes are much better than the values for **1** B. For three exponential components, the χ^2 values of B close nicely on one, but the values of F are getting so small that it is starting to resemble overfitting. On the three-component fits, the amplitudes of the shortest lifetimes on F are routinely 4–5 times larger than the middle ones', and the difference between the middle and the longest lifetime is an order of magnitude. For **1** B, the differences are an order of magnitude and two orders of magnitude, respectively. The massively larger variation in amplitudes, combined with larger χ^2 values indicates that there are more lifetime components present on the larger B squares than on the smaller ones on F. Operative parameters causing the difference may be the roughness of the surface, or simply the lesser amount of square edge per area unit. These may induce different binding between BSA and the graphene, affecting the position of avidin-FITC, which changes the distance between the dye molecules and the graphene surface.

11.1 Damage to the first chip

Chip **1** was damaged sometime after the first FLIM measurement, as evident from the optical microscope and AFM images (figures 47 and 52). In the FLIM image of **1** F during water immersion it is clear that the water disrupts imaging in some way. Even the best fit with three components has a χ^2 value of of over 23, which is not even close to being reliable. There is also the fact that nothing worth imaging was found from **1** B during water immersion. However, as the **1** F oxidized grid can faintly be found from the FLIM image after immersion, it must be deduced that the large area exfoliation of graphene is not due to the contact with water. Looking at the optical microscopy images again, some of the damage appears rather linear. A more likely explanation for the peeling would me mishandling of the sample; the chip may have been scratched against a sample holder, for example.

If the blurriness of the FLIM images during and after water immersion is not due to damage to the sample, it could be caused by some of the dye and/or dye-protein conjugate separating from the surface. The fluorescence from the solution can cover the fluorescence from the molecules below, critically lowering imaging resolution. A similar phenomenon has been found by Togashi and Ryder,[71] who imaged BSA labeled with dye molecules attached to surfaces. They found that removal of a bulk solution from the top of the imaged surface improved their results, as the bulk solution shadowed the already low intensity of the attached BSA conjugates. These

results indicate that further measurements should not be conducted in water immersion.

Another unexpected change in the chip topography on **1** B is the disappearance of the least oxidized squares. The remaining squares are also distinctly deformed, losing their sharp edges and corners. The middle square is missing its right half and lastly, the graphene appears missing at certain positions. The stripe artifacts are most likely due to some of the protein attaching to the AFM tip. Some irregularity on the squares could be explained by protein adhesion, as BSA should be visible on the images. The changes are, however, in larger scale. The completely, and partly, missing squares support a notation that the squares are damaged.

A most interesting result can be found at the positions of the missing squares. The graphene at the positions appears undamaged, and even the typical wrinkles are present. Johansson *et al.*[77] have suggested that the graphene network remains intact after two-photon oxidation, and this finding appears to support the claim. Whatever the method of peeling, a kind of "molecular tape" could have been discovered here.

12 Conclusions

The effect of two-photon oxidized graphene on the fluorescence of avidin-FITC attached to the graphene *via* b-BSA was studied by AFM, Raman and FLIM. The effect of oxidation on graphene can be seen on the Raman and AFM measurements. The $I(\mathrm{D})I(\mathrm{G})^{-1}$ ratio is found to increase with increasing irradiation parameters (irradiation time and laser pulse energy). As $I(\mathrm{D})I(\mathrm{G})^{-1}$ increases, so does the height of the oxidized squares. It is noted that the size of the irradiated area appears to affect the effect irradiation has on graphene. Average lifetime of the dye molecule is found to linearly increase as a function of oxidized square height. Pearson's R values for linear fits were 0.95 for both grids. The fits of **1** B and F have widely different values for interception and slope, indicating that the square area also affects the behavior.

Due to the many possible distances from dye molecules to other dye molecules and graphene, there are naturally many other lifetimes. Fitting two and three exponential components has the linear nature degrade, and especially three lifetime component fits show signs of overfitting. This is not to say that there are barely two components, only that the amplitudes of the others are too small to fit unequivocally. The designated lifetimes are distinctly lower than those found in literature for BSA-FITC complex in different microenvironments. Fluorescence of the oxidized graphene could also play a part in the lowest lifetime components, but the fluorescence of the uncoated graphene was not studied here.

The measurement setup places many variables to the lifetime data: how BSA binds to the surface is not known; the amount of biotin per BSA varies; avidin may bind to up to four biotins; the amount of FITC per avidin varies; and the effect of graphene and its oxide on the fluorescence of FITC is not intimately understood. It is still appears that the square height and area directly affect the quenching efficiency of the oxide, whereas $I(\mathrm{D})I(\mathrm{G})^{-1}$ ratio affects it indirectly.

13 References

1. Novoselov, K. S.; Geim, A. K.; Morozov, S. V.; Jiang, D.; Zhang, Y.; Dubonos, S. V.; Grigorieva, I. V.; Firsov, A. A., Electric Field Effect in Atomically Thin Carbon Films. *Science*, **2004**, *306*, 666–669.
2. Kireev, D.; Offenhäusser, A., Graphene & two-dimensional devices for bioelectronics and neuroprosthetics. *2D Materials*, **2018**, *5*, 042004.
3. Stine, R.; Robinson, J. T.; Sheehan, P. E.; Tamanaha, C. R., Real-Time DNA Detection Using Reduced Graphene Oxide Field Effect Transistors. *Advanced Materials*, **2010**, *22*, 5297–5300.
4. Spira, M. E.; Hai, A., Multi-electrode array technologies for neuroscience and cardiology. *Nature Nanotechnology*, **2013**, *8*, 83–94.
5. Masvidal-Codina, E. et al., High-resolution mapping of infraslow cortical brain activity enabled by graphene microtransistors. *Nature Materials*, **2019**, *18*, 280–288.
6. Sharon, M., *Graphene : an introduction to the fundamentals and industrial applications*, Advanced materials series; Scrivener Publishing, Hoboken, New Jersey ; Salem, Massachusetts, 2015.
7. Meyer, J. C.; Geim, A. K.; Katsnelson, M. I.; Novoselov, K. S.; Booth, T. J.; Roth, S., The structure of suspended graphene sheets. *Nature*, **2007**, *446*, 60.
8. Yazyev, O. V.; Louie, S. G., Topological defects in graphene: Dislocations and grain boundaries. *Phys. Rev. B*, **2010**, *81*, 195420.
9. Banhart, F.; Kotakoski, J.; Krasheninnikov, A. V., Structural Defects in Graphene. *ACS Nano*, **2011**, *5*, PMID: 21090760, 26–41.
10. Robinson, J. T.; Perkins, F. K.; Snow, E. S.; Wei, Z.; Sheehan, P. E., Reduced Graphene Oxide Molecular Sensors. *Nano Letters*, **2008**, *8*, PMID: 18763832, 3137–3140.
11. Kwon, O. S.; Park, S. J.; Hong, J.-Y.; Han, A.-R.; Lee, J. S.; Lee, J. S.; Oh, J. H.; Jang, J., Flexible FET-Type VEGF Aptasensor Based on Nitrogen-Doped Graphene Converted from Conducting Polymer. *ACS Nano*, **2012**, *6*, PMID: 22224587, 1486–1493.
12. Lee, C.; Wei, X.; Kysar, J. W.; Hone, J., Measurement of the elastic properties and intrinsic strength of monolayer graphene. *Science (New York, N.Y.)* **2008**, *321*, 385–8.
13. *Young's Modulus - Tensile and Yield Strength for common Materials*, (accessed 10/18/2019).
14. *The Nobel Prize in Physics 2010 - Advanced information*, (accessed 10/18/2019).
15. Morozov, S. V.; Novoselov, K. S.; Katsnelson, M. I.; Schedin, F.; Elias, D. C.; Jaszczak, J. A.; Geim, A. K., Giant Intrinsic Carrier Mobilities in Graphene and Its Bilayer. **2007**, DOI: 10.1103/PhysRevLett.100.016602.
16. *Electrical properties of Silicon (Si)*, (accessed 10/18/2019).
17. Castro Neto, A. H.; Guinea, F.; Peres, N. M. R.; Novoselov, K. S.; Geim, A. K., The electronic properties of graphene. *Rev. Mod. Phys.* **2009**, *81*, 109–162.

18. Katsnelson, M. I.; Novoselov, K. S.; Geim, A. K., Chiral tunnelling and the Klein paradox in graphene. *Nature Physics*, **2006**, *2*, 620–625.
19. Liu, H.; Liu, Y.; Zhu, D., Chemical doping of graphene. *J. Mater. Chem.* **2011**, *21*, 3335–3345.
20. Schwierz, F., Graphene transistors. *Nature Nanotechnology*, **2010**, *5*, 487–496.
21. Riordan, M.; Hoddeson, L.; Herring, C., The invention of the transistor. *Rev. Mod. Phys.* **1999**, *71*, S336–S345.
22. *Nobel Prize in Physics 1956 - Presentation Speech*, (accessed 06/11/2019).
23. Storey, N., *Electronics : A Systems Approach.* Pearson, 2017; Vol. Sixth edition.
24. Ng, K. K., *Complete guide to semiconductor devices*, IEEE Press, 2002, ss. 740.
25. Kireev, D.; Brambach, M.; Seyock, S.; Maybeck, V.; Fu, W.; Wolfrum, B.; Offenhäusser, A., Graphene transistors for interfacing with cells: towards a deeper understanding of liquid gating and sensitivity. *Scientific Reports*, **2017**, *7*, 6658.
26. Meric, I.; Han, M. Y.; Young, A. F.; Ozyilmaz, B.; Kim, P.; Shepard, K. L., Current saturation in zero-bandgap, top-gated graphene field-effect transistors. *Nature Nanotechnology*, **2008**, *3*, 654–659.
27. Das, A.; Pisana, S.; Chakraborty, B.; Piscanec, S.; Saha, S. K.; Waghmare, U. V.; Novoselov, K. S.; Krishnamurthy, H. R.; Geim, A. K.; Ferrari, A. C.; Sood, A. K., Monitoring dopants by Raman scattering in an electrochemically top-gated graphene transistor. *Nature Nanotechnology*, **2008**, *3*, 210–215.
28. Hess, L. H.; Seifert, M.; Garrido, J. A., Graphene Transistors for Bioelectronics. *Proceedings of the IEEE*, **2013**, *101*, 1780–1792.
29. Xia, J.; Chen, F.; Li, J.; Tao, N., Measurement of the quantum capacitance of graphene. *Nature Nanotechnology*, **2009**, *4*, 505–509.
30. Lin, Y.-M.; Dimitrakopoulos, C.; Jenkins, K. A.; Farmer, D. B.; Chiu, H.-Y.; Grill, A.; Avouris, P., 100-GHz Transistors from Wafer-Scale Epitaxial Graphene. *Science*, **2010**, *327*, 662–662.
31. Hess, L. H.; Hauf, M. V.; Seifert, M.; Speck, F.; Seyller, T.; Stutzmann, M.; Sharp, I. D.; Garrido, J. A., High-transconductance graphene solution-gated field effect transistors. *Applied Physics Letters*, **2011**, *99*, 033503.
32. Dankerl, M.; Hauf, M. V.; Lippert, A.; Hess, L. H.; Birner, S.; Sharp, I. D.; Mahmood, A.; Mallet, P.; Veuillen, J.-Y.; Stutzmann, M.; Garrido, J. A., Graphene Solution-Gated Field-Effect Transistor Array for Sensing Applications. *Advanced Functional Materials*, **2010**, *20*, 3117–3124.
33. Chen, F.; Qing, Q.; Xia, J.; Li, J.; Tao, N., Electrochemical Gate-Controlled Charge Transport in Graphene in Ionic Liquid and Aqueous Solution. *Journal of the American Chemical Society*, **2009**, *131*, PMID: 19572712, 9908–9909.

34. Cheng, Z.; Li, Q.; Li, Z.; Zhou, Q.; Fang, Y., Suspended Graphene Sensors with Improved Signal and Reduced Noise. *Nano Letters*, **2010**, *10*, PMID: 20373779, 1864–1868.
35. Schedin, F.; Geim, A. K.; Morozov, S. V.; Hill, E. W.; Blake, P.; Katsnelson, M. I.; Novoselov, K. S., Detection of individual gas molecules adsorbed on graphene. *Nature Materials*, **2007**, *6*, 652–655.
36. Cheng, J.; Wu, L.; Du, X.; Jin, Q.; Zhao, J.; Xu, Y., Flexible Solution-Gated Graphene Field Effect Transistor for Electrophysiological Recording. *Journal of Microelectromechanical Systems*, **2014**, *23*, 1311–1317.
37. A miniature microelectrode array to monitor the bioelectric activity of cultured cells. *Experimental Cell Research*, **1972**, *74*, 61–66.
38. Gross, G. W.; Williams, A. N.; Lucas, J. H., Recording of spontaneous activity with photoetched microelectrode surfaces from mouse spinal neurons in culture. *Journal of Neuroscience Methods*, **1982**, *5*, 13–22.
39. Du, X.; Wu, L.; Cheng, J.; Huang, S.; Cai, Q.; Jin, Q.; Zhao, J., Graphene microelectrode arrays for neural activity detection. *Journal of biological physics*, **2015**, *41*, 339–47.
40. Ohno, Y.; Maehashi, K.; Yamashiro, Y.; Matsumoto, K., Electrolyte-Gated Graphene Field-Effect Transistors for Detecting pH and Protein Adsorption. *Nano Letters*, **2009**, *9*, PMID: 19637913, 3318–3322.
41. Guo, S.-R.; Lin, J.; Penchev, M.; Yengel, E.; Ghazinejad, M.; Ozkan, C.; Ozkan, M., Label Free DNA Detection Using Large Area Graphene Based Field Effect Transistor Biosensors. *Journal of Nanoscience and Nanotechnology*, **2011**, *11*, 5258–5263.
42. Hwang, M. T.; Wang, Z.; Ping, J.; Ban, D. K.; Shiah, Z. C.; Antonschmidt, L.; Lee, J.; Liu, Y.; Karkisaval, A. G.; Johnson, A. T. C.; Fan, C.; Glinsky, G.; Lal, R., DNA Nanotweezers and Graphene Transistor Enable Label-Free Genotyping. *Advanced Materials*, **2018**, *30*, 1802440.
43. Ang, P. K.; Chen, W.; Wee, A. T. S.; Loh, K. P., Solution-Gated Epitaxial Graphene as pH Sensor. *Journal of the American Chemical Society*, **2008**, *130*, PMID: 18850701, 14392–14393.
44. Park, S. J.; Kwon, O. S.; Lee, S. H.; Song, H. S.; Park, T. H.; Jang, J., Ultrasensitive Flexible Graphene Based Field-Effect Transistor (FET)-Type Bioelectronic Nose. *Nano Letters*, **2012**, *12*, PMID: 22962838, 5082–5090.
45. Zhang, M.; Liao, C.; Mak, C. H.; You, P.; Mak, C. L.; Yan, F., Highly sensitive glucose sensors based on enzyme-modified whole-graphene solution-gated transistors. *Scientific Reports*, **2015**, *5*, 8311.
46. Vasu, K.; Sridevi, S.; Sampath, S.; Sood, A., Non-enzymatic electronic detection of glucose using aminophenylboronic acid functionalized reduced graphene oxide. *Sensors and Actuators B: Chemical*, **2015**, *221*, 1209–1214.

47. Huang, Y.; Dong, X.; Shi, Y.; Li, C. M.; Li, L.-J.; Chen, P., Nanoelectronic biosensors based on CVD grown graphene. *Nanoscale*, **2010**, *2*, 1485–1488.
48. Kwak, Y. H.; Choi, D. S.; Kim, Y. N.; Kim, H.; Yoon, D. H.; Ahn, S.-S.; Yang, J.-W.; Yang, W. S.; Seo, S., Flexible glucose sensor using CVD-grown graphene-based field effect transistor. *Biosensors and Bioelectronics*, **2012**, *37*, 82–87.
49. You, X.; Pak, J. J., Graphene-based field effect transistor enzymatic glucose biosensor using silk protein for enzyme immobilization and device substrate. *Sensors and Actuators B: Chemical*, **2014**, *202*, 1357–1365.
50. Dong, X.; Shi, Y.; Huang, W.; Chen, P.; Li, L.-J., Electrical Detection of DNA Hybridization with Single-Base Specificity Using Transistors Based on CVD-Grown Graphene Sheets. *Advanced Materials*, **2010**, *22*, 1649–1653.
51. Li, S.; Huang, K.; Fan, Q.; Yang, S.; Shen, T.; Mei, T.; Wang, J.; Wang, X.; Chang, G.; Li, J., Highly sensitive solution-gated graphene transistors for label-free DNA detection. *Biosensors and Bioelectronics*, **2019**, *136*, 91–96.
52. Hwang, M. T.; Landon, P. B.; Lee, J.; Choi, D.; Mo, A. H.; Glinsky, G.; Lal, R., Highly specific SNP detection using 2D graphene electronics and DNA strand displacement. *Proceedings of the National Academy of Sciences of the United States of America*, **2016**, *113*, 7088–93.
53. Willner, I.; Zayats, M., Electronic Aptamer-Based Sensors. *Angewandte Chemie International Edition*, **2007**, *46*, 6408–6418.
54. Ohno, Y.; Maehashi, K.; Matsumoto, K., Label-Free Biosensors Based on Aptamer-Modified Graphene Field-Effect Transistors. *Journal of the American Chemical Society*, **2010**, *132*, PMID: 21128665, 18012–18013.
55. *Molecular cell biology*, 5th ed, Lodish, H., Ed.; W. H. Freeman, Company, New York, 2003.
56. Sohn, I.-Y.; Kim, D.-J.; Jung, J.-H.; Yoon, O. J.; Thanh, T. N.; Quang, T. T.; Lee, N.-E., pH sensing characteristics and biosensing application of solution-gated reduced graphene oxide field-effect transistors. *Biosensors and Bioelectronics*, **2013**, *45*, 70–76.
57. Hess, L. H.; Lyuleeva, A.; Blaschke, B. M.; Sachsenhauser, M.; Seifert, M.; Garrido, J. A.; Deubel, F., Graphene Transistors with Multifunctional Polymer Brushes for Biosensing Applications. *ACS Applied Materials & Interfaces*, **2014**, *6*, PMID: 24866105, 9705–9710.
58. Li, Y.-T.; Jin, X.; Tang, L.; Lv, W.-L.; Xiao, M.-M.; Zhang, Z.-Y.; Gao, C.; Zhang, G.-J., Receptor-Mediated Field Effect Transistor Biosensor for Real-Time Monitoring of Glutamate Release from Primary Hippocampal Neurons. *Analytical Chemistry*, **2019**, *91*, PMID: 31142114, 8229–8236.
59. He, Q.; Sudibya, H. G.; Yin, Z.; Wu, S.; Li, H.; Boey, F.; Huang, W.; Chen, P.; Zhang, H., Centimeter-Long and Large-Scale Micropatterns of Reduced Graphene Oxide Films:

Fabrication and Sensing Applications. *ACS Nano*, **2010**, *4*, PMID: 20441213, 3201–3208.

60. Jung, H. S.; Kim, H. H.; Shin, M. H.; Kim, S.; Kim, K. S.; Cho, K.; Hahn, S. K., Electroceutical Residue-Free Graphene Device for Dopamine Monitoring and Neural Stimulation. *ACS Biomaterials Science & Engineering*, **2019**, *5*, 2013–2020.
61. Zhang, M.; Liao, C.; Yao, Y.; Liu, Z.; Gong, F.; Yan, F., High-Performance Dopamine Sensors Based on Whole-Graphene Solution-Gated Transistors. *Advanced Functional Materials*, **2014**, *24*, 978–985.
62. Oh, J.; Lee, J. S.; Jun, J.; Kim, S. G.; Jang, J., Ultrasensitive and Selective Organic FET-type Nonenzymatic Dopamine Sensor Based on Platinum Nanoparticles-Decorated Reduced Graphene Oxide. *ACS Applied Materials & Interfaces*, **2017**, *9*, PMID: 29067802, 39526–39533.
63. Cohen-Karni, T.; Qing, Q.; Li, Q.; Fang, Y.; Lieber, C. M., Graphene and Nanowire Transistors for Cellular Interfaces and Electrical Recording. *Nano Letters*, **2010**, *10*, PMID: 20136098, 1098–1102.
64. Hess, L. H.; Jansen, M.; Maybeck, V.; Hauf, M. V.; Seifert, M.; Stutzmann, M.; Sharp, I. D.; Offenhäusser, A.; Garrido, J. A., Graphene Transistor Arrays for Recording Action Potentials from Electrogenic Cells. *Advanced Materials*, **2011**, *23*, 5045–5049.
65. Cheng, Z.; Hou, J.; Zhou, Q.; Li, T.; Li, H.; Yang, L.; Jiang, K.; Wang, C.; Li, Y.; Fang, Y., Sensitivity Limits and Scaling of Bioelectronic Graphene Transducers. *Nano Letters*, **2013**, *13*, PMID: 23638876, 2902–2907.
66. Hess, L. H.; Becker-Freyseng, C.; Wismer, M. S.; Blaschke, B. M.; Lottner, M.; Rolf, F.; Seifert, M.; Garrido, J. A., Electrical Coupling Between Cells and Graphene Transistors. *Small*, **2015**, *11*, 1703–1710.
67. Kireev, D.; Zadorozhnyi, I.; Qiu, T.; Sarik, D.; Brings, F.; Wu, T.; Seyock, S.; Maybeck, V.; Lottner, M.; Blaschke, B. M.; Garrido, J.; Xie, X.; Vitusevich, S.; Wolfrum, B.; Offenhäusser, A., Graphene Field-Effect Transistors for In Vitro and Ex Vivo Recordings. *IEEE Transactions on Nanotechnology*, **2017**, *16*, 140–147.
68. Hébert, C. et al., Flexible Graphene Solution-Gated Field-Effect Transistors: Efficient Transducers for Micro-Electrocorticography. *Advanced Functional Materials*, **2018**, *28*, 1703976.
69. Blaschke, B. M.; Tort-Colet, N.; Guimerà-Brunet, A.; Weinert, J.; Rousseau, L.; Heimann, A.; Drieschner, S.; Kempski, O.; Villa, R.; Sanchez-Vives, M. V.; Garrido, J. A., Mapping brain activity with flexible graphene micro-transistors. *2D Materials*, **2017**, *4*, 025–040.
70. Du, M.; Xu, X.; Yang, L.; Guo, Y.; Guan, S.; Shi, J.; Wang, J.; Fang, Y., Simultaneous surface and depth neural activity recording with graphene transistor-based dual-modality probes. *Biosensors and Bioelectronics*, **2018**, *105*, 109–115.

71. Togashi, D. M.; Ryder, A. G., Assessing protein–surface interactions with a series of multi-labeled BSA using fluorescence lifetime microscopy and Förster Energy Resonance Transfer. *Biophysical Chemistry*, **2010**, *152*, 55–64.
72. Wiederschain, G. Y., The Molecular Probes handbook. A guide to fluorescent probes and labeling technologies. *Biochemistry (Moscow)*, **2011**, *76*, 1276.
73. Hermanson, G. T. In *Bioconjugate Techniques (Third Edition)*, Hermanson, G. T., Ed., Third Edition; Academic Press: Boston, 2013, pp 465–505.
74. Aumanen, J.; Johansson, A.; Koivistoinen, J.; Myllyperkiö, P.; Pettersson, M., Patterning and tuning of electrical and optical properties of graphene by laser induced two-photon oxidation. *Nanoscale*, **2015**, *7*, 2851–2855.
75. Sprinkle, M.; Ruan, M.; Hu, Y.; Hankinson, J.; Rubio-Roy, M.; Zhang, B.; Wu, X.; Berger, C.; De Heer, W. A., Scalable templated growth of graphene nanoribbons on SiC. *Nature Nanotechnology*, **2010**, *5*, 727–731.
76. Hicks, J.; Tejeda, A.; Taleb-Ibrahimi, A.; Nevius, M. S.; Wang, F.; Shepperd, K.; Palmer, J.; Bertran, F.; Le Fèvre, P.; Kunc, J.; De Heer, W. A.; Berger, C.; Conrad, E. H., A wide-bandgap metal-semiconductor-metal nanostructure made entirely from graphene. *Nature Physics*, **2013**, *9*, 49–54.
77. Johansson, A.; Tsai, H.-C.; Aumanen, J.; Koivistoinen, J.; Myllyperkiö, P.; Hung, Y.-Z.; Chuang, M.-C.; Chen, C.-H.; Woon, W. Y.; Pettersson, M., Chemical composition of two-photon oxidized graphene. *Carbon*, **2017**, *115*, 77–82.
78. Handschuh-Wang, S.; Wang, T.; Druzhinin, S. I.; Wesner, D.; Jiang, X.; Schönherr, H., Detailed Study of BSA Adsorption on Micro- and Nanocrystalline Diamond/β-SiC Composite Gradient Films by Time-Resolved Fluorescence Microscopy. *Langmuir*, **2017**, *33*, PMID: 28025889, 802–813.
79. Rubio-Pereda, P.; Vilhena, J. G.; Takeuchi, N.; Serena, P. A.; Pérez, R., Albumin (BSA) adsorption onto graphite stepped surfaces. *The Journal of Chemical Physics*, **2017**, *146*, 214704.
80. Kuchlyan, J.; Kundu, N.; Banik, D.; Roy, A.; Sarkar, N., Spectroscopy and Fluorescence Lifetime Imaging Microscopy To Probe the Interaction of Bovine Serum Albumin with Graphene Oxide. *Langmuir*, **2015**, *31*, PMID: 26646418, 13793–13801.
81. Kim, J.; Somorjai, G. A., Molecular Packing of Lysozyme, Fibrinogen, and Bovine Serum Albumin on Hydrophilic and Hydrophobic Surfaces Studied by Infrared-Visible Sum Frequency Generation and Fluorescence Microscopy. *Journal of the American Chemical Society*, **2003**, *125*, PMID: 12617683, 3150–3158.
82. Kelley, A. M., *Condensed-phase molecular spectroscopy and photophysics*, Kelley, A. M., Ed.; Wiley, Hoboken, N.J., 2013.
83. *Fluorescence microscopy : from principles to biological applications*, Second edition, Kubitscheck Ulrich, t., Ed.; Wiley-VCH, Weinheim, Germany, 2017.

84. Kasry, A.; Ardakani, A. A.; Tulevski, G. S.; Menges, B.; Copel, M.; Vyklicky, L., Highly Efficient Fluorescence Quenching with Graphene. *The Journal of Physical Chemistry C*, **2012**, *116*, 2858–2862.
85. Swathi, R. S.; Sebastian, K. L., Resonance energy transfer from a dye molecule to graphene. *The Journal of Chemical Physics*, **2008**, *129*, 054703.
86. Swathi, R. S.; Sebastian, K. L., Long range resonance energy transfer from a dye molecule to graphene has (distance)-4 dependence. *The Journal of Chemical Physics*, **2009**, *130*, 086101.
87. Swathi, R. S.; Sebastian, K. L., Distance dependence of fluorescence resonance energy transfer. *Journal of Chemical Sciences*, **2009**, *121*, 777–787.
88. Gaudreau, L.; Tielrooij, K. J.; Prawiroatmodjo, G. E. D. K.; Osmond, J.; de Abajo, F. J. G.; Koppens, F. H. L., Universal Distance-Scaling of Nonradiative Energy Transfer to Graphene. *Nano Letters*, **2013**, *13*, PMID: 23488979, 2030–2035.
89. Chen, Z.; Berciaud, S.; Nuckolls, C.; Heinz, T. F.; Brus, L. E., Energy Transfer from Individual Semiconductor Nanocrystals to Graphene. *ACS Nano*, **2010**, *4*, PMID: 20402475, 2964–2968.
90. Lee, J.; Bao, W.; Ju, L.; Schuck, P. J.; Wang, F.; Weber-Bargioni, A., Switching Individual Quantum Dot Emission through Electrically Controlling Resonant Energy Transfer to Graphene. *Nano Letters*, **2014**, *14*, PMID: 25383700, 7115–7119.
91. Kaminska, I.; Bohlen, J.; Rocchetti, S.; Selbach, F.; Acuna, G. P.; Tinnefeld, P., Distance Dependence of Single-Molecule Energy Transfer to Graphene Measured with DNA Origami Nanopositioners. *Nano Letters*, **2019**, *19*, PMID: 31251640, 4257–4262.
92. Swathi, R. S.; Sebastian, K. L., Excitation energy transfer from dye molecules to doped graphene. *Journal of Chemical Sciences*, **2012**, *124*, 233–240.
93. Koppens, F. H. L.; Chang, D. E.; García de Abajo, F. J., Graphene Plasmonics: A Platform for Strong Light–Matter Interactions. *Nano Letters*, **2011**, *11*, PMID: 21766812, 3370–3377.
94. Guo, X.; Zafar, A.; Nan, H.; Yu, Y.; Zhao, W.; Liang, Z.; Zhang, X.; Ni, Z., Manipulating fluorescence quenching efficiency of graphene by defect engineering. *Applied Physics Express*, **2016**, *9*, 055502.
95. Hungerford, G.; Benesch, J.; Mano, J. F.; Reis, R. L., Effect of the labelling ratio on the photophysics of fluorescein isothiocyanate (FITC) conjugated to bovine serum albumin. *Photochem. Photobiol. Sci.* **2007**, *6*, 152–158.
96. Benesch, J.; Hungerford, G.; Suhling, K.; Tregidgo, C.; Mano, J. F.; Reis, R. L., Fluorescence probe techniques to monitor protein adsorption-induced conformation changes on biodegradable polymers. *Journal of Colloid and Interface Science*, **2007**, *312*, 193–200.
97. Giessibl, F. J., Advances in atomic force microscopy. *Rev. Mod. Phys.* **2003**, *75*, 949–983.

98. Kaemmer, S. B., *Introduction to Bruker's ScanAsyst and PeakForce Tapping AFM Technology*; Application note; Santa Barbara, CA, USA: Bruker Nano Surfaces Division, 2011.

99. Pittenger, B.; Erina, N.; Su, C., *Quantitative Mechanical Property Mapping at the Nanoscale with PeakForce QNM*; Application note; Santa Barbara, CA, USA: Bruker Nano Surfaces Division, 2012.

100. Hollas, J. M., *Modern spectroscopy*, 4th ed, Hollas, J. M., Ed., Lisäpainokset: Reprinted 2005, 2007, 2008, 2009, 2010.; Wiley, Chichester, 2004.

101. Cançado, L. G.; Jorio, A.; Ferreira, E. H. M.; Stavale, F.; Achete, C. A.; Capaz, R. B.; Moutinho, M. V. O.; Lombardo, A.; Kulmala, T. S.; Ferrari, A. C., Quantifying Defects in Graphene via Raman Spectroscopy at Different Excitation Energies. *Nano Letters*, **2011**, *11*, PMID: 21696186, 3190–3196.

102. Pimenta, M. A.; Dresselhaus, G.; Dresselhaus, M. S.; Cançado, L. G.; Jorio, A.; Saito, R., Studying disorder in graphite-based systems by Raman spectroscopy. *Phys. Chem. Chem. Phys.* **2007**, *9*, 1276–1290.

103. Cançado, L. G.; Takai, K.; Enoki, T.; Endo, M.; Kim, Y. A.; Mizusaki, H.; Jorio, A.; Coelho, L. N.; Magalhães-Paniago, R.; Pimenta, M. A., General equation for the determination of the crystallite size La of nanographite by Raman spectroscopy. *Applied Physics Letters*, **2006**, *88*, 163106.

104. Lucchese, M. M.; Stavale, F.; Ferreira, E. H.; Vilani, C.; Moutinho, M. V.; Capaz, R. B.; Achete, C. A.; Jorio, A., Quantifying ion-induced defects and Raman relaxation length in graphene. *Carbon*, **2010**, *48*, 1592–1597.

105. Gokus, T.; Nair, R. R.; Bonetti, A.; Böhmler, M.; Lombardo, A.; Novoselov, K. S.; Geim, A. K.; Ferrari, A. C.; Hartschuh, A., Making Graphene Luminescent by Oxygen Plasma Treatment. *ACS Nano*, **2009**, *3*, PMID: 19925014, 3963–3968.

106. Shang, J.; Ma, L.; Li, J.; Ai, W.; Yu, T.; Gurzadyan, G. G., The origin of fluorescence from graphene oxide. *Scientific Reports*, **2012**, *2*, 1–8.

107. Exarhos, A. L.; Turk, M. E.; Kikkawa, J. M., Ultrafast Spectral Migration of Photoluminescence in Graphene Oxide. *Nano Letters*, **2013**, *13*, PMID: 23339511, 344–349.

108. Trautmann, S.; Buschmann, V.; Orthaus, S.; Koberling, F.; Ortmann, U.; Erdmann, R., *Fluorescence Lifetime Imaging (FLIM) in Confocal Microscopy Applications: An Overview*; Application note; Berlin, Germany: PicoQuant GmbH, 2013.

109. Lakowicz, J. R., *Principles of fluorescence spectroscopy*, Springer, 2006, ss. 1–954.

110. Liu, X.; Lin, D.; Becker, W.; Niu, J.; Yu, B.; Liu, L.; Qu, J., Fast fluorescence lifetime imaging techniques: A review on challenge and development. *Journal of Innovative Optical Health Sciences*, **2019**, *12*, 1930003.

111. Alvarez, L. A. J.; Widzgowski, B.; Ossato, G.; van den Broek, B.; Jalink, K.; Kuschel, L.; Roberti, M. J.; Hecht, F., *SP8 FALCON: a novel concept in fluorescence lifetime*

imaging enabling video-rate confocal FLIM; Application note; Mannheim, Germany: Leica Microsystems CMS GmbH, 2019.

Appendices

1. AFM cross section heights
2. Raman spectra
3. Fast-FLIM images
4. FLIM fitting parameters
5. Lifetime heatmaps with a different number of exponential components
6. Three lifetime components of **1** F as a function of **2** A $I(\mathrm{D})I(\mathrm{G})^{-1}$
7. Linear fits of lifetime as a function square height

Table 11. **1** B square heights in nanometers

	0.2 s	0.4 s	0.6 s
20 pJ	2.25	2.37	2.51
15 pJ	1.60	1.80	2.09
10 pJ	0.41	0.49	0.44

Table 12. **1** F square heights in nanometers

	0.2 s	0.4 s	0.6 s	0.8 s	1.0 s	1.5 s
30 pJ	1.55	1.65	1.73	1.91	2.04	2.35
25 pJ	1.43	1.58	1.69	1.82	1.94	1.93
20 pJ	0.91	1.64	1.64	1.67	1.63	1.58
15 pJ	0.56	1.13	1.51	1.54	1.72	1.70
10 pJ	-	0.21	0.39	0.59	0.98	1.21

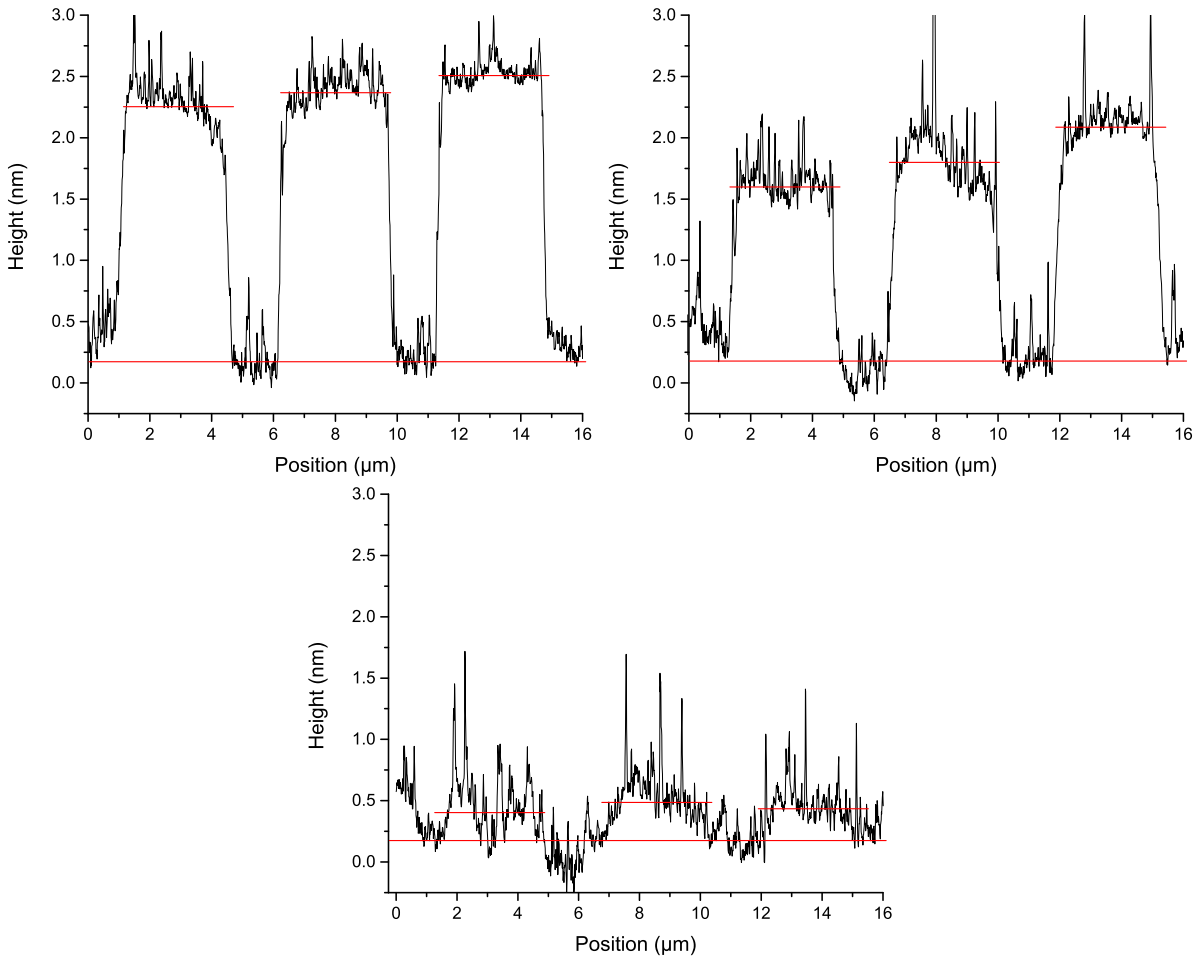

Figure 75. AFM cross sections of **1** B rows with the approximate graphene base and square heights.

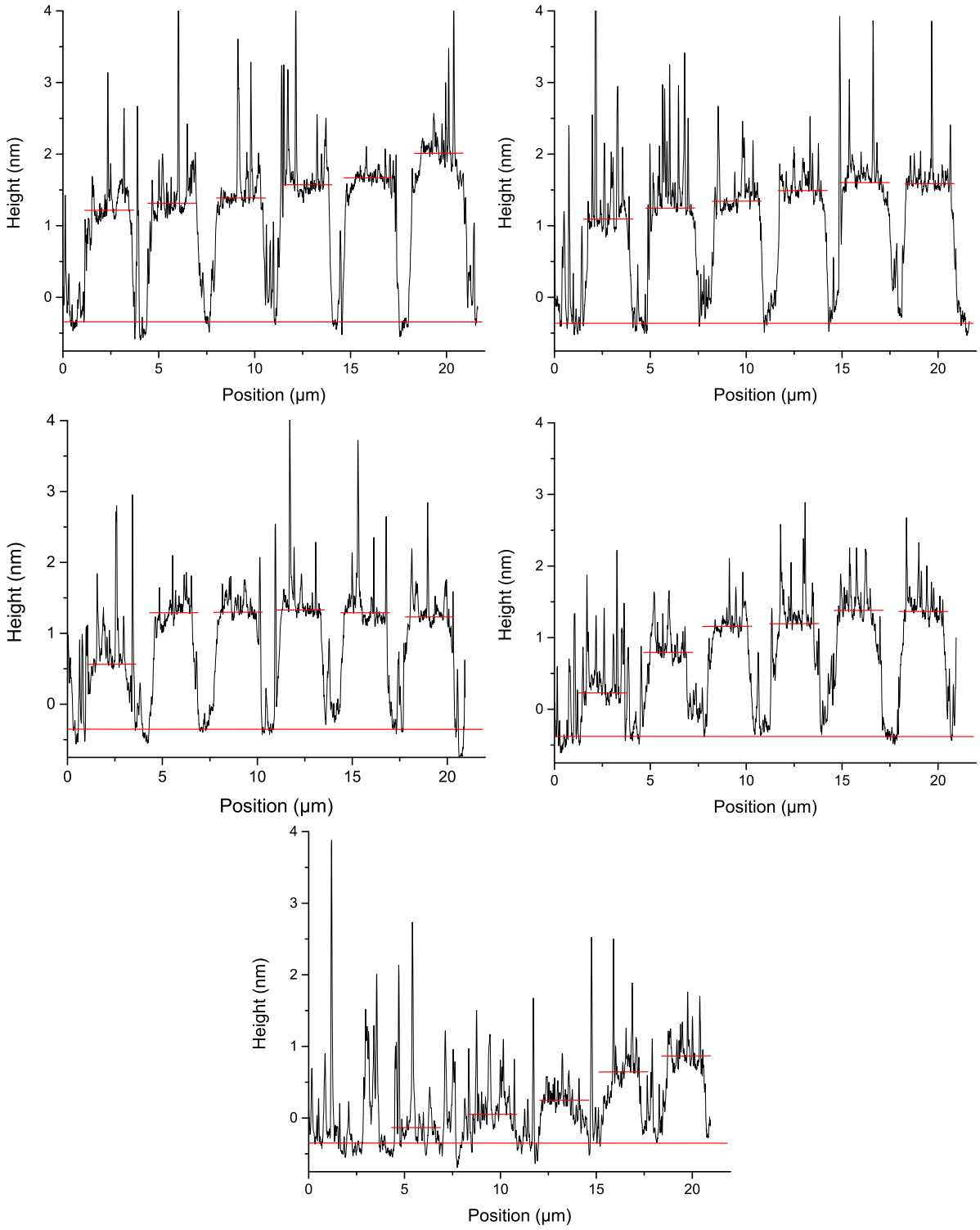

Figure 76. AFM cross sections of **1** F rows with the approximate graphene base and square heights.

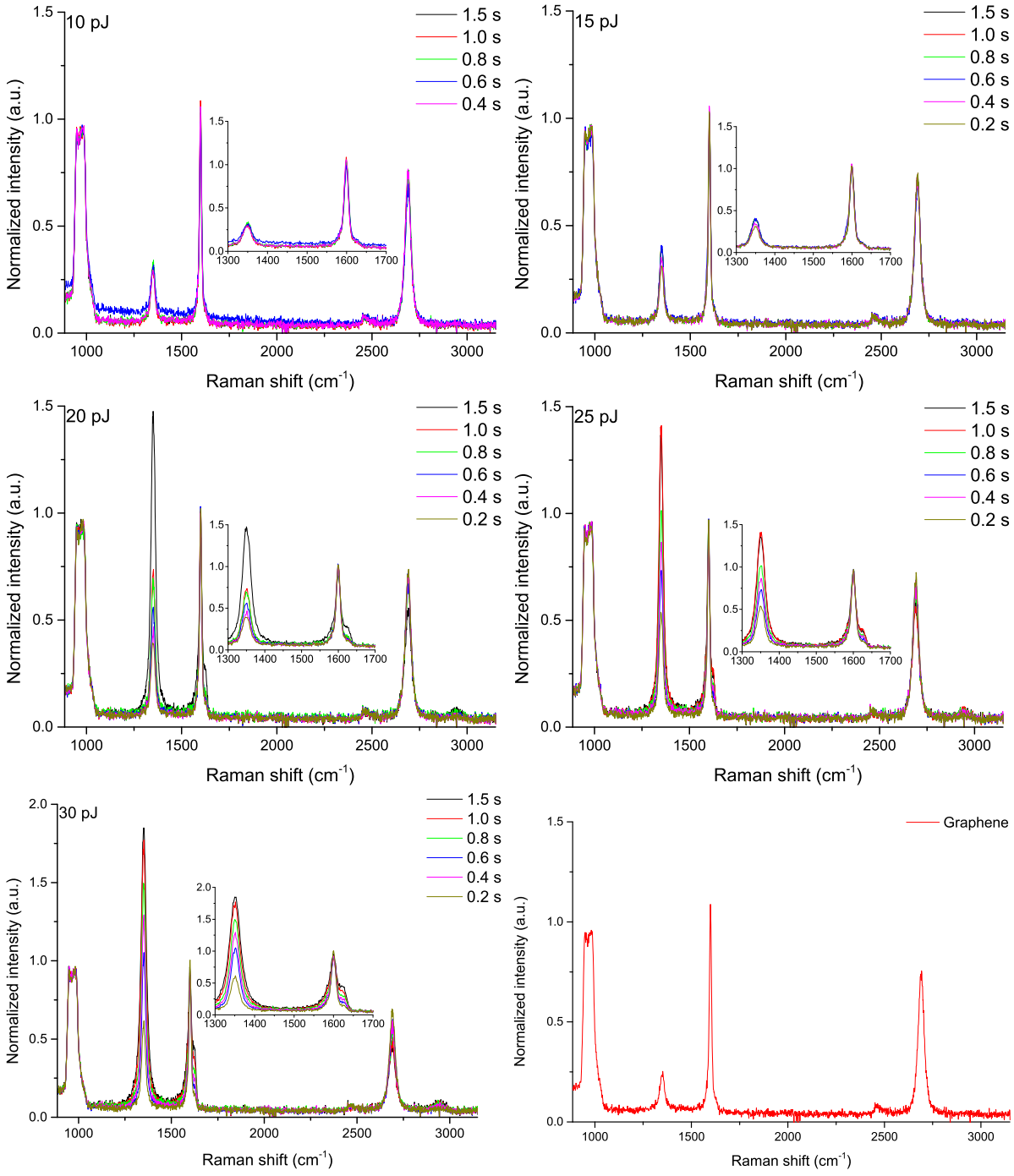

Figure 77. Raman spectra of **2** A squares at different irradiation parameters and pristine graphene at random locations. Each spectrum is an average of five points.

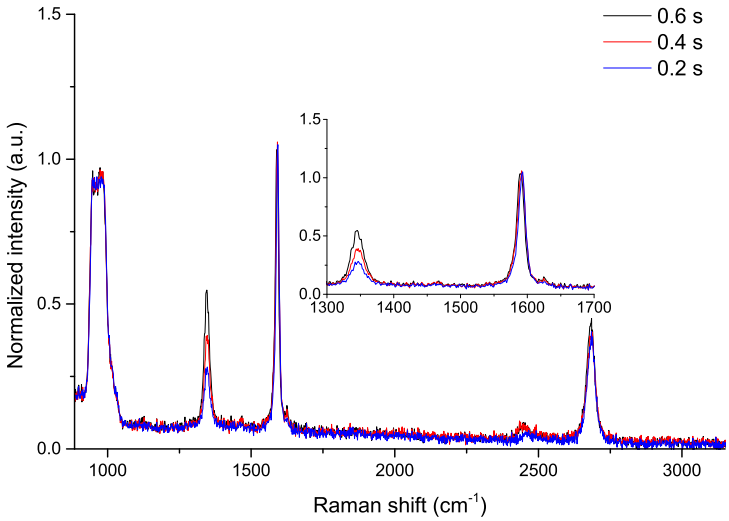

Figure 78. Raman spectra of **1** B after protein immobilization measured at 20 pJ laser pulse energy. Each spectrum is an average of five points.

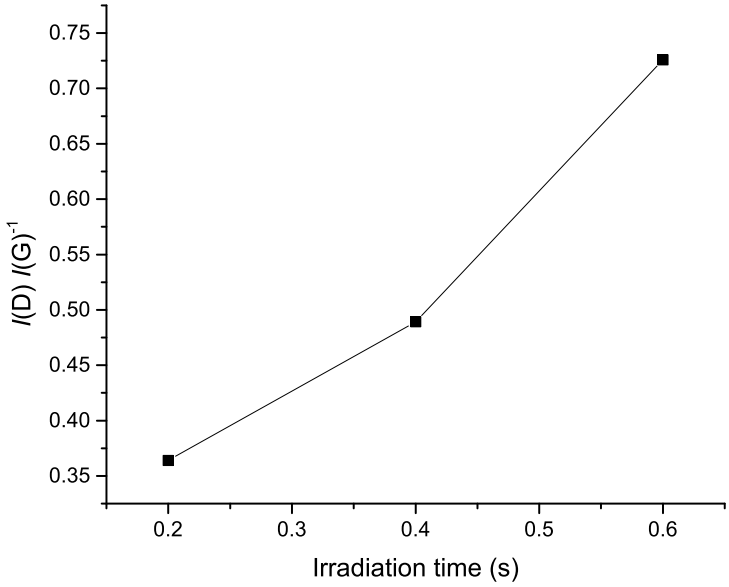

Figure 79. $I(\mathrm{D})/I(\mathrm{G})$ for **1** B after protein functionalization as a function of irradiation time.

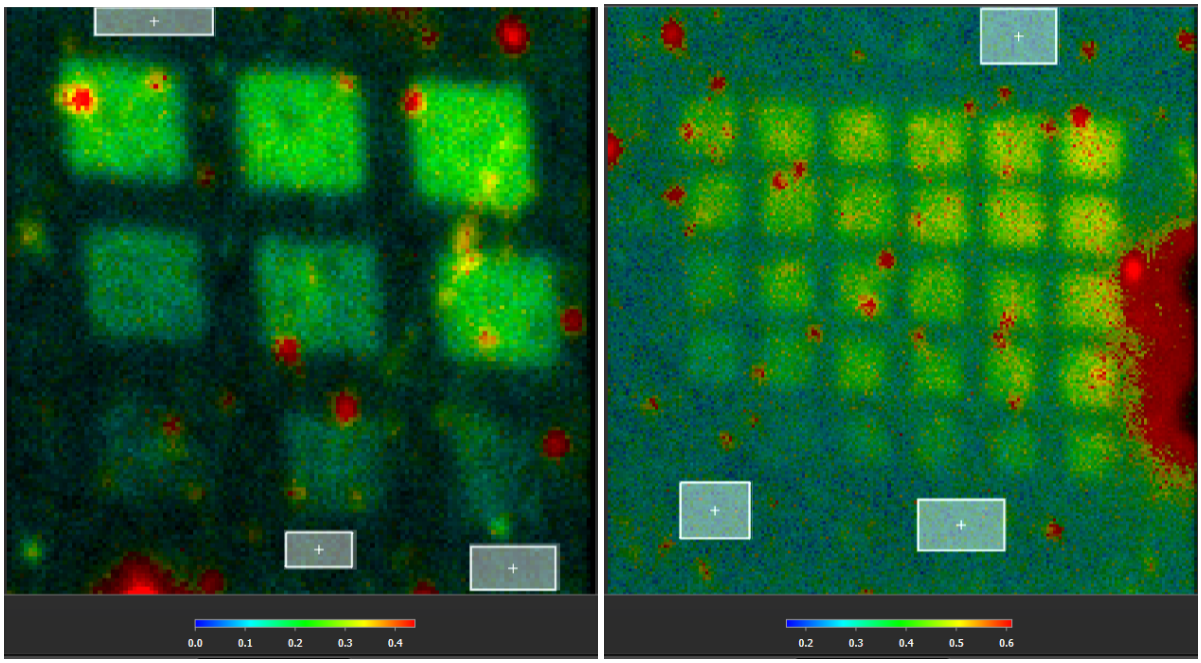

Figure 80. Fast-FLIM images of protein coated chips **1** B (left) and **1** F (right).The gray areas highlight the graphene regions used for fitting the lifetimes.

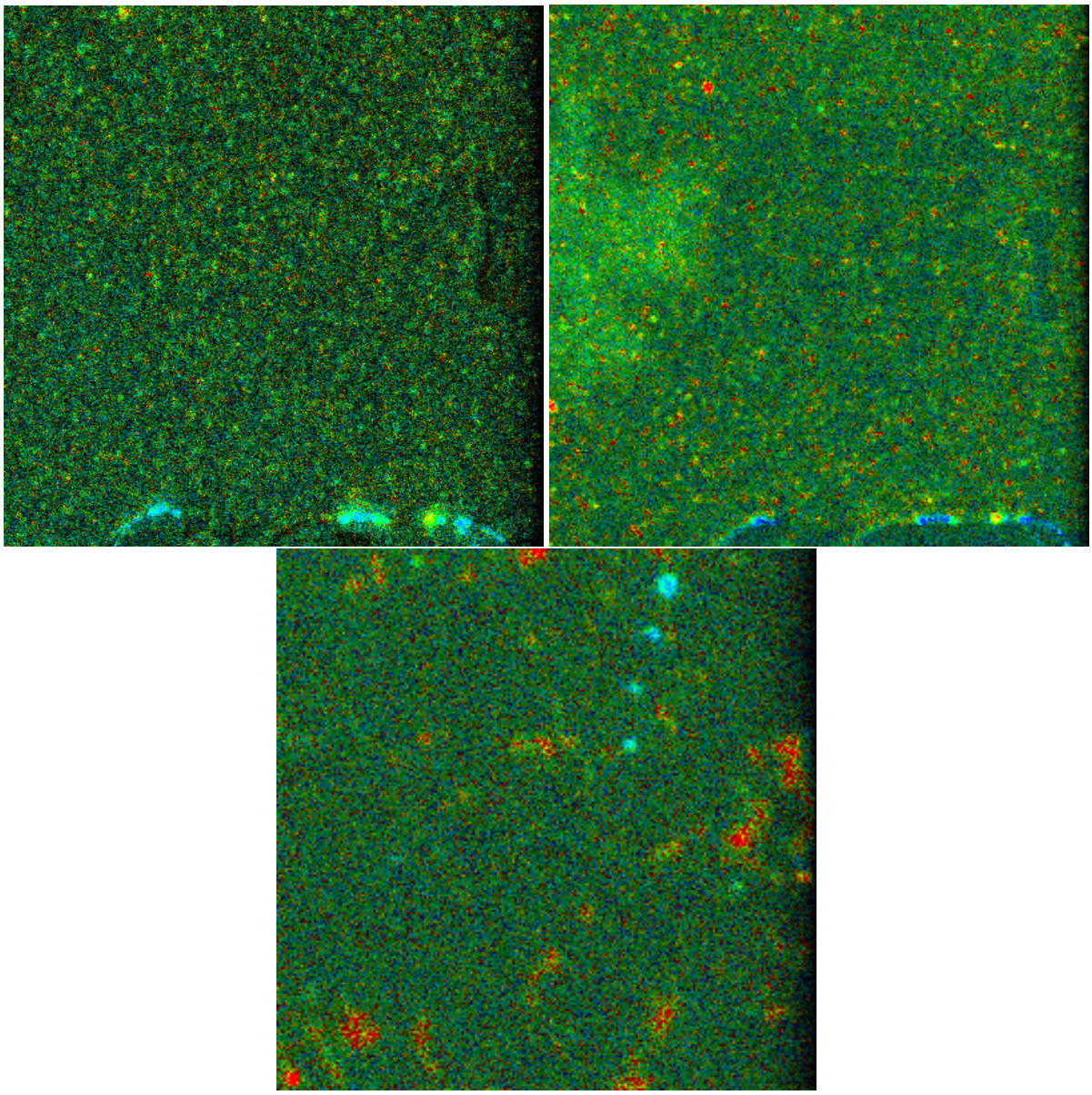

Figure 81. Fast-FLIM images of **1** B after water immersion (bottom) and **1** F (top) during (left) and after (right) water immersion.

Table 13. Fitting parameters of graphene after protein coating using one to four exponential components. The first column gives the measured area and the number of exponential components.

	τ_1	τ_2	τ_3	τ_4	A_1	A_2	A_3	A_4	I_1	I_2	I_3	I_4	χ^2
1 B, 1	0.14821				76.36106				116.710				8.318
1 B, 2	0.13335	0.85983			88.35792	0.32615			121.507	2.892			2.138
1 B, 3	0.11672	0.27011	2.35946		91.8473	6.01087	0.03826		110.550	16.744	0.931		1.215
1 B, 4	0.1132	0.1789	0.30396	2.41579	85.59364	9.5643	3.12733	0.03638	99.920	17.646	9.803	0.906	1.224
1 F, 1	0.36251				63.30183				236.647				34.456
1 F, 2	0.20247	0.63338			101.03052	12.01			210.946	78.448			2.782
1 F, 3	0.16654	0.46213	1.4607		97.40721	25.28457	0.47352		167.288	120.498	7.133		1.255
1 F, 4	0.15413	0.38074	0.80775	3.40116	90.18182	31.56288	3.23824	0.03298	143.342	123.929	26.974	1.156	1.172

Table 14. Fitting parameters of **1** F during water immersion as well as **1** B and F after it using the best amount of exponential components. The first column tells the measured area and wether the measurement was conducted during or after the immersion.

	A_1	A_2	A_3	A_4	τ_1	τ_2	τ_3	τ_4	I_1	I_2	I_3	I_4	χ^2
1 F, during	0.102	0.469	1.287	3.600	541.145	20.692	16.798	15.233	567.454	100.121	222.881	564.877	2.651
1 B, after	0.096	0.553	1.892	4.817	481.438	21.423	11.979	4.941	478.507	122.126	233.750	244.008	1.427
1 F, after	0.137	1.197	4.207		821.848	50.716	19.835		1165.026	626.116	858.173		23.514

Table 15. Fitting parameters of **1** B using a single exponential component. The first column denotes the irradiation parameters: the laser pulse energy and the irradiation time.

	A_1	τ_1	I_1	χ^2
20 pJ 0.6 s	90.131	0.267	247.832	28.787
20 pJ 0.4 s	97.004	0.246	245.695	21.248
20 pJ 0.2 s	73.621	0.240	181.864	17.185
15 pJ 0.6 s	76.584	0.239	188.437	23.581
15 pJ 0.4 s	84.104	0.203	176.066	15.008
15 pJ 0.2 s	73.420	0.191	144.344	8.098
10 pJ 0.6s	43.765	0.174	78.353	6.476
10 pJ 0.4 s	35.597	0.177	65.154	6.876
10 pJ 0.2 s	31.002	0.165	52.645	4.780

Table 16. Fitting parameters of **1** F using a single exponential component. The first column denotes the irradiation parameters: the laser pulse energy and the irradiation time.

	A_1	τ_1	I_1	χ^2
30 pJ, 1.5 s	15.827	0.590	96.217	13.819
30 pJ, 1.0 s	14.814	0.577	88.208	13.300
30 pJ, 0.8 s	15.591	0.561	90.273	12.947
30 pJ, 0.6 s	14.000	0.544	78.546	10.998
30 pJ, 0.4 s	15.184	0.527	82.507	12.084
30 pJ, 0.2 s	9.134	0.522	49.194	8.282
25 pJ, 1.5 s	17.474	0.581	104.690	15.612
25 pJ, 1.0 s	16.318	0.564	94.840	14.189
25 pJ, 0.8 s	16.908	0.552	96.279	14.998
25 pJ, 0.6 s	15.601	0.538	86.518	13.540
25 pJ, 0.4 s	10.259	0.528	55.824	8.600
25 pJ, 0.2 s	12.981	0.502	67.186	10.338
20 pJ, 1.5 s	9.153	0.588	55.487	10.693
20 pJ, 1.0 s	9.542	0.538	52.964	8.588
20 pJ, 0.8 s	11.880	0.517	63.298	9.548
20 pJ, 0.6 s	7.280	0.524	39.364	6.604
20 pJ, 0.4 s	10.918	0.502	56.517	8.516
20 pJ, 0.2 s	5.975	0.456	28.086	5.048
15 pJ, 1.5 s	11.480	0.587	69.478	13.022
15 pJ, 1.0 s	9.008	0.525	48.778	8.766
15 pJ, 0.8 s	10.577	0.497	54.197	8.626
15 pJ, 0.6 s	9.487	0.499	48.851	7.289
15 pJ, 0.4 s	8.439	0.462	40.222	7.086
15 pJ, 0.2 s	7.811	0.426	34.293	4.993
10 pJ, 1.5 s	11.687	0.507	61.100	12.563
10 pJ, 1.0 s	7.404	0.451	34.438	7.240
10 pJ, 0.8 s	7.069	0.443	32.290	6.633
10 pJ, 0.6 s	7.685	0.423	33.504	5.611
10 pJ, 0.4 s	5.366	0.384	21.273	3.736

Table 17. Fitting parameters of **1** B using two exponential components. The first column denotes the irradiation parameters: the laser pulse energy and the irradiation time.

	A_1	A_1	τ_1	τ_2	I_1	I_2	χ^2
20 pJ, 0.6 s	128.015	6.034	0.190	0.617	250.211	38.388	2.163
20 pJ, 0.4 s	131.293	7.491	0.178	0.522	241.152	40.322	2.458
20 pJ, 0.2 s	98.849	3.860	0.180	0.581	183.680	23.111	2.017
15 pJ, 0.6 s	105.972	3.043	0.179	0.666	195.543	20.903	2.395
15 pJ, 0.4 s	107.406	2.342	0.164	0.591	181.274	14.273	2.251
15 pJ, 0.2 s	90.845	4.954	0.149	0.389	139.595	19.888	2.093
10 pJ, 0.6 s	53.963	0.582	0.147	0.640	81.914	3.840	1.800
10 pJ, 0.4 s	44.102	0.364	0.151	0.780	68.493	2.930	1.630
10 pJ, 0.2 s	36.335	0.156	0.147	0.942	54.973	1.519	1.318

Table 18. Fitting parameters of **1** F using two exponential components. The first column denotes the irradiation parameters: the laser pulse energy and the irradiation time.

	A_1	A_1	τ_1	τ_2	I_1	I_2	χ^2
30 pJ, 1.5 s	25.567	4.617	0.287	0.906	75.652	43.152	1.590
30 pJ, 1.0 s	24.369	4.620	0.270	0.871	67.832	41.492	1.384
30 pJ, 0.8 s	25.576	5.056	0.260	0.833	68.653	43.426	1.291
30 pJ, 0.6 s	22.051	3.937	0.272	0.843	61.813	34.232	1.164
30 pJ, 0.4 s	24.597	4.334	0.258	0.814	65.473	36.357	1.210
30 pJ, 0.2 s	14.441	1.839	0.285	0.914	42.506	17.343	1.567
25 pJ, 1.5 s	29.085	5.526	0.268	0.872	80.489	49.690	1.128
25 pJ, 1.0 s	27.053	4.873	0.268	0.859	74.843	43.146	1.257
25 pJ, 0.8 s	27.756	4.639	0.270	0.872	77.234	41.731	1.627
25 pJ, 0.6 s	26.490	4.699	0.252	0.820	68.737	39.737	1.339
25 pJ, 0.4 s	16.638	2.999	0.256	0.809	43.902	25.017	1.369
25 pJ, 0.2 s	20.461	2.802	0.271	0.850	57.283	24.551	1.435
20 pJ, 1.5 s	16.827	2.646	0.264	0.924	45.763	25.218	1.316
20 pJ, 1.0 s	15.437	2.491	0.270	0.861	42.916	22.130	1.246
20 pJ, 0.8 s	19.626	3.386	0.251	0.798	50.901	27.880	1.147
20 pJ, 0.6 s	12.096	1.942	0.258	0.830	32.212	16.622	0.884
20 pJ, 0.4 s	17.950	2.960	0.249	0.787	46.114	24.039	1.056
20 pJ, 0.2 s	9.995	1.382	0.234	0.759	24.127	10.821	1.046
15 pJ, 1.5 s	20.178	2.937	0.280	0.962	58.331	29.125	1.393
15 pJ, 1.0 s	14.839	1.767	0.282	0.927	43.197	16.891	1.124
15 pJ, 0.8 s	18.052	2.930	0.240	0.778	44.682	23.500	1.106
15 pJ, 0.6 s	15.626	2.845	0.239	0.757	38.589	22.224	1.057
15 pJ, 0.4 s	13.451	1.685	0.252	0.805	34.963	13.994	1.185
15 pJ, 0.2 s	12.407	2.144	0.216	0.658	27.604	14.560	0.838
10 pJ, 1.5 s	21.351	2.930	0.238	0.838	52.335	25.331	1.247
10 pJ, 1.0 s	13.094	1.519	0.229	0.796	30.943	12.469	1.177
10 pJ, 0.8 s	12.609	1.655	0.217	0.742	28.251	12.664	1.117
10 pJ, 0.6 s	13.015	2.143	0.205	0.658	27.506	14.544	1.100
10 pJ, 0.4 s	8.420	0.928	0.221	0.693	19.187	6.633	0.868
10 pJ, 0.2 s	36.335	0.156	0.147	0.942	54.973	1.519	1.318

Table 19. Fitting parameters of **1** B using three exponential components. The first column denotes the irradiation parameters: the laser pulse energy and the irradiation time.

	A_1	A_2	A_3	τ_1	τ_2	τ_3	I_1	I_2	I_3	χ^2
20 pJ, 0.6 s	121.718	21.543	0.550	0.163	0.374	1.155	204.091	83.049	6.553	1.222
20 pJ, 0.4 s	125.766	20.894	0.134	0.157	0.369	1.693	203.637	79.424	2.335	1.228
20 pJ, 0.2 s	96.407	12.997	0.095	0.159	0.378	1.900	157.794	50.712	1.866	0.944
15 pJ, 0.6 s	104.319	13.677	0.211	0.154	0.370	1.545	165.664	52.163	3.365	1.224
15 pJ, 0.4 s	106.637	10.403	0.065	0.146	0.348	2.165	160.369	37.291	1.458	1.194
15 pJ, 0.2 s	86.577	12.505	0.025	0.137	0.296	2.477	121.944	38.222	0.643	1.294
10 pJ, 0.6 s	54.135	6.170	0.030	0.125	0.281	2.106	69.737	17.882	0.649	1.057
10 pJ, 0.4 s	45.471	2.753	0.025	0.134	0.341	2.453	62.884	9.694	0.623	1.034
10 pJ, 0.2 s	36.595	3.734	0.038	0.126	0.262	1.673	47.470	10.081	0.655	1.033

Table 20. Fitting parameters of **1** F using three exponential components. The first column denotes the irradiation parameters: the laser pulse energy and the irradiation time.

	A_1	A_2	A_3	τ_1	τ_2	τ_3	I_1	I_2	I_3	χ^2
30 pJ, 1.5 s	25.158	7.276	0.177	0.243	0.727	1.914	62.949	54.559	3.489	1.141
30 pJ, 1.0 s	22.808	8.472	0.934	0.207	0.585	1.241	48.596	51.130	11.960	1.024
30 pJ, 0.8 s	25.137	7.200	0.206	0.227	0.691	1.652	58.777	51.304	3.505	1.025
30 pJ, 0.6 s	21.086	6.884	0.344	0.221	0.629	1.440	48.128	44.627	5.117	0.860
30 pJ, 0.4 s	23.330	7.489	0.527	0.211	0.593	1.284	50.818	45.764	6.979	0.924
30 pJ, 0.2 s	14.117	4.867	0.111	0.204	0.601	2.002	29.755	30.145	2.290	0.984
25 pJ, 1.5 s	27.169	8.856	1.455	0.218	0.591	1.156	60.954	53.981	17.347	0.859
25 pJ, 1.0 s	24.051	9.202	1.798	0.206	0.519	1.071	51.088	49.265	19.863	1.016
25 pJ, 0.8 s	27.201	8.423	0.250	0.216	0.652	1.790	60.500	56.641	4.607	0.964
25 pJ, 0.6 s	25.035	8.521	0.830	0.197	0.562	1.204	50.963	49.363	10.310	0.964
25 pJ, 0.4 s	16.421	4.297	0.049	0.226	0.687	2.206	38.281	30.445	1.110	1.092
25 pJ, 0.2 s	19.339	6.922	0.270	0.201	0.561	1.526	40.076	40.010	4.251	0.941
20 pJ, 1.5 s	16.797	3.900	0.141	0.230	0.739	1.798	39.767	29.720	2.623	1.053
20 pJ, 1.0 s	14.814	5.003	0.237	0.208	0.605	1.500	31.800	31.200	3.664	0.908
20 pJ, 0.8 s	18.773	5.663	0.390	0.209	0.591	1.271	40.464	34.495	5.106	0.942
20 pJ, 0.6 s	10.485	4.441	0.719	0.189	0.473	1.044	20.469	21.678	7.745	0.763
20 pJ, 0.4 s	17.689	4.226	0.071	0.223	0.665	1.843	40.689	28.959	1.352	0.868
20 pJ, 0.2 s	9.895	2.148	0.020	0.207	0.625	2.404	21.106	13.850	0.503	0.863
15 pJ, 1.5 s	19.961	5.383	0.289	0.226	0.685	1.681	46.586	38.016	5.010	0.992
15 pJ, 1.0 s	14.196	4.050	0.253	0.223	0.603	1.481	32.621	25.180	3.867	0.887
15 pJ, 0.8 s	17.827	4.472	0.092	0.209	0.634	1.736	38.336	29.228	1.641	0.852
15 pJ, 0.6 s	15.424	3.947	0.058	0.214	0.649	1.808	34.026	26.405	1.090	0.904
15 pJ, 0.4 s	11.918	5.347	0.364	0.170	0.456	1.178	20.925	25.171	4.420	0.902
15 pJ, 0.2 s	11.898	3.608	0.106	0.181	0.515	1.274	22.218	19.156	1.396	0.695
10 pJ, 1.5 s	20.386	5.866	0.668	0.187	0.527	1.193	39.234	31.888	8.226	0.936
10 pJ, 1.0 s	12.871	3.021	0.120	0.189	0.559	1.504	25.053	17.403	1.865	0.919
10 pJ, 0.8 s	12.165	3.194	0.219	0.177	0.508	1.198	22.240	16.735	2.703	0.962
10 pJ, 0.6 s	12.783	3.361	0.060	0.176	0.533	1.555	23.209	18.475	0.964	0.940
10 pJ, 0.4 s	7.574	3.144	0.134	0.152	0.406	1.123	11.897	13.179	1.552	0.687

Table 21. Fitting parameters of **1** B using four exponential components. The first column denotes the irradiation parameters: the laser pulse energy and the irradiation time.

	A_1	A_2	A_3	A_4	τ_1	τ_2	τ_3	τ_4	I_1	I_2	I_3	I_4	χ^2
20 pJ, 0.6 s	51.610	70.108	21.543	0.550	0.163	0.163	0.374	1.155	86.535	117.555	83.049	6.553	1.232
20 pJ, 0.4 s	125.766	0.957	19.937	0.134	0.157	0.369	0.369	1.693	203.636	3.637	75.787	2.335	1.238
20 pJ, 0.2 s	35.139	61.268	12.998	0.095	0.159	0.159	0.378	1.900	57.514	100.280	50.712	1.866	0.952
15 pJ, 0.6 s	100.293	17.982	0.604	0.029	0.149	0.325	0.925	2.849	154.452	60.319	5.760	0.841	1.201
15 pJ, 0.4 s	31.932	74.705	10.404	0.065	0.146	0.146	0.348	2.165	48.019	112.349	37.292	1.458	1.205
15 pJ, 0.2 s	66.043	20.534	12.505	0.025	0.137	0.137	0.296	2.477	93.021	28.924	38.222	0.643	1.305
10 pJ, 0.6 s	32.529	21.607	6.170	0.030	0.125	0.125	0.281	2.106	41.903	27.835	17.882	0.649	1.065
10 pJ, 0.4 s	45.471	0.449	2.304	0.025	0.134	0.341	0.341	2.453	62.884	1.582	8.113	0.623	1.042
10 pJ, 0.2 s	36.595	3.734	0.019	0.019	0.126	0.262	1.673	1.674	47.470	10.081	0.327	0.327	1.042

Table 22. Fitting parameters of **1** F using four exponential components. The first column denotes the irradiation parameters: the laser pulse energy and the irradiation time.

	A_1	A_2	A_3	A_4	τ_1	τ_2	τ_3	τ_4	I_1	I_2	I_3	I_4	χ^2
30 pJ, 1.5 s	19.957	7.976	5.253	0.090	0.211	0.389	0.809	2.238	43.434	31.986	43.808	2.077	1.139
30 pJ, 1.0 s	21.983	8.701	1.679	0.006	0.200	0.531	1.070	3.908	45.361	47.627	18.532	0.233	1.021
30 pJ, 0.8 s	0.000	0.036	29.473	2.509	0.050	0.454	0.503	0.946	0.000	0.167	153.001	24.483	121.973
30 pJ, 0.6 s	14.606	9.466	4.684	0.141	0.182	0.336	0.730	1.726	27.483	32.786	35.268	2.511	0.858
30 pJ, 0.4 s	22.711	7.747	1.033	0.002	0.206	0.547	1.091	6.672	48.221	43.681	11.620	0.129	0.923
30 pJ, 0.2 s	13.331	5.427	0.575	0.029	0.191	0.518	1.042	2.880	26.264	29.003	6.175	0.856	0.981
25 pJ, 1.5 s	26.735	8.858	1.950	0.005	0.215	0.561	1.077	3.010	59.236	51.255	21.660	0.163	0.865
25 pJ, 1.0 s	24.051	6.907	2.295	1.798	0.206	0.519	0.519	1.071	51.088	36.976	12.290	19.863	1.025
25 pJ, 0.8 s	24.973	8.443	2.954	0.068	0.199	0.488	0.874	2.453	51.140	42.473	26.630	1.732	0.955
25 pJ, 0.6 s	24.612	8.667	1.186	0.002	0.194	0.535	1.102	6.487	49.337	47.779	13.469	0.098	0.966
25 pJ, 0.4 s	14.609	3.100	3.301	0.032	0.209	0.391	0.738	2.468	31.511	12.510	25.123	0.816	1.098
25 pJ, 0.2 s	0.000	23.788	0.785	0.019	0.050	0.591	0.863	2.502	0.000	145.002	6.987	0.497	188.498
20 pJ, 1.5 s	1.526	15.271	3.900	0.141	0.230	0.230	0.739	1.798	3.611	36.156	29.720	2.623	1.061
20 pJ, 1.0 s	13.613	4.578	1.986	0.095	0.194	0.457	0.785	1.811	27.290	21.589	16.088	1.769	0.913
20 pJ, 0.8 s	17.517	3.959	3.291	0.204	0.200	0.424	0.697	1.425	36.131	17.326	23.654	2.998	0.949
20 pJ, 0.6 s	9.815	4.861	1.030	0.001	0.182	0.426	0.952	7.532	18.375	21.363	10.112	0.083	0.756
20 pJ, 0.4 s	4.741	13.825	3.821	0.055	0.150	0.249	0.689	1.959	7.354	35.548	27.128	1.104	0.872
20 pJ, 0.2 s	7.715	2.180	2.148	0.020	0.207	0.207	0.625	2.404	16.455	4.651	13.850	0.503	0.871
15 pJ, 1.5 s	18.945	6.013	1.043	0.005	0.213	0.568	1.191	6.791	41.546	35.206	12.810	0.320	0.969
15 pJ, 1.0 s	9.868	7.532	1.673	0.034	0.175	0.365	0.864	2.361	17.761	28.381	14.910	0.819	0.873
15 pJ, 0.8 s	0.000	16.333	3.367	2.775	0.050	0.192	0.480	0.753	0.000	32.339	16.684	21.550	1.725
15 pJ, 0.6 s	7.744	8.900	3.268	0.030	0.161	0.270	0.693	2.138	12.821	24.815	23.369	0.667	0.906
15 pJ, 0.4 s	11.819	5.423	0.403	0.001	0.169	0.450	1.135	2.976	20.601	25.157	4.720	0.042	0.909
15 pJ, 0.2 s	11.497	1.120	2.948	0.090	0.177	0.357	0.540	1.316	21.026	4.123	16.410	1.218	0.701
10 pJ, 1.5 s	20.386	5.822	0.697	0.001	0.187	0.524	1.175	29.524	39.334	31.483	8.442	0.126	0.962
10 pJ, 1.0 s	1.613	11.257	3.021	0.120	0.189	0.189	0.559	1.504	3.140	21.913	17.403	1.865	0.927
10 pJ, 0.8 s	11.889	3.353	0.397	0.001	0.173	0.469	1.019	7.802	21.257	16.222	4.172	0.070	0.963
10 pJ, 0.6 s	11.961	3.567	0.897	0.009	0.164	0.417	0.745	2.599	20.232	15.326	6.895	0.254	0.939
10 pJ, 0.4 s	3.211	4.364	3.144	0.134	0.152	0.152	0.406	1.123	5.042	6.854	13.179	1.552	0.693

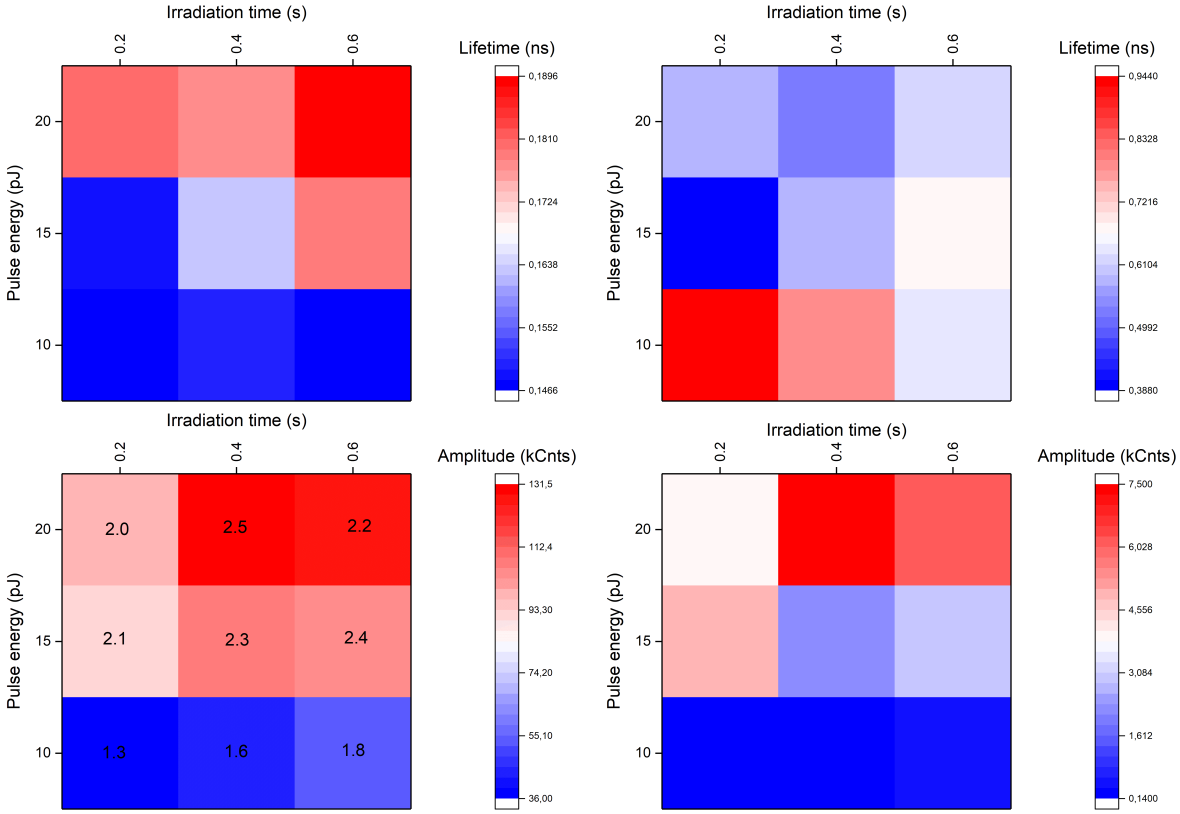

Figure 82. The lifetimes (top) and corresponding amplitudes (bottom) of **1** B fitted with two exponential components. The numbers on the amplitudes indicate the χ^2 value for the fit.

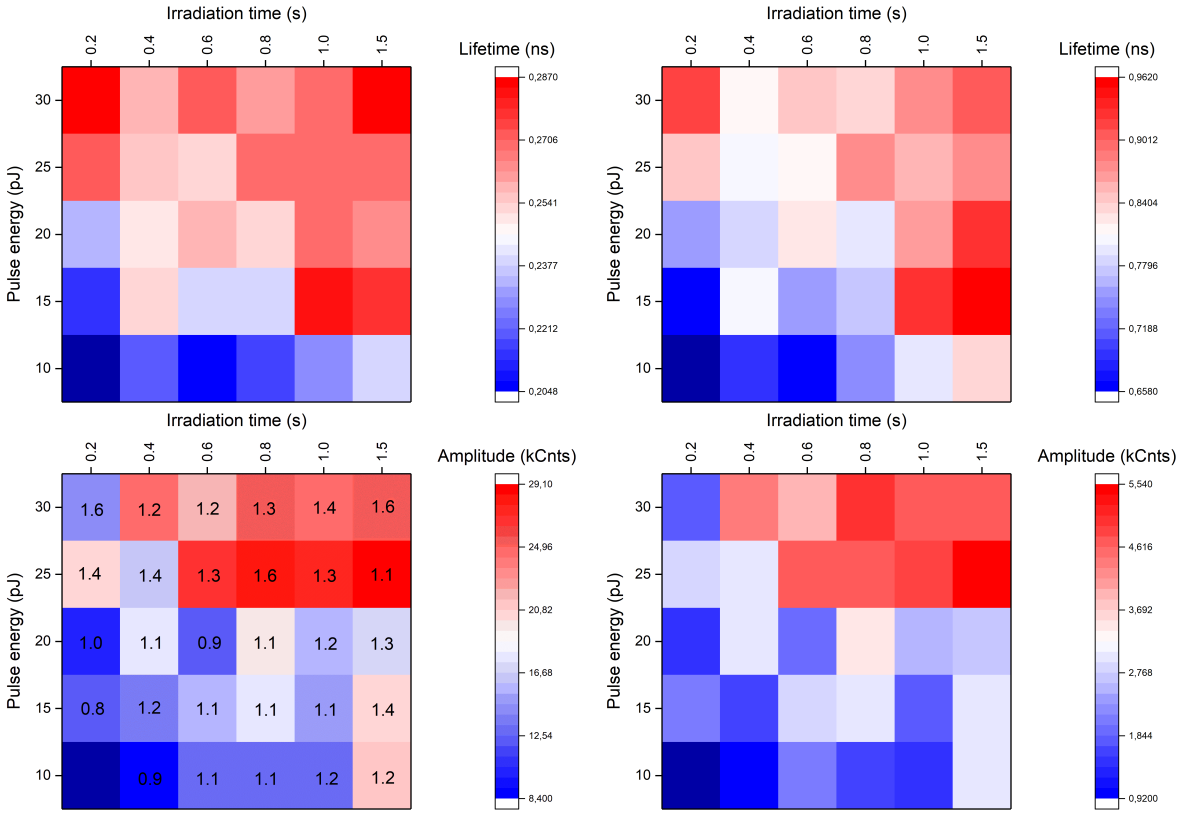

Figure 83. The lifetimes (top) and corresponding amplitudes (bottom) of **1** F fitted with two exponential components. The numbers on the amplitudes indicate the χ^2 value for the fit.

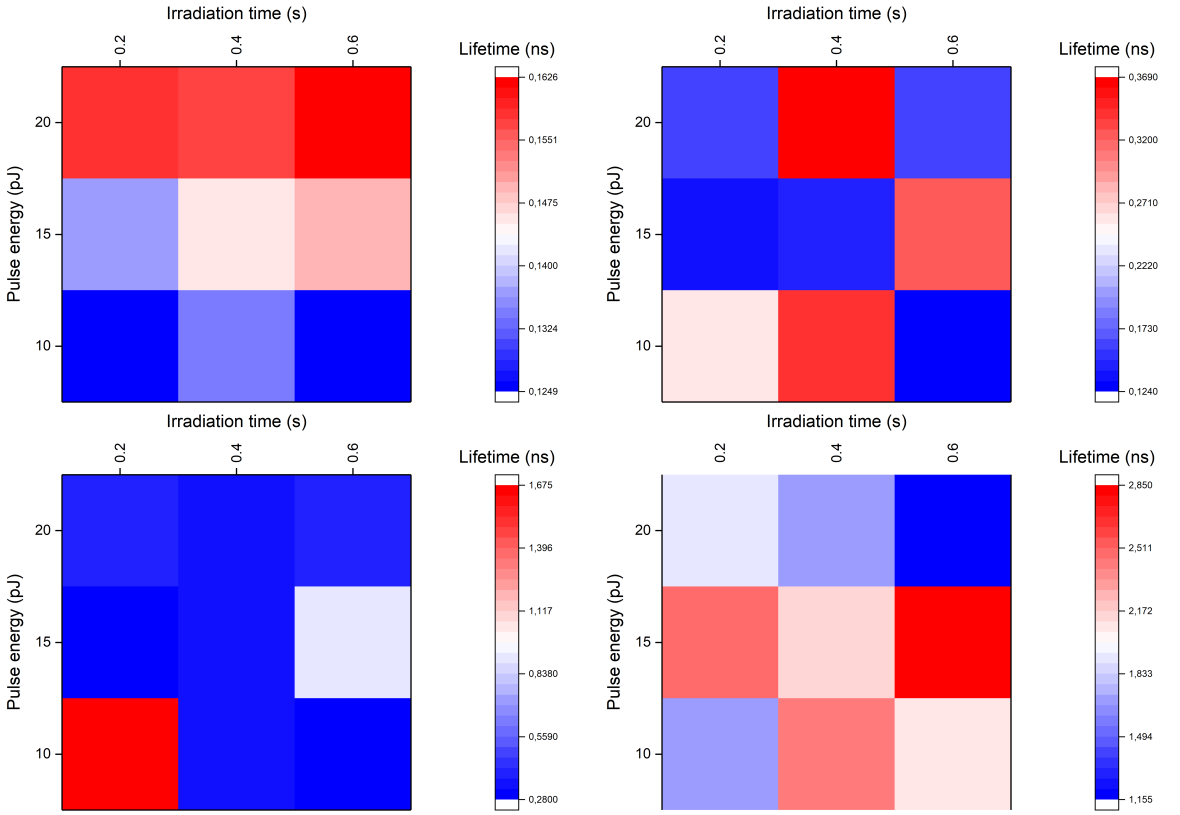

Figure 84. The lifetimes of **1** B fitted with four exponential components.

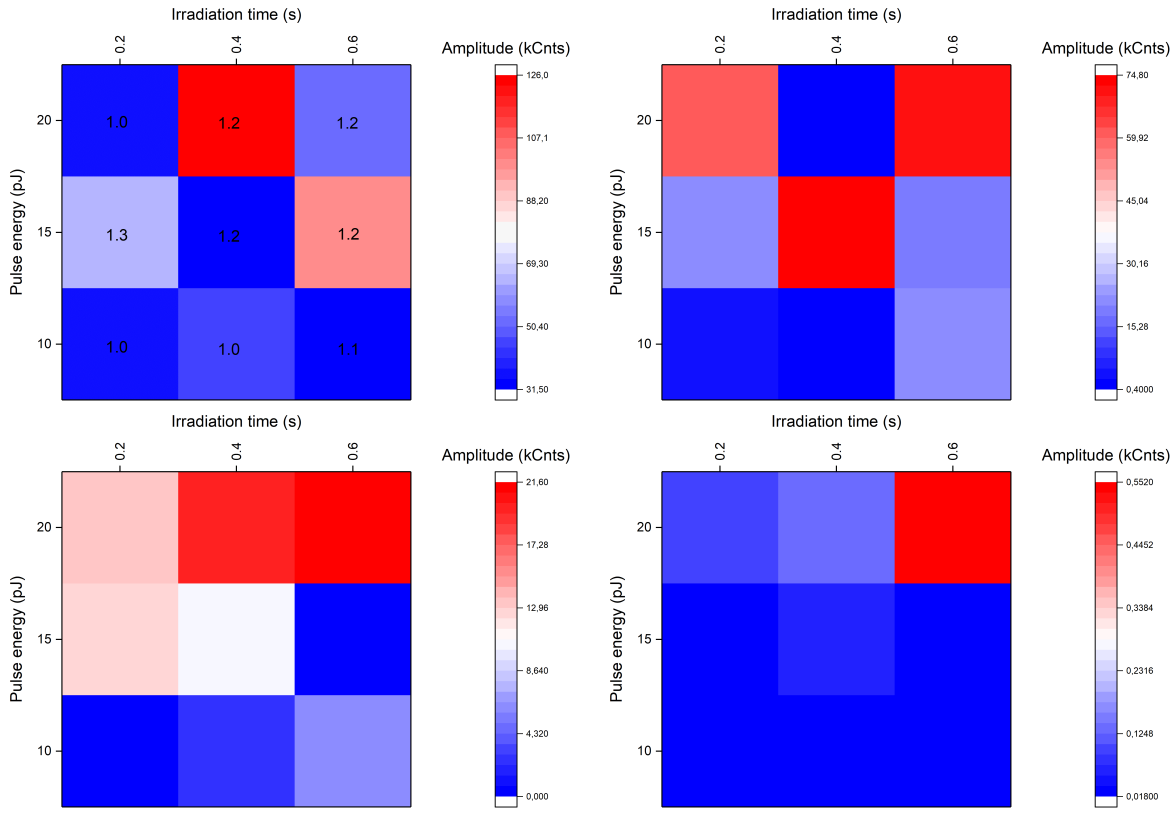

Figure 85. The amplitudes of **1** B fitted with four exponential components. The numbers indicate the χ^2 value for the fit.

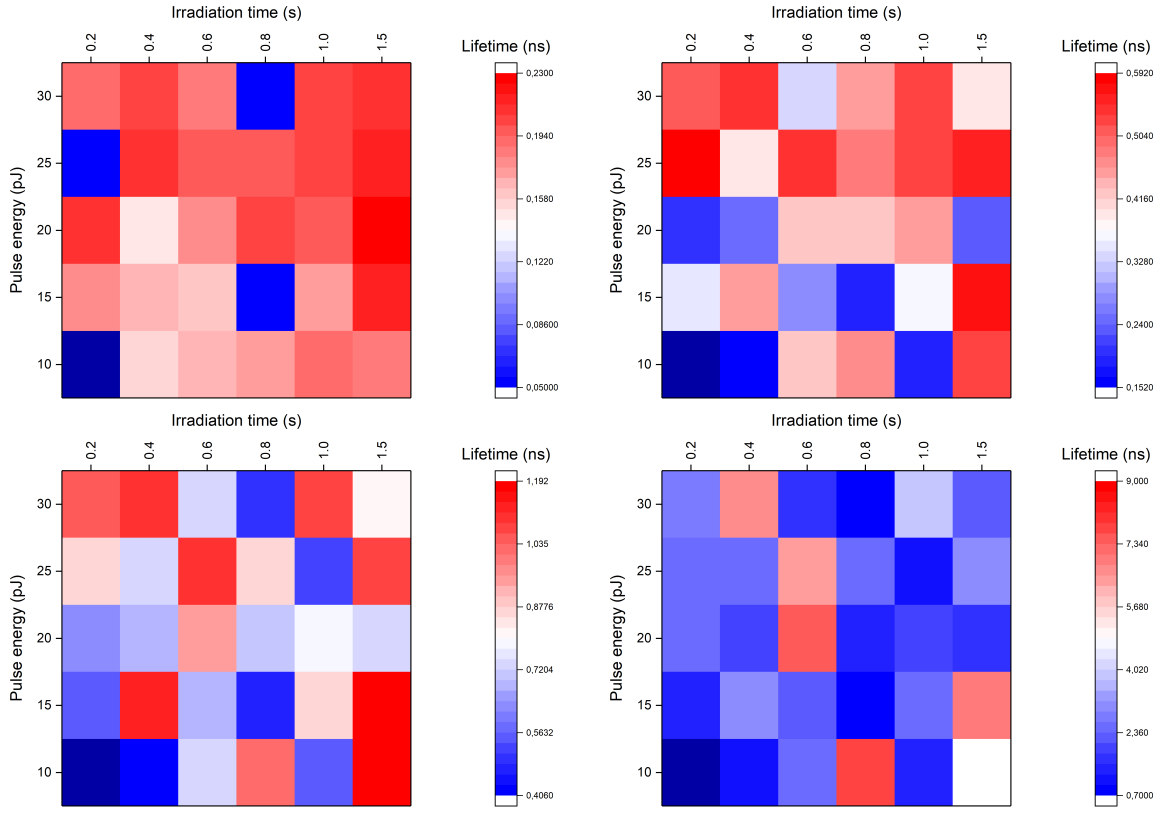

Figure 86. The lifetimes of **1** F fitted with four exponential components.

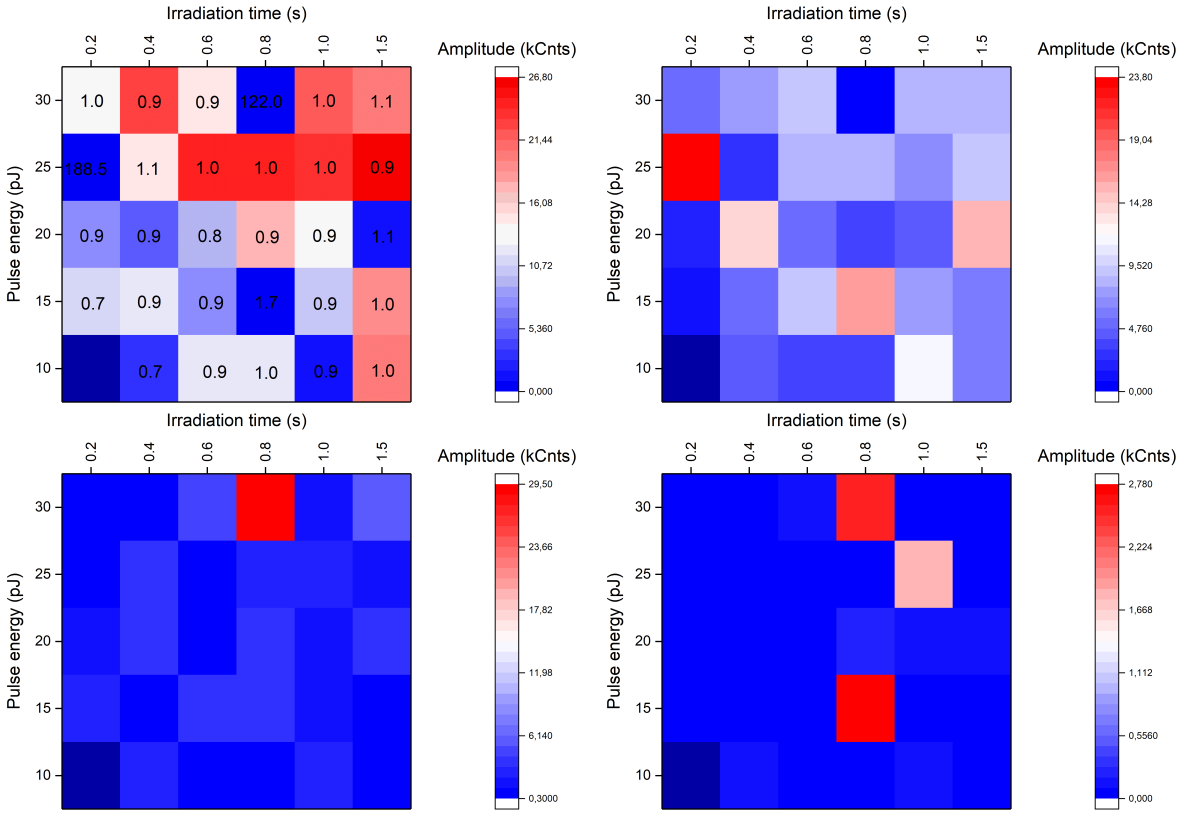

Figure 87. The amplitudes of **1** F fitted with four exponential components. The numbers indicate the χ^2 value for the fit.

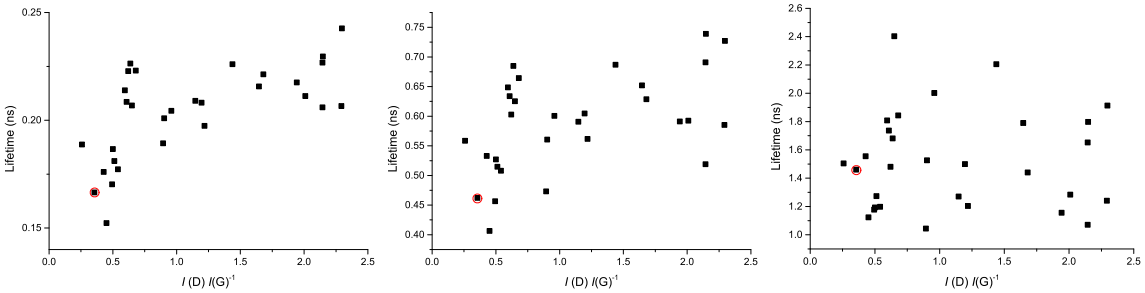

Figure 88. Three lifetimes of **1** F squares as a function of $I(\mathrm{D})I(\mathrm{G})^{-1}$ measured on **2** A (identical irradiation parameters). Circled points indicate measurement on unoxidized graphene.

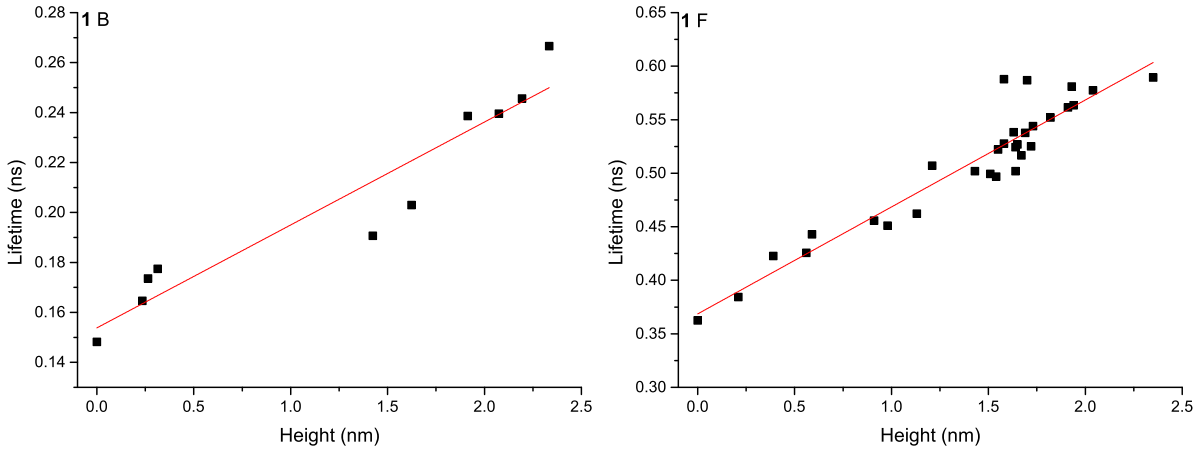

Figure 89. Linear fits of average lifetime as a function of oxidized square height. For B, the interception is at 0.1538 ns and the slope is 0.041 21 ns m^{-1}, with a Pearson's R value of 0.95316. For F the values are 0.368 61 ns, 0.0999 ns m^{-1} and 0.94605, respectively.